



**THE GEANT4 REMSIM SIMULATION FOR DOSIMETRY IN INTERPLANETARY
MANNED SPACE MISSIONS**

Susanna Guatelli¹, Maria Grazia Pia¹

¹ INFN, Sezione di Genova, I-16146 Genova, Italy

Abstract

The study of the dosimetric effects of space radiation on astronauts is an important concern of space missions for the exploration of the Solar System. To protect the crew, shielding must be designed, the environment must be anticipated and monitored and a warning system must be put in place. A Geant4 simulation has been developed for a first quantitative study of existing vehicle concepts and planet surface habitat designs, and the radiation exposure of crews therein. We will show first results of the dosimetric analysis of proposed shielding solutions in the selected geometrical set-ups, complemented with a critical analysis of the Geant4 tools currently available for this type of studies.

PACS: 11.30.Er; 13.20.Eb; 13.20.Jf; 29.40.Gx; 29.40.Vj

1 Introduction

The study of the effects of space radiation on astronauts is an important concern of space missions for the exploration of the solar system.

The radiation hazard to crew is critical to the feasibility of interplanetary manned missions. To protect crew, shielding must be designed, the environment must be anticipated and monitored, and a warning system must be put in place. Because of the strong influence on the mission design and the vehicle/habitat designs, early study must be made.

The ESA REMSIM project addresses these issues, including the development of a Geant4 [1] simulation for a preliminary quantitative study of existing vehicle concepts and habitat designs, and the radiation exposure of crews therein.

The REMSIM project is defined in the context of the European AURORA programme, for the exploration of the Solar System, whose primary object is to study possible solutions for the robotic and human exploration of the solar system with Mars, the Moon and the asteroids as the most likely targets.

The quantitative analysis of the REMSIM project employs the Geant4 Simulation Toolkit to construct a geometrical description of the vehicle, habitat, astronaut, and to model the interplanetary space radiation environment.

This report summarises the work done for the REMSIM Geant4 simulation and its results. Section 2 illustrates the vision underlying the REMSIM Geant4 simulation project.

Section 3 summarises the main aspects of the software process adopted in the simulation development.

Section 4 illustrates the architecture and design of the simulation application.

Section 5 is dedicated to the software implementation aspects of the application.

Section 6 describes the model of the interplanetary space radiation adopted in the Geant4 REMSIM application.

Section 7 is devoted to the validation at the microscopic level of the Geant4 electromagnetic physics components of interest for the REMSIM project and to the performance optimisation of the simulation.

Section 8 describes the study of shielding proposals to be applied in vehicle concepts on the basis of the effects of electromagnetic interactions. A preliminary study is performed in a simplified set-up with monochromatic beams of particles of interest; a set of shielding solutions is analysed in the context of the Galactic Cosmic Rays (GCR) environment.

Section 9 is dedicated to the effects of hadronic processes in the same context as in section 8.

Section 10 is devoted to possible radioprotective solutions for Solar Particle Events (SPE).

Section 11 regards the dosimetric analysis of space radiation environment in moon habitat

concepts.

Section 12 illustrates the process for the migration of the application to a distributed computing environment required to meet its high CPU needs.

Section 13 summarises the conclusions of the study.

2 The vision of the REMSIM Simulation

The ESA REMSIM Project reviews and quantitatively analyses existing vehicle and surface habitat concepts for interplanetary exploration. The quantitative analysis employs the Geant4 Toolkit to construct a geometrical description of the vehicle, habitat and astronaut to the required detail, and to evaluate the physical effects of space radiation in the exposed human body.

The main objectives of the simulation study are:

- a critical analysis of the Geant4 tools currently available for this type of studies, highlighting necessary extensions and improvements to the existing tools, as well as the need of further validation tests,
- a first quantitative analysis of proposed shielding solutions, contributing to an evaluation of feasibility of existing shielding hypotheses.

2.1 Critical analysis of Geant4 tools

Peculiar features of a Geant4-based simulation for the study of radiation effects in interplanetary missions are considered, with focus on the physics of particle interactions available in Geant4 and the model of the interplanetary radiation environment.

The Geant4 Toolkit provides a rich set of physics processes, covering an extended energy range. Geant4 physics is a domain still under active development; also the validation of existing physics models against experimental data is the object of intensive activity.

The REMSIM Simulation study intends to evaluate whether the energy range typical of the radiation environment of interplanetary missions is adequately treated in Geant4 physics packages, for all major types of particles involved, identifying the availability of appropriate electromagnetic and hadronic physics models and verifying the status of their validation. Recommendations for further Geant4 developments or improvements and for further validation tests, necessary for the simulation of interplanetary manned missions, will be issued as a result of this study.

Geant4 provides the facility to input primary events to the process of particle transport in matter, but it does not include specific tools for this purpose.

The REMSIM Simulation study intends to identify common needs for modeling the radiation environment of interplanetary missions, and to issue recommendations for auxiliary components to be interfaced to the Geant4 Toolkit.

The recommendations resulting from this study may have an impact on future Geant4 kernel development, as well as on the development of external tools interfaced to Geant4, of interest to ESA and to the space community at large.

2.2 Preliminary shielding analysis

Models of existing vehicle concepts and surface habitat designs are available from previous studies or other programmes.

The REMSIM Simulation intends to perform a first study of a set of candidate shielding configurations, with respect to some radiation exposure hypotheses. Simplified geometrical models are implemented, with accurate material descriptions, adequate for a preliminary shielding analysis and optimisation.

As a result of this study, critical evaluations of proposed shielding configurations are achievable, based on quantitative estimates of the dose released by radiation interactions with matter. These results may have an impact on candidate structures and materials for future interplanetary missions.

Recommendations for further in-depth studies of shielding analysis and optimisation are also identified.

2.3 REMSIM Simulation Overview

The REMSIM Simulation is based on the Geant4 Toolkit.

The main requirements of the application are:

- to model a variety of geometry and material configurations, corresponding to vehicle and surface habitat concepts;
- to model a variety of primary event generators, reproducing the spectra of different particles in relevant space radiation environments;
- to calculate the dose released in a phantom, as a result of the radiation environment in a shielding configuration.

The application design allows to model various geometry configurations. Priority is given to the development of simple configurations (multi-layer geometry) for basic shielding studies. More complex configurations, modeling vehicle and surface habitat concepts, are envisaged; their implementation is subject to the time constraints of the REMSIM project.

The shielding materials and thicknesses present in a multi-layer geometry can be selected by the user. The phantom is modeled as a simple solid of uniform material.

A variety of primary particle generators is envisaged, to describe the space radiation environment of interest to an interplanetary mission; they include models of the Galactic Cosmic Ray and Solar Particle Event spectra for various particles (protons, alpha, ions). A simple monochromatic beam generator is needed for testing purpose.

Electromagnetic and hadronic physics processes are activated, selecting them among those available in Geant4 most appropriate to the energy range of the primary particles involved.

The main output of the simulation consists of the calculation of the dose in phantom layers at various depth. Other analysis objects are also created, to understand in depth the simulation results.

The analysis is based on AIDA [4] interfaces, so that the REMSIM Simulation does not depend on any specific analysis system.

2.4 Strategy of the simulation study

The simulation study adopted an iterative and incremental approach.

The process consisted of a series of iterations, each one adding a refinement in the model of the experimental set-up or the usage of further Geant4 functionality. This approach, that is suggested by the most advanced software methodologies, allows to isolate and face problems one by one. Moreover it allows to perform successive steps on the basis of previous stable acquisitions, thus contributing to the overall reliability of results.

The Unified Software Development Process has been adopted as software process model [2].

To meet the objectives defined by the vision of the project, simplified structures of vehicle concepts and moon habitats have been modeled. The simplified structures retain the essential characteristics of geometry and materials adequate to obtain meaningful results from the simulation study at the preliminary stage of the REMSIM project.

For a better understanding of the effects involved, the contributions of electromagnetic and hadronic interactions have been analysed separately. As a first approach the dosimetric studies have been performed by activating the Geant4 electromagnetic processes only. This part of the study has proceeded through different steps: the first step consisted in the dosimetric study in possible shielding solutions of monochromatic beams of particle types and energies of interest; then the study has been iterated for Galactic Cosmic Ray and Solar Particle Events spectra.

The contribution of hadronic interactions has been added to the simulation in a second

stage, on top of the previously analysed electromagnetic contribution.

The reliability of the simulation results is based on the validation of the Geant4 physics components. The Geant4 Collaboration has an extensive physics validation program in progress, and the REMSIM project has largely profited of this activity. Specific microscopic validation of Geant4 electromagnetic models for protons and alpha particles has been performed in the context of REMSIM and of the global electromagnetic and hadronic contributions to the proton Bragg peak. Suggestions for further validation studies of interest for interplanetary manned missions are outlined in the conclusions of this paper.

2.5 Technical computing details

The code is developed according to ISO C++ standard.

The application is based on Geant4 release geant4-06-00.

The application is developed and tested on the Geant4 supported platform Linux Red Hat 7.3 - gcc 3.2.

3 Software process

The REMSIM Simulation project is based on a rigorous software process. The adoption of a disciplined process based on software engineering best practices is known as the key to produce high quality software, that meets the needs of its users within a predictable schedule, at the same time optimising the available development resources.

3.1 Process model

The software development has followed an iterative and incremental approach, based on the Unified Software Development Process [2]. The Rational Unified Process (RUP) [3] has been adopted as process framework, tailoring the process to the specific characteristics of the project. The guidance offered by the RUP represents a practical support to the implementation of best practices in the process, compatible with the guidelines of the ISO 15504 [5] software process improvement model.

The process adopted takes into account a set of best practices of software engineering, proven throughout the industry to help software development projects to be successful: iterative development, management of requirements, the adoption of component architecture, visual modeling, continuous verification of quality, management of change.

3.2 Process essentials

To achieve the delicate balance between producing quality software and delivering it quickly, within to the tight time frame defined by the REMSIM project, the process has been tailored to best fit the project needs; this operation has been performed while adhering to the best practices outlined in the previous section.

In this context, a set of essential principles have been identified:

- the development of a vision;
- the management of the plan;
- the identification and mitigation of risks;
- the design of a sound architecture;
- incrementally building and testing the product;
- regular assessment of results;
- management and control of changes;
- improvement of the software process throughout the lifecycle.

3.2.1 *Development of a vision*

Developing a clear vision is key to developing a product that meets the stakeholders' real needs. In the case of REMSIM - a project characterized by a very wide scope and a complex scientific and technical environment - the development of a clear vision of the simulation project has been essential to guarantee a concrete and meaningful output from the project itself. The clear vision developed for the REMSIM Simulation has played a key role to keep the developers focused, allowing them to achieve all the required results within a very aggressive time scale.

The Vision artifact [6] identifies the main objectives of the project and captures very high-level requirements and design constraints, to give the reader an understanding of the system to be developed.

3.2.2 *Management*

Project management represents a key element of a successful software project [7]. Therefore, a significant investment of resources has been directed into the Project Management discipline in the REMSIM Simulation project.

In the context of the REMSIM Simulation, project management has involved conceiving the simulation project itself, evaluating scope and risk, monitoring and controlling the project, planning for and evaluating each iteration and phase, as well as providing the scientific guidance necessary to achieve meaningful results from the project.

The essential role played by project management for the success of the project is objectively demonstrated by one of the metrics collected in the software process: all the code implementation and all the results contained in this report have been produced in a 10-week period, after transferring the management of the REMSIM Work Packages 2300 and 4300 to a new organization, while the production of both code and results had been null over a period of 5 months under the previous management.

3.2.3 Identification and mitigation of risks

It is essential to identify and attack the highest risk items early in the project and track them, along with other related issues.

A Risk List [8] has been assembled to capture the perceived risks to the success of the REMSIM Simulation project. It identifies, in decreasing order of priority, the events which could lead to a significant negative outcome.

Along with each risk, a plan for mitigating that risk has been outlined. This has served as a focal point for planning project activities, and has been the basis around which iterations have been organized.

3.2.4 Design of the architecture

The architecture of a software system is the organization or structure of the system's significant components interacting through interfaces. Its role is fundamental to gain and retain intellectual control over the project, to manage its complexity and to maintain system integrity.

The definition of an architectural representation has been one of the first objectives in the REMSIM Simulation lifecycle; its description is captured in the Software Architecture Document [9], which presents the architecture in multiple views.

3.2.5 Incremental build-test

The iterative approach of building, testing, and evaluating executable versions of the software in order represents a key element to the success of a software project, to flush out the problems and resolve risks and issues as early as possible.

3.2.6 Regular assessment of results

Regular status assessments provide a mechanism for addressing, communicating, and resolving management issues, technical issues, and project risks.

A fine-grained iteration plan [10], accompanied by a thorough assessment of the results from each iterations, has allowed to produce a wealth of significant and reliable results from the REMSIM Simulation project.

3.2.7 Management and control of changes

The management of changes through a consistent process is essential to keep a software project focussed, avoiding the chaos deriving from uncontrolled changes. This was especially important in the case of REMSIM, because the aggressive time scale of the project, because of the risks of failure deriving from the disruptive impact of uncontrolled changes. A strict process has been applied to the management of User Requirements, including their evolution throughout the process, to guarantee the integrity of the scope of the project and the successful achievement of concrete results.

The adoption of version control and configuration management has been adopted for all the software artifacts.

3.3 Articulation of the process

The process adopted in REMSIM Simulation has been articulated across two dimensions, according to the Unified Process model: the dimension of time, associated to the lifecycle aspects of the process and representing the dynamic aspect of the process, and the dimension of disciplines, representing the static aspect of the process through the logical grouping of activities.

From the management perspective, the software lifecycle of REMSIM Simulation has been decomposed into four sequential phases - inception, elaboration, construction and transition, each one concluded by a major milestone. The iterative and incremental approach followed by the software process has allowed to embed the usage of the software throughout its development cycle, producing meaningful physics results all along the construction phase.

The static content of the process has been articulated into a set of disciplines: Requirements, Analysis and Design, Implementation, Test, Deployment, Environment, Project Management, Configuration and Change Management. All the disciplines have been carried out through each phase, with emphasis varying over time. Some activity concerning the discipline of Business Modeling was performed in the context of the preparation of the REMSIM Proposal [11]; however, because of the specific characteristics of the project,

this discipline was not considered essential in the following REMSIM development cycle. The artifacts associated to the various disciplines produced in the course of the REMSIM project are documented in the project web site <http://www.ge.infn.it/geant4/space/remsim>. They include the Vision Document, the User Requirements Document, the Software Architecture Document, the Use Case Model, the Software Design Model, the source code, training material, the Risk List, the Iteration Plan, the Project Tracking Summary.

4 Architecture and design of the REMSIM Simulation

4.1 Architectural Goals and Constraints

The REMSIM Simulation represents a preliminary study in the framework of a long term programme of the European Space Agency for planetary exploration; the REMSIM project, of which it is part, has a duration limited to one year. The architecture of the software system is driven by the following goals, deriving from the vision of the simulation project:

- designing an agile system, capable of providing preliminary indications useful for the evaluation of vehicle concepts and surface habitat configurations within the time scale of the REMSIM project;
- designing an extensible system, capable of evolution for more refined studies beyond the REMSIM contractual constraints, without requiring changes to the kernel architecture.

The REMSIM Simulation is a Geant4-based application. As such, it provides a main and concrete classes derived from Geant4 mandatory initialization and user action classes (G4VDetectorConstruction, G4VUserPhysicsList and G4VPrimaryGeneratorAction).

The analysis is based on AIDA abstract interfaces, to avoid dependencies from any concrete analysis system.

4.2 Use Case View

The REMSIM application involves two main use cases: the simulation vehicle concepts and the simulation of surface habitats.

Both simulation studies include the same basic use cases (configuration of a geometrical set-up, configuration of different shielding models, configuration of radiation environments, evaluation of the dose deposited in an astronaut). Figure 1 illustrates the main features of the REMSIM Use Case Diagram.

Since the two simulation studies exhibit a wide commonality in their use cases, a general architecture is adopted, capable of handling both studies within a single system.

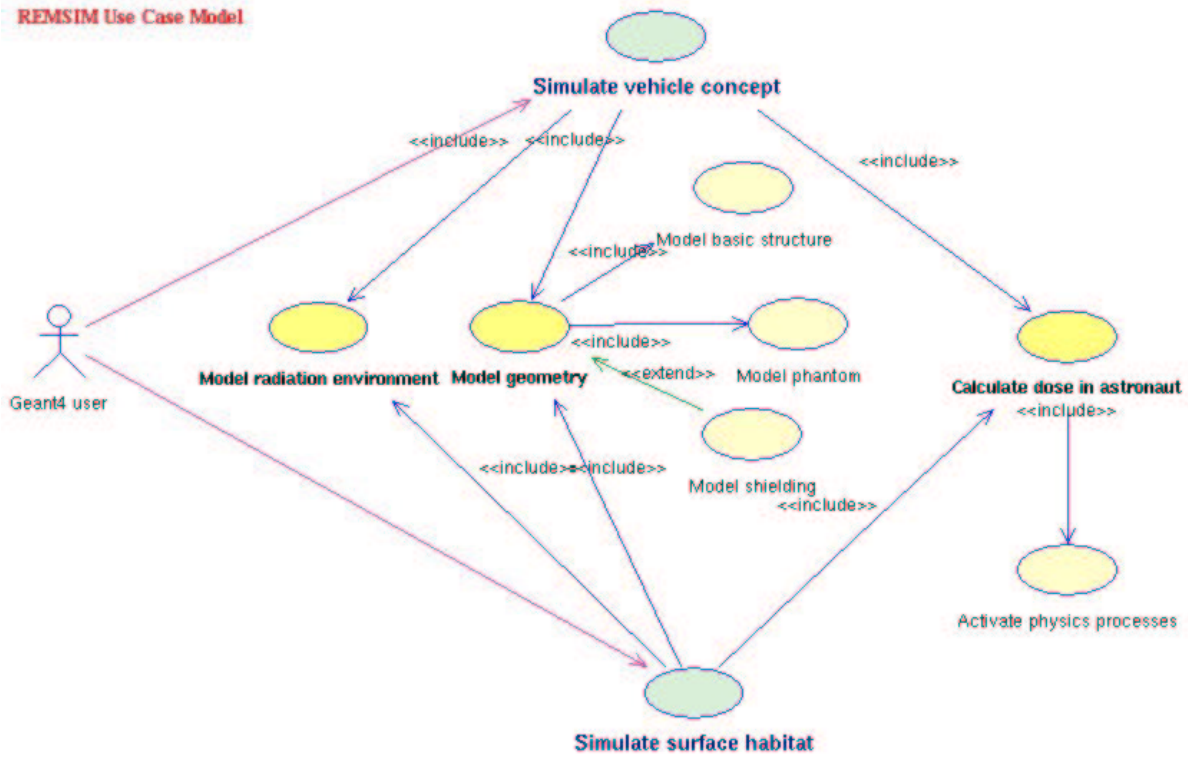


Figure 1: Use Case Diagram.

4.3 Logical View

The domain decomposition of the Geant4 REMSIM application is driven by the use case model. The resulting design is shown in figure 2; its most significant aspects are illustrated in the following sections.

4.3.1 Geometry Design

The design of the geometry component is shown in figure 3.

The geometry design fulfills the requirement of configuring the application with different geometrical set-ups for the study of vehicle concepts and of surface habitats, taking into account that each of them may appear in different models (basic structure only, with

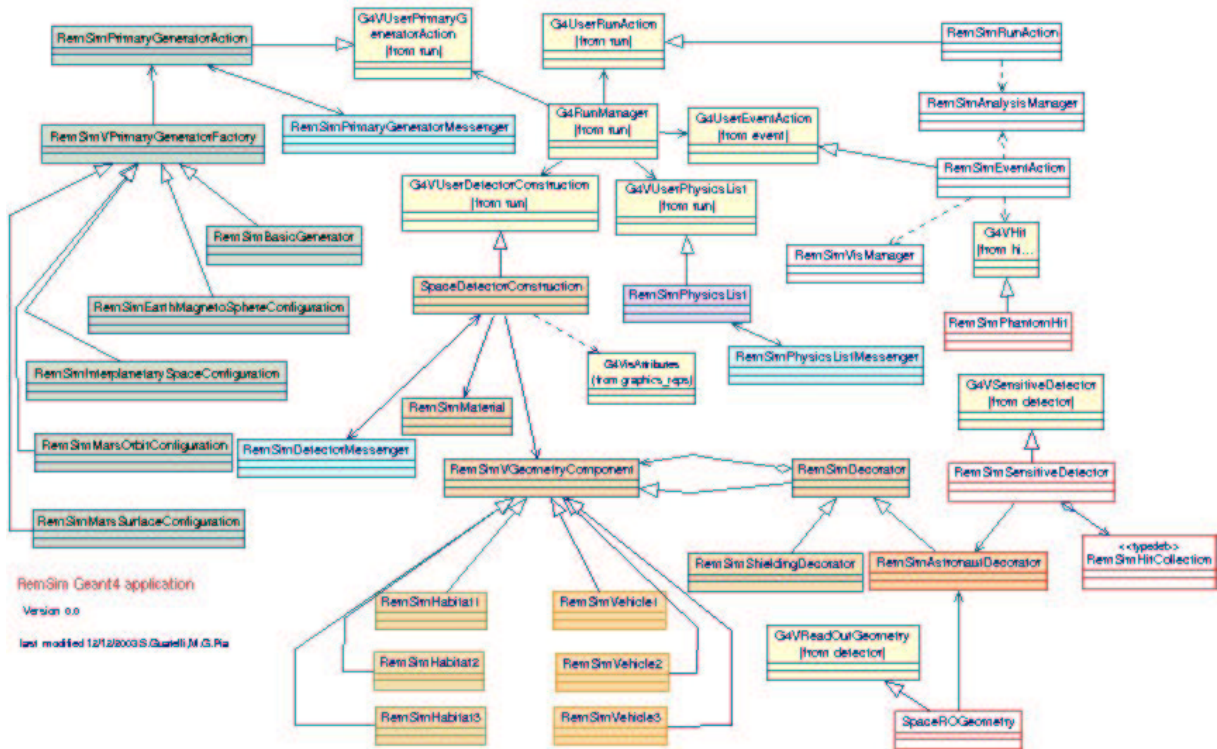


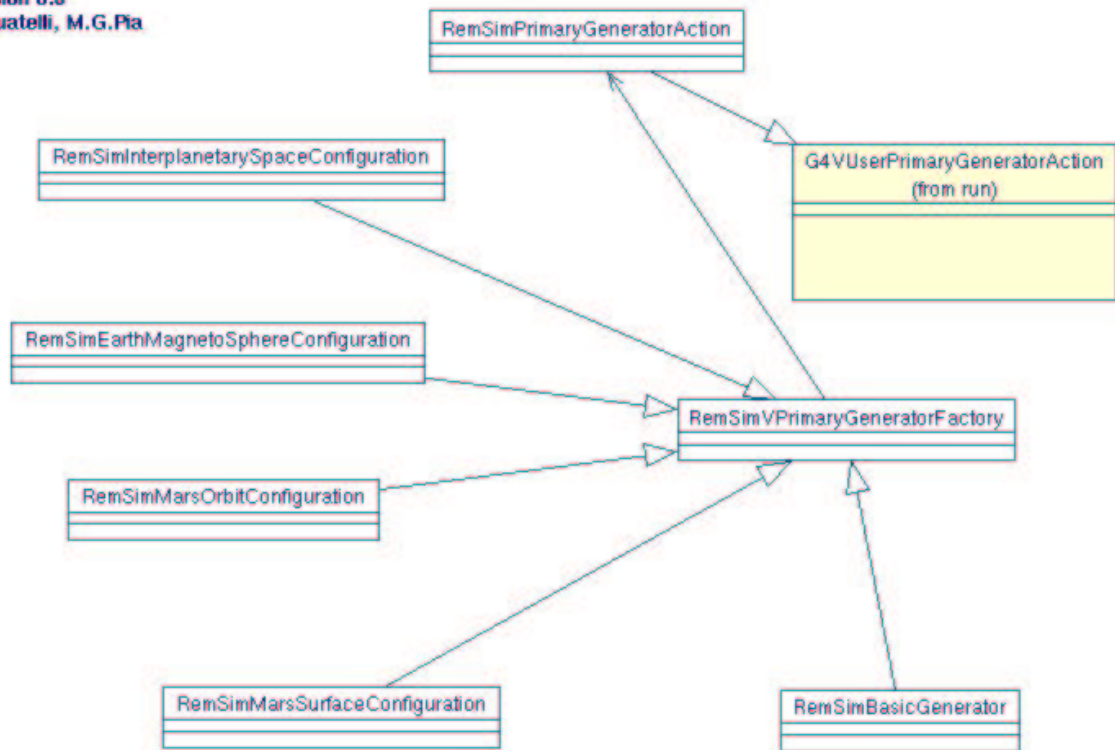
Figure 2: Design.

shielding added, with an astronaut in different positions inside etc.). For this purpose a Decorator design pattern [12] is adopted.

The various experimental set-ups (habitats and space vehicle concepts), the shielding structures and the astronaut phantom are defined through the Decorator design pattern.

The adoption of this pattern allows the user to define the experimental set-up with great flexibility, extending the geometrical functionality by adding the necessary components dynamically.

The RemSimDetectorConstruction class has the responsibility of the geometry definition. The RemSimDetectorMessenger class defines the actions allowing the user to change experimental set-up conditions in an interactive session. The RemSimMaterial class defines the materials present in the geometrical set-up. G4VisAttributes allows the user to visualise the geometrical volumes of the experimental set-up.



The design pattern Abstract Factory has been adopted to modelise the primary particle generator

Figure 4: Design of primary particles component.

RemSimPhysicsListMessenger allows the user to change the threshold of production of secondary particles interactively.

4.3.4 Sensitive Detector Design

The energy deposit due to the passage of primary particles and their secondary particles generated is collected in a sensitive detector, corresponding to the phantom representing the astronaut. The design concerning the sensitive detector is shown in figure 6. It involves the definition of a parallel geometrical description, to be used to collect the energy deposit in the astronaut object, motivated by performance optimisation arguments.

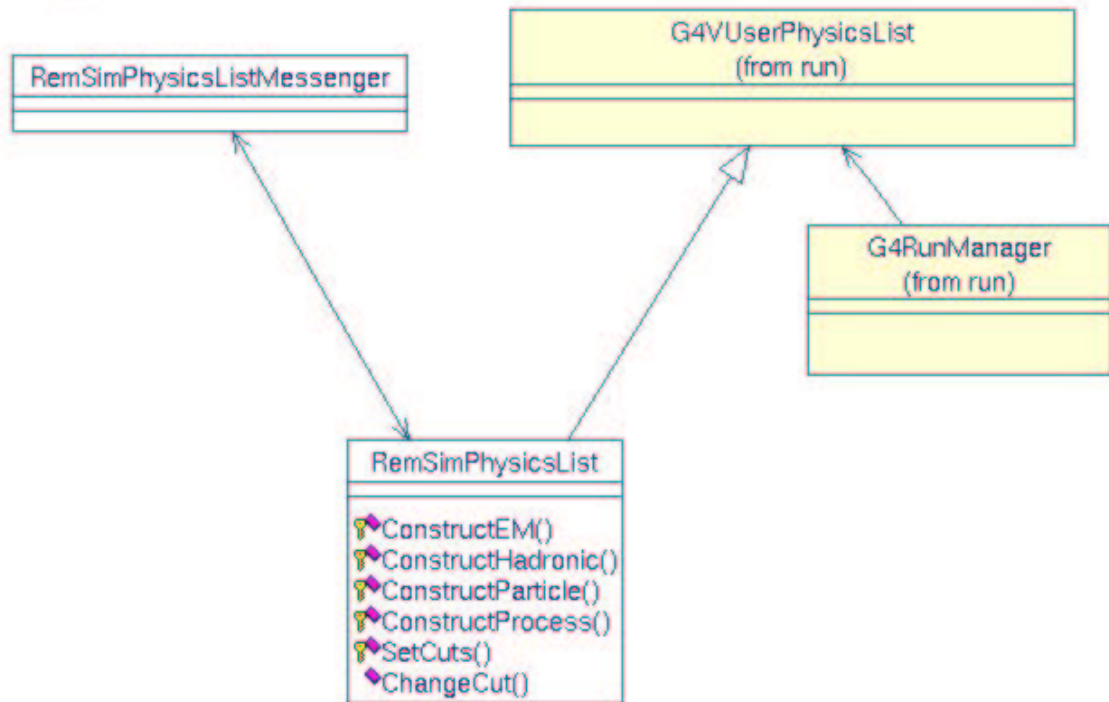


Figure 5: Design of the physics component.

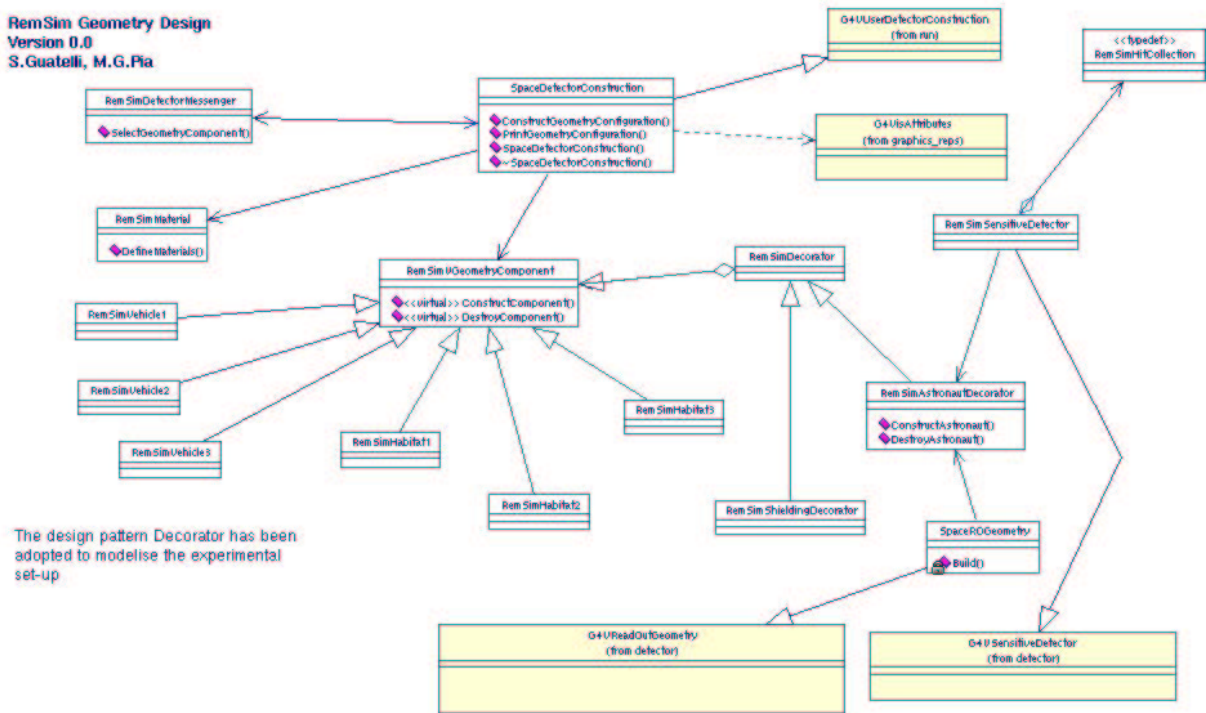
4.3.5 Analysis Design

The design of the analysis component is shown in figure 7. It conforms to the recommendations for handling analysis issued for Geant4 Advanced Examples.

The RemSimAnalysisManager class has the responsibility of the analysis. It applies the Singleton design pattern [12]. The RemSimRunAction class controls the initial and final phases of the analysis (booking and storing analysis objects). The information about the energy deposit in the sensitive detector is stored in an analysis object, such as a histogram or ntuple.

5 The Geant4 REMSIM application

This section is dedicated to relevant implementation aspects of the method adopted to develop the Geant4 REMSIM application.



The design pattern Decorator has been adopted to modelise the experimental set-up

Figure 6: Sensitive detector design.

5.1 Implementation

The Geant4 REMSIM application encompasses components, that have different responsibilities and cooperate to achieve the goals of the application defined in the User Requirement Document. The implementation of the software reflects the design model described in section 4.

The next sections describe in detail the various components.

5.1.1 Primary particle generation

This element has the responsibility of the generation of primary particles.

Primary particle types can be protons, alpha particles, ions, electrons, photons, neutrons, etc..

Primary particles can be generated as monochromatic beams or on the basis of a given energy spectrum. The energy spectrum is supplied in an ASCII file.

The user can generate primary particles from a unique point in the experimental set-up or from a plane or from the surface of a hemisphere.

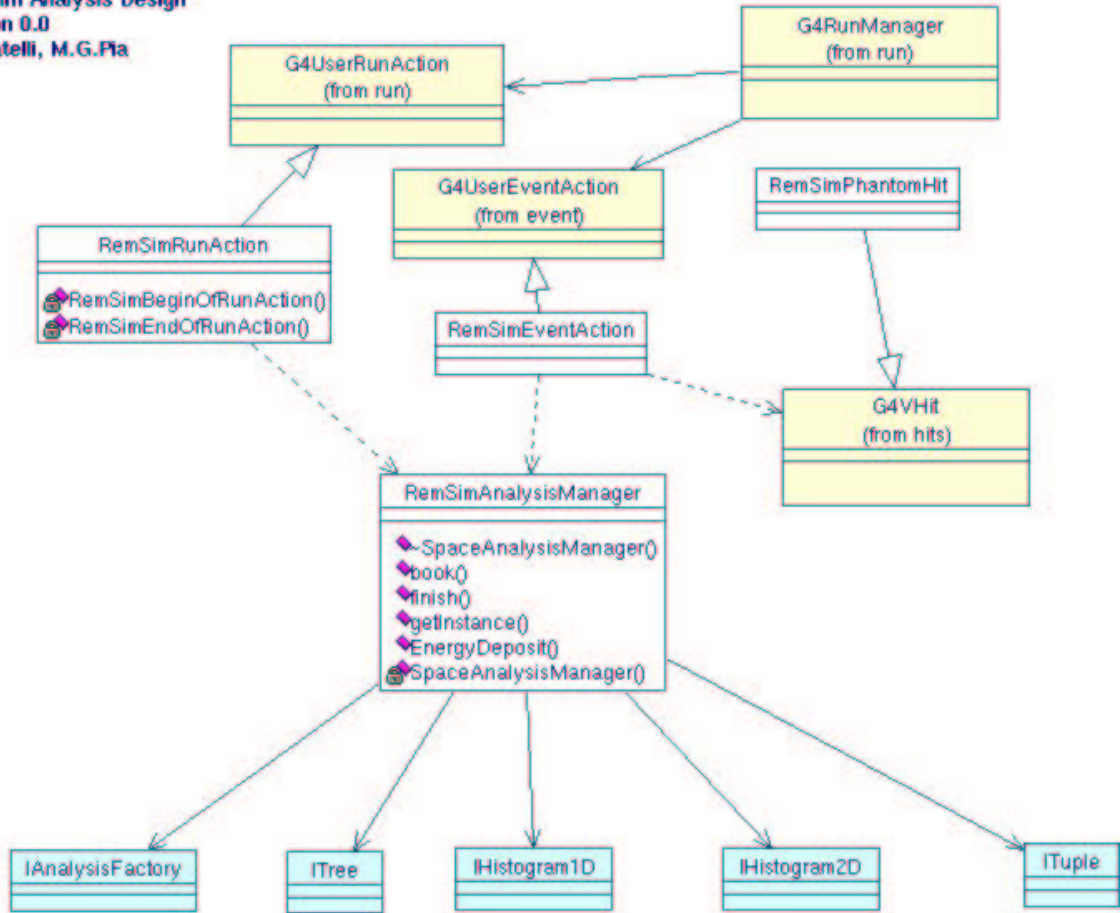


Figure 7: Analysis design.

The direction of the primary particles can be fixed or randomized on the basis of a given algorithm.

The user can choose the conditions of the generation of primary particles interactively.

5.1.2 Geometry

This component has the responsibility of the configuration of the experimental set-up in terms of volumes and materials.

The vehicle, habitat concepts and the Astronaut ¹ are defined in this component.

¹The Astronaut is often referred to as *phantom* in this document, according to the convention in use in medical physics, where the object of dosimetric studies is often called phantom.

According to Geant4 geometry modeling, a world volume is defined, containing all the geometrical components of the experimental set-up and defining the reference system of coordinates.

The geometrical elements are defined through their shape, sizes, presence of magnetic fields, sensitivity and position (translation and rotation) in the world volume.

A material is associated to each geometrical volume defined. A material can be defined through its density, atomic and mass number if it is an element, or as a mixture of elements, given the fraction in mass of each constituent, or as a heterogeneous material, given the fractions in mass of each elementary material. A material can be defined also through its density, pressure, temperature, atomic and mass number.

5.1.3 Astronaut

The Astronaut is the geometrical component where the energy deposit is collected. The energy deposit results from the interactions of the primary and secondary particles in the associated volume.

The collection of the energy deposit in the Astronaut is made possible by defining the associated volume as a sensitive one.

The user can retrieve the information of energy deposit, position, particle type resulting from particle transport in the Astronaut.

5.1.4 Particles

This component has the responsibility of the instantiation of particles involved in the simulation study.

The Geant4 pre-defined particles (as for example electrons, positrons, photons, neutrons, protons, alphas) are just instantiated; instead, ions, that are not provided as default by the Geant4 Toolkit, have been created.

Carbon, Oxygen, Silicon and Iron ions have been created for REMSIM Simulation, providing information of their mass, atomic and mass numbers. These ions are completely stripped of their electrons.

5.1.5 Physics

The physics component has the responsibility of the activation of Geant4 physics processes.

Geant4 does not provide any default physics processes. The user must select the processes and models to be activated, among those available in the Geant4 Toolkit, for all the particle types involved in the simulation.

The physics component is modularised in sub-components: each of them controls the activation of the processes for a given type of particle. This structure contributes to the flexibility of the simulation.

The user can activate both electromagnetic and hadronic physics processes.

The threshold of production of secondaries must be fixed in this component; this parameter, called *cut in range*, defines the condition of generation of secondary particles. A particle is generated if its range is higher than the value of the cut. Section 7 illustrates the optimisation of this parameter.

The next subsection is dedicated to the Geant4 electromagnetic physics models highlighting significant aspects of the models chosen for the REMSIM Geant4 application. The hadronic physics is a critical domain of study; for this reason an entire section is dedicated completely to it (section 9).

5.1.6 Selection of electromagnetic models

Geant4 offers alternative and complementary physics models for both electromagnetic and hadronic physics.

Geant4 provides two main packages for modeling the electromagnetic physics interactions: the Standard package and the Low Energy package.

The Standard package handles particles from 1KeV up to $O(\text{TeV})$ and it is based on theory-driven models. This package is used in the Geant4 REMSIM application to model the interaction of positrons and muons with matter.

The Geant4 Low Energy package [14], [15], [16] is fundamental for space and medical applications, because it extends the coverage of electromagnetic interactions in Geant4 below 1. keV.

This package includes two sets of models of electromagnetic processes for electrons and photons: one based on evaluated data libraries (EPDL97, EEDL, EADL) and one based on the Penelope analytical models [17]. It also includes models for the electromagnetic interactions of hadrons and ions, including specialised extensions at low energies based on Ziegler and ICRU parameterisation [18], [19].

The Low Energy Package has been chosen to model the interaction of photons, electrons, protons, alpha particles and heavy ions in the REMSIM simulation, since it is more accurate in the energy range of interest for project [20].

5.1.7 Stepping

This component manages information regarding the steps of particles in the experimental set-up.

A step is defined in Geant4 as the distance between two interaction points of a particle in the experimental set-up.

At this level, for example, the user can retrieve the information about the position of a step, the type and the initial energy of the particle associated to the step, etc..

5.1.8 Messengers

The messengers allow to change simulation parameters in interactive session mode or through macros. The Geant4 REMSIM application is provided of messengers to define physics processes to be activated, to change primary particles configuration and geometry experimental set-ups, to define the number of events to be generated.

5.1.9 Visualisation

The Geant4 REMSIM application is interfaced to external visualisation tools in order to visualise the experimental set-up and the tracks of particles. The user can use OpenGL, DAWN or VRML as graphic tools according to the purpose of the visualisation (for debugging, for producing high quality pictures, or for creating pictures to be put on the web). DAVID has been used to debug the experimental set-up in the case of overlapping volumes.

5.1.10 Analysis

The Geant4 REMSIM application is interfaced to external analysis tools through AIDA 3.0. Anaphe 5.0.5 [13] has been chosen as concrete AIDA implementation to be used for the simulation analysis.

The use of these analysis tools allows to store the results of the simulations in histograms, ntuples, data vectors in different formats.

6 Model of the space radiation environment

In the Earth magnetosphere and in the interplanetary space in the Solar System, the particle or radiation population consists of:

- Solar X-rays,
- Solar event protons and alpha particles,
- Solar event electrons,
- Jovian electrons,

- trapped protons and electrons,
- Galactic cosmic rays (protons, alpha particles, ions),
- Galactic X-rays and gamma-rays [21].

Due to the time limits of the project, the strategy adopted for the REMSIM simulation has considered only a limited set of radiation environment configurations: Galactic Cosmic Rays (GCR) and Solar Particle Events (SPE). Their effects on vehicle and moon habitat concepts have been investigated with the approximations illustrated in the next sections.

6.1 Galactic Cosmic Rays

As a conservative approach to estimate the dosimetric effects on vehicle and habitat concepts, it has been decided to consider Galactic Cosmic Rays during solar minimum as primary particle input to the simulation.

The spectra corresponding to this radiation environment configuration have been provided by ALENIA-SPAZIO [22] at 1 AU.

The spectra have been modeled in the REMSIM simulation application; due to the time constraints of the project, a significant subset of ions spectra (carbon, oxygen, silicon and iron ions), as well as proton and alpha spectra, have been implemented. The GCR energy spectra modeled are shown in fig. 8.

6.2 Solar Particle Events

Solar event protons and alpha particles have been considered and analysed.

The fluxes versus the particle energy were given by ALENIA-SPAZIO at 1 AU (see fig. 9) [22].

6.3 Strategy

Individual simulations have been performed for each GCR or SPE component corresponding to a single energy spectrum. Then the dosimetric results of individual simulations are weighted according to the relative contribution of the corresponding particle type spectrum, assuming the proton energy spectrum as reference with weight one. The result of this operation gives the following approximate relative weights of GCR components with respect to 100 GCR protons:

- 4 alpha particles,
- 0.127 carbon and oxygen ions,

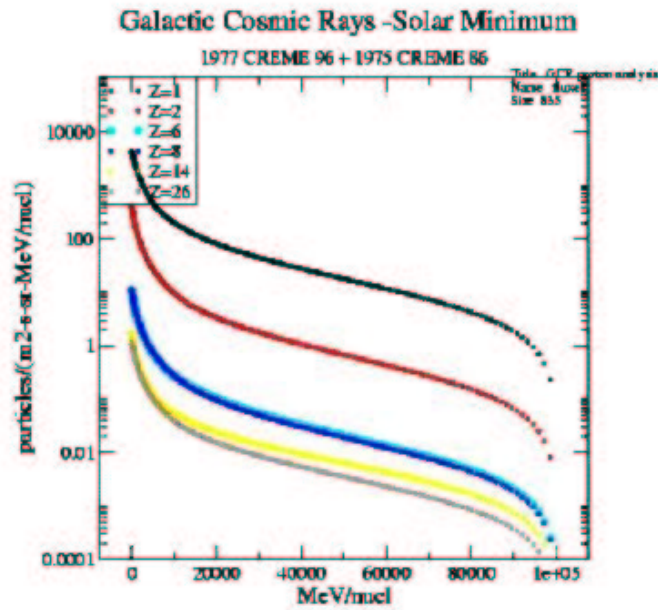


Figure 8: Fluxes of GCR protons, alpha particles and heavier ions versus particle energy. The fluxes are expressed as $\frac{\text{particles}}{m^2-s-sr-MeV/nucleon}$.

- 0.026 silicon ions,
- 0.00186 iron ions.

Similarly, the energy spectrum of SPE alpha particles has been weighted against the one of SPE protons. For 100 SPE protons generated, 0.07 alpha particles are produced approximately.

Single GCR and SPE energy spectra (i.e. corresponding to one particle type) are formatted in ASCII files; they are loaded into the Geant4 REMSIM application as input energy spectra of primary particles. The fluxes are normalised to transform the energy spectra into probability distributions: the energy spectra provided are used to calculate the probability to generate a particle of a given energy according to the corresponding flux.

7 Electromagnetic Physics Verification

A test has been performed to verify at microscopic level the correct activation of electromagnetic physics processes for hadrons and ions in the Geant4 REMSIM application.

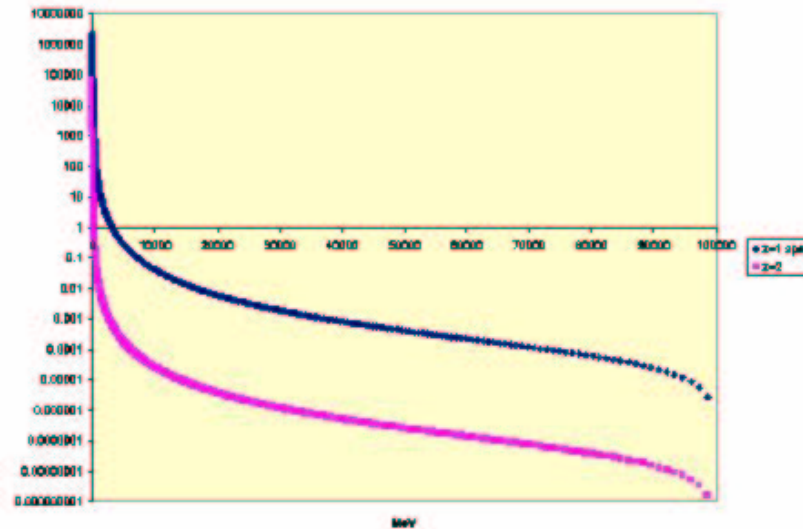


Figure 9: Fluxes of SPE protons (in blue) and alpha particles (in magenta) versus particle energy. The fluxes are expressed as $\frac{\text{particles}}{m^2-s-sr-MeV/nucleon}$.

The models for the electromagnetic interactions of hadrons and ions selected for REMSIM Simulation consists of ICRU parameterisation in their validity range up to 2. MeV, the free electron gas model at lower energies and the Bethe-Bloch model at higher energies.

To verify the correct activation of Geant4 physics in the REMSIM application, a test has been performed to verify the consistency of the application results with respect to protocol data used in medical physics (ICRU Report 49).

Proton and alpha Stopping Power and Continuous Slowing Down Approximation (CSDA) Range are calculated for materials of interest for the REMSIM Geant4 application. The tests have been performed in the following energy ranges:

- from 1 MeV to 10 GeV for protons,
- from 1 MeV to 1 GeV for alpha particles.

The results of the electromagnetic physics verification are compared to protocol data (ICRU Report 49). The protocol data are downloadable in electronic format from the National Institute of Standards and Technology (NIST) web site (www.nist.gov).

7.1 Test experimental set-up

Primary particles are generated in the center of a box filled with a given material. Primary particles can be protons or alpha particles.

The electromagnetic physics is activated in terms of ionisation. The multiple scattering and the fluctuations of energy loss are not active. The maximum step allowed in the box is fixed and the threshold of production of secondaries is fixed to 100. km (secondaries are not generated in this condition). This set-up corresponds to the conditions of the protocol data.

The materials chosen for the tests are water, hydrogen, graphite, nitrogen, oxygen, aluminum, silicon, iron; these materials have been selected because are or constitute the compounds used in the Geant4 REMSIM application.

7.2 Test results

The results of the tests concerning protons are shown in the pictures fig. 10, fig. 11, fig. 12, fig. 13, fig. 14, fig. 15, fig. 16, fig. 17.

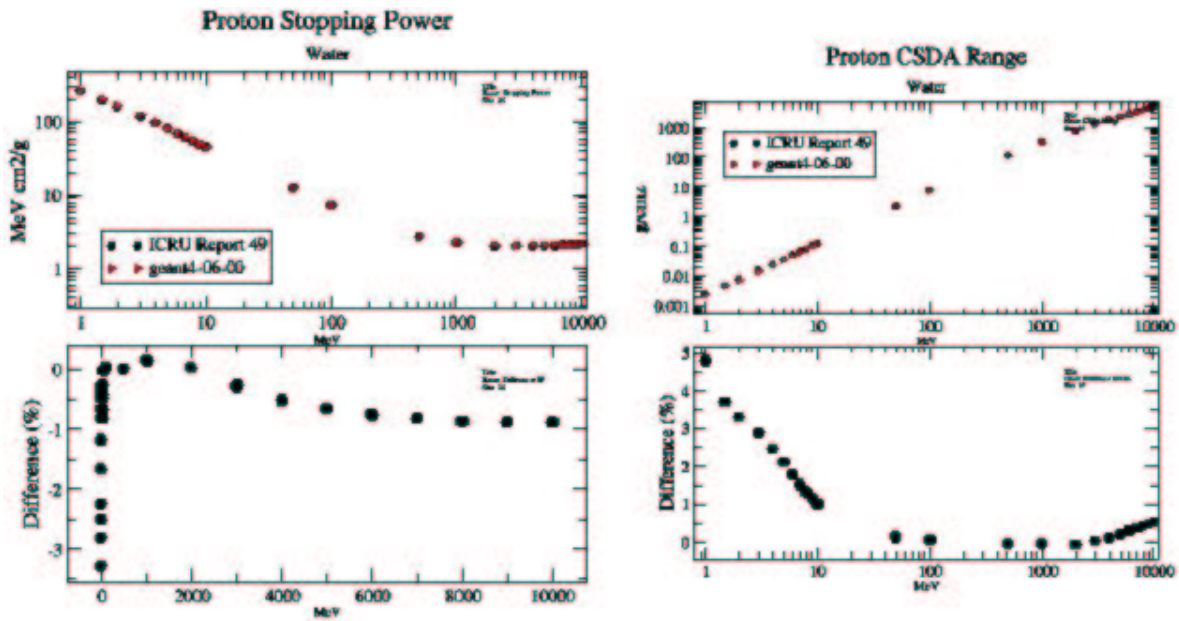


Figure 10: Proton Stopping Power and CSDA Range in water. The difference between Geant4 simulation and protocol data is reported in the lower plots respectively for Stopping Power and CSDA Range.

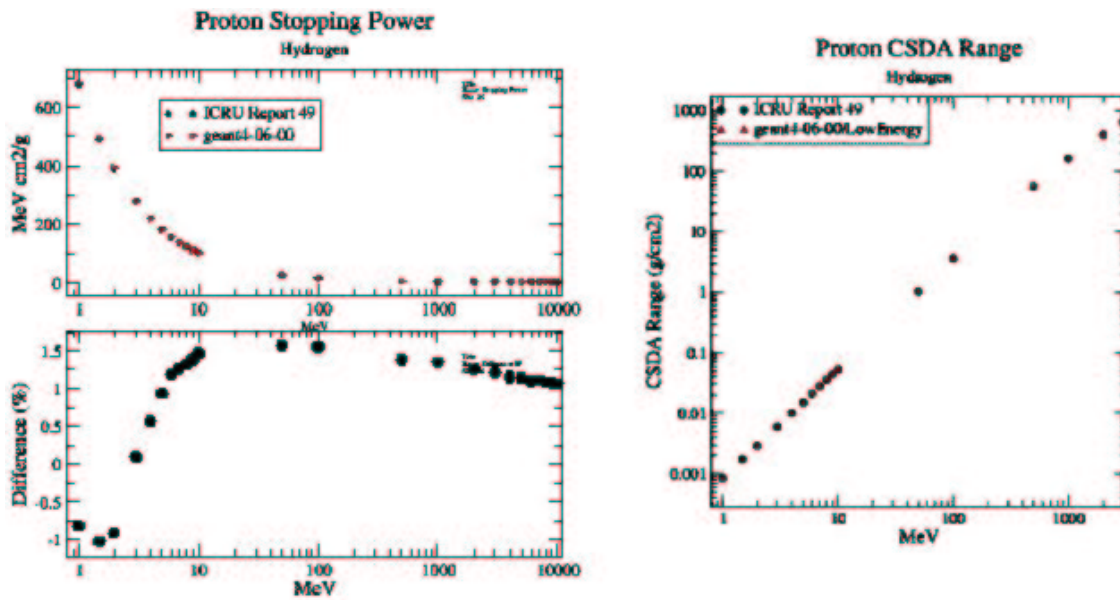


Figure 11: Proton Stopping Power and CSDA Range in hydrogen.

The uncertainties of the protocol data for protons are the following:

- for elements
 - $E < 1\text{MeV}$: 5%
 - $E > 1\text{MeV}$: 2%
- for compounds
 - $E < 1\text{MeV}$: 5%
 - $E > 1\text{MeV}$: 4%

The differences between test results and protocol data are consistent with the errors of the protocol data for all materials, with the exception of graphite for the energy $E = 2\text{MeV}$; in this case the difference is about 4%, while the uncertainty of protocol data is 2% in this case).

The results of the tests concerning alpha particles are shown in fig. 18, fig. 19, fig. 20, fig. 21, fig. 22, fig. 23, fig. 24, fig. 25.

The uncertainties that affect the alpha Stopping Power reported by NIST are the following:

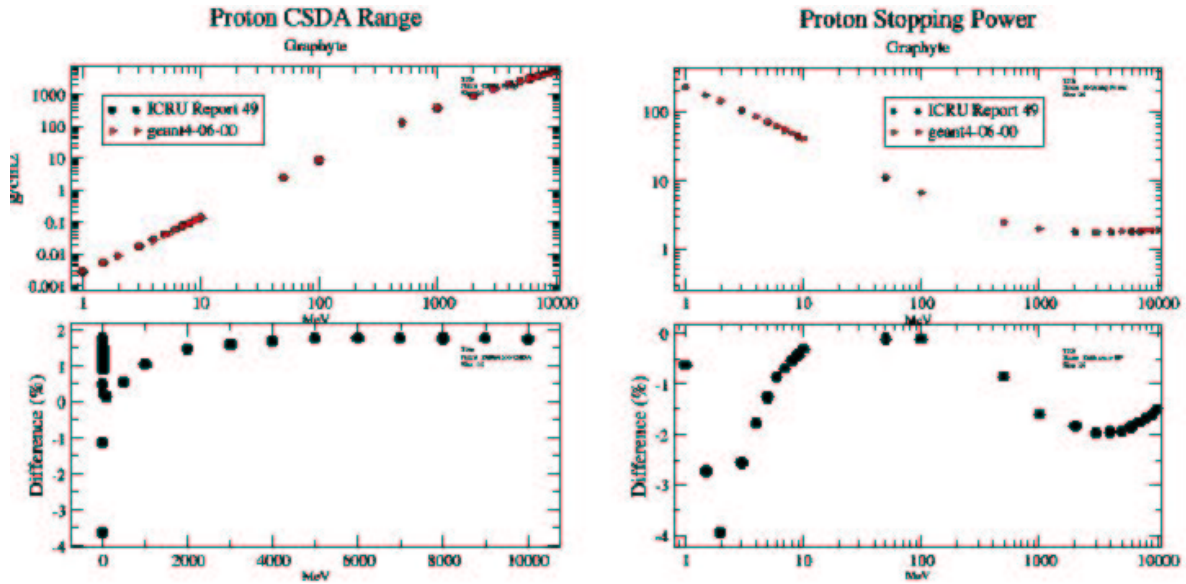


Figure 12: Proton Stopping Power and CSDA Range in graphite. The difference between Geant4 simulation and protocol data is reported in the lower plots respectively for Stopping Power and CSDA Range.

- for elements
 - $E < 2MeV$: 5%
 - $E > 2MeV$: 2%
- for compounds
 - $E < 2MeV$: 5%
 - $E > 2MeV$: 4%

The differences between test results and protocol data are consistent with the errors of the protocol data for all the materials, except for graphite at $6MeV < E < 10MeV$; in this case the difference is about 5/6%, while the uncertainty of protocol data is 2%.

From the test we can infer that the physics processes are activated properly in REMSIM physics list, their reliability with respect to protocol reference is of the order of few percent accuracy.

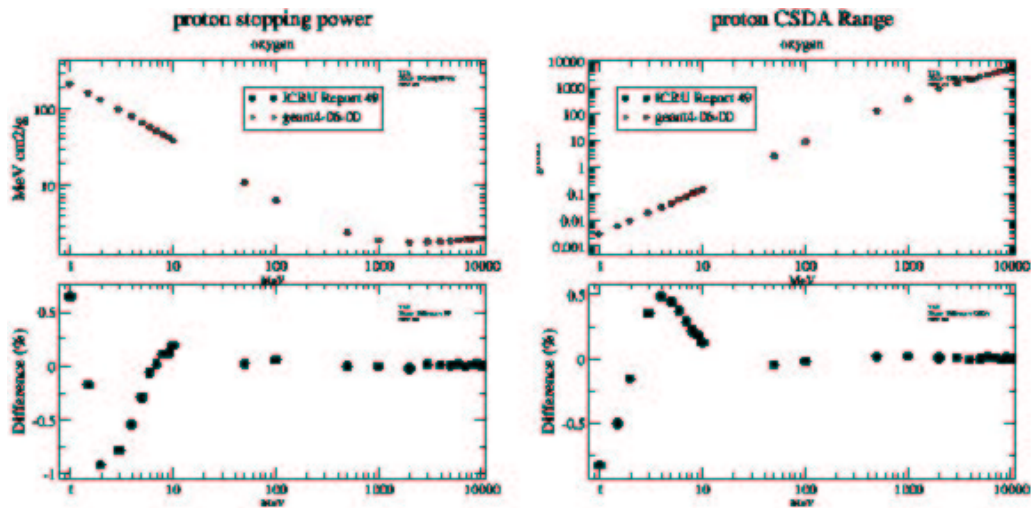


Figure 13: Proton Stopping Power and CSDA Range in oxygen. The difference between Geant4 simulation and protocol data is reported in the lower plots respectively for Stopping Power and CSDA Range.

7.3 Stopping Powers and CSDA Ranges

The Stopping Power and CSDA Range in water have been calculated for some configuration of interest for the following REMSIM simulation study.

The results for protons, alpha particles, carbon ions, oxygen ions, silicon ions, iron ions are shown in fig. 26, 27, 28.

7.4 Optimisation of the application

Geant4 provides the user access to some parameters that control the accuracy of the simulation results. These parameters include the maximum step size and the threshold of production of secondary particles.

Usually the accuracy of the results affects the CPU performance of the simulation. Therefore a study has been performed to optimise the CPU consumption of the REMSIM application without affecting the accuracy of dose calculation.

The maximum step size and the production threshold of secondaries have been fixed in relation to the Astronaut (sensitive detector of the application) geometrical characteris-

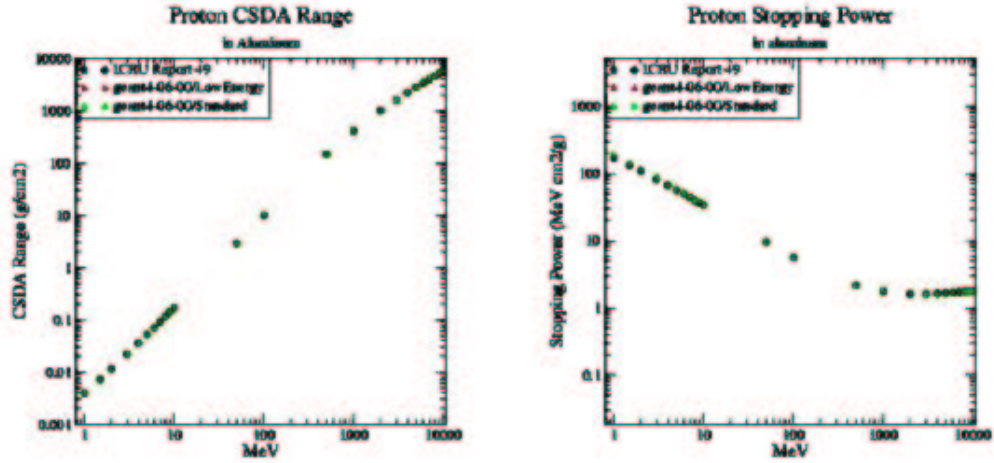


Figure 14: Proton Stopping Power and CSDA Range in aluminum.

tics.

The Astronaut (see fig. 29) is a water box, whose Z-size is 30. cm wide while X-size and Y-size are 5. m wide. The Astronaut is sliced in 30 1. cm wide voxels along Z direction. The energy deposit is collected in every voxel. The primary particles impinge on the Astronaut with an initial direction parallel to Z axis.

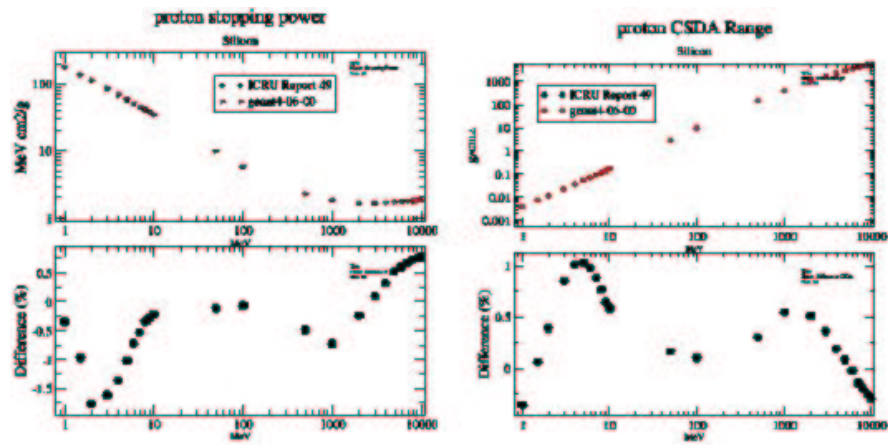


Figure 15: Proton Stopping Power and CSDA Range in silicon. The difference between Geant4 simulation and protocol data is reported in the lower plots respectively for Stopping Power and CSDA Range.

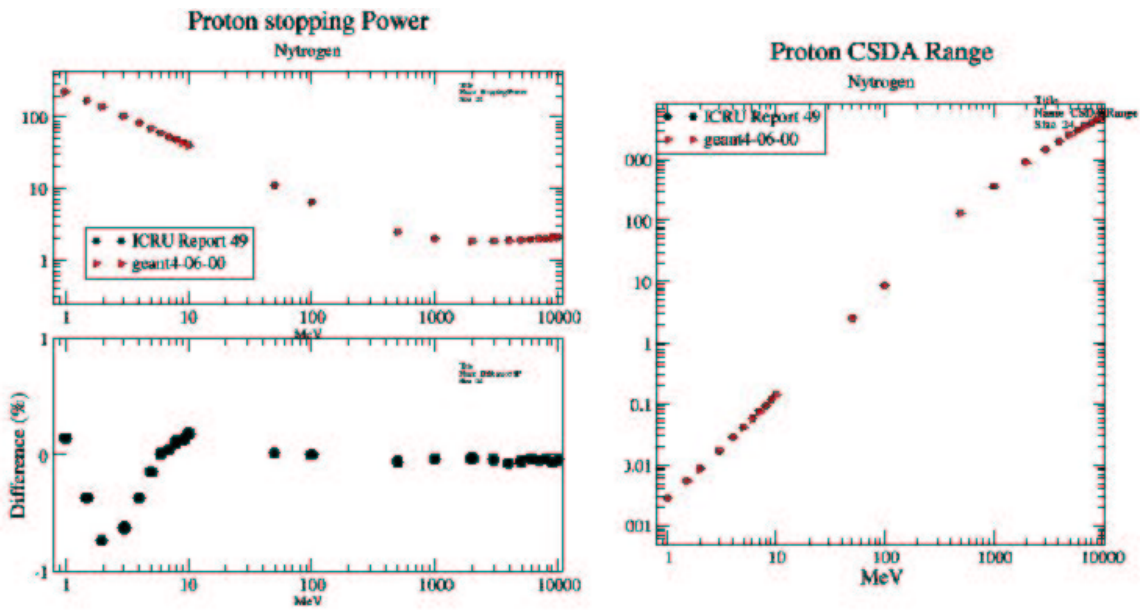


Figure 16: Proton Stopping Power and CSDA Range in nitrogen.

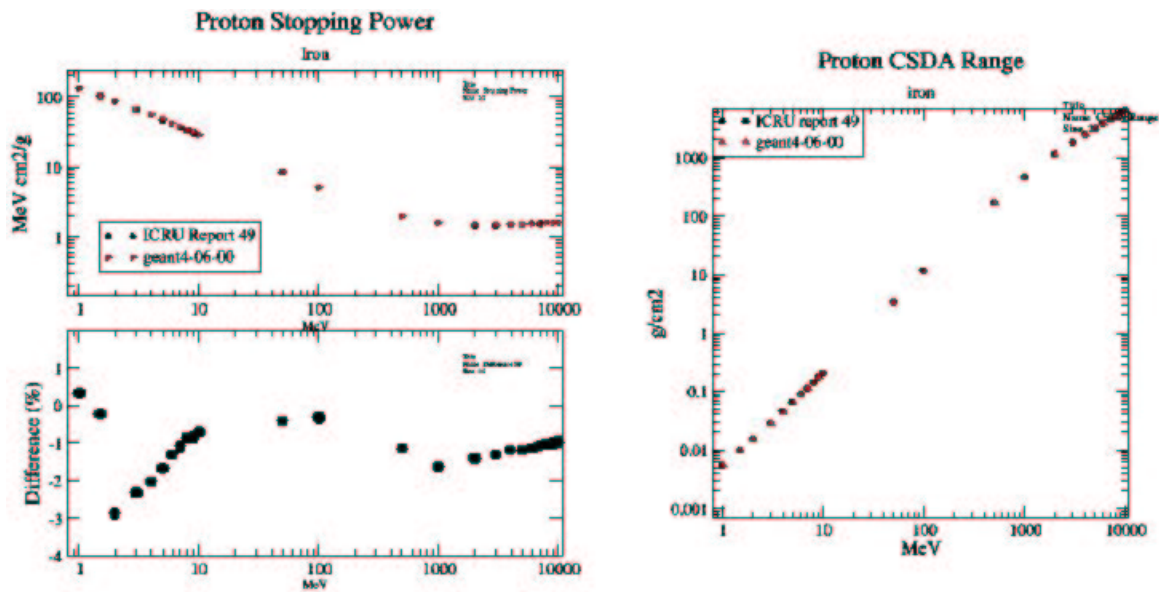


Figure 17: Proton Stopping Power and CSDA Range in iron.

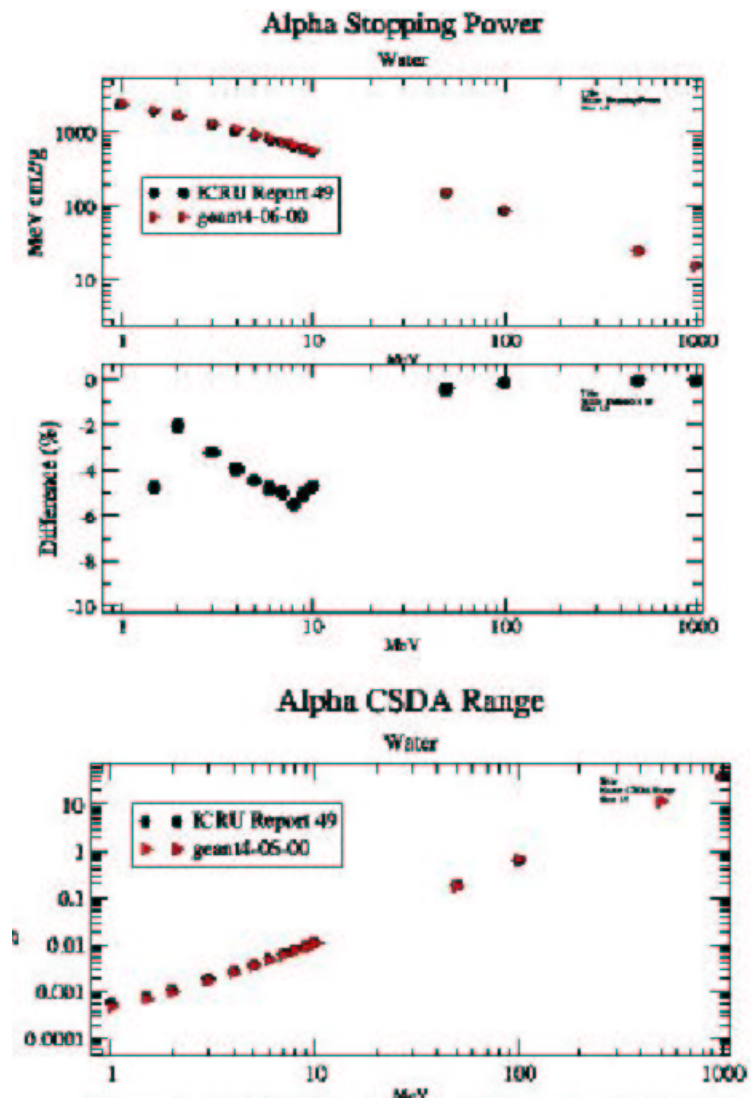


Figure 18: Alpha Stopping Power (higher plot), SP difference between Geant4 test and protocol data (middle plot) and CSDA Range (lower plot) in water.

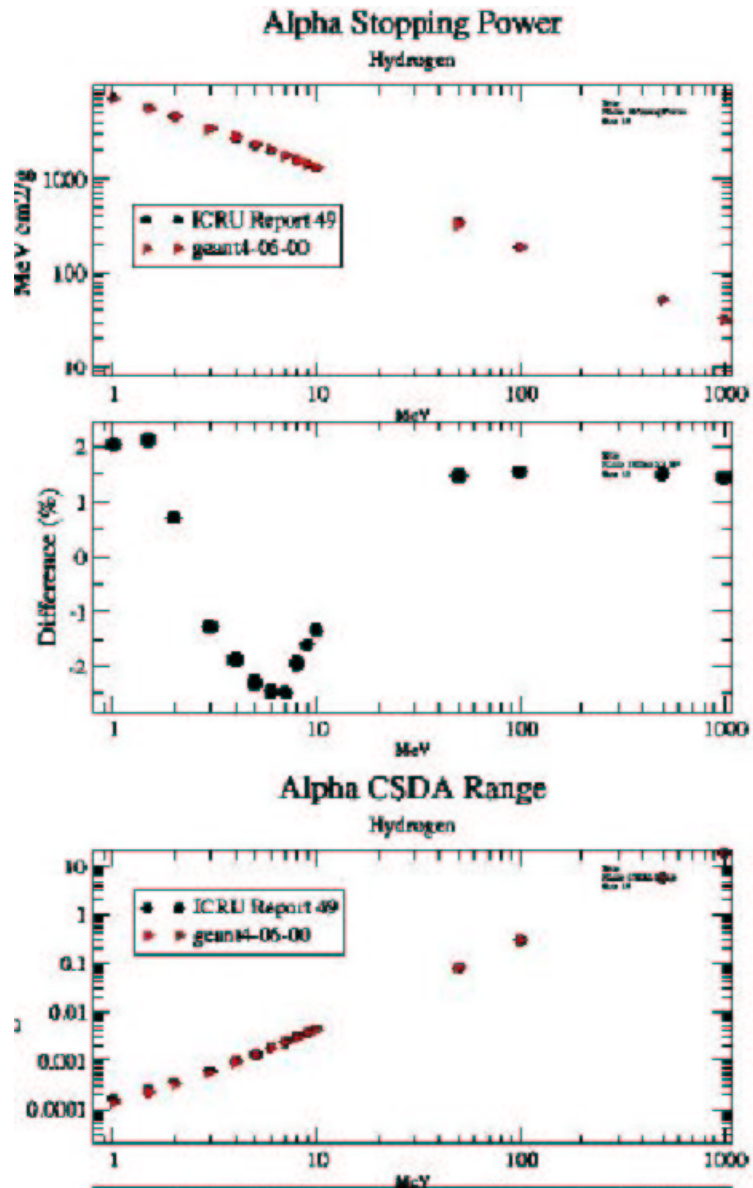


Figure 19: Alpha Stopping Power (higher plot), SP difference between Geant4 test and protocol data (middle plot) and CSDA Range (lower plot) in hydrogen.

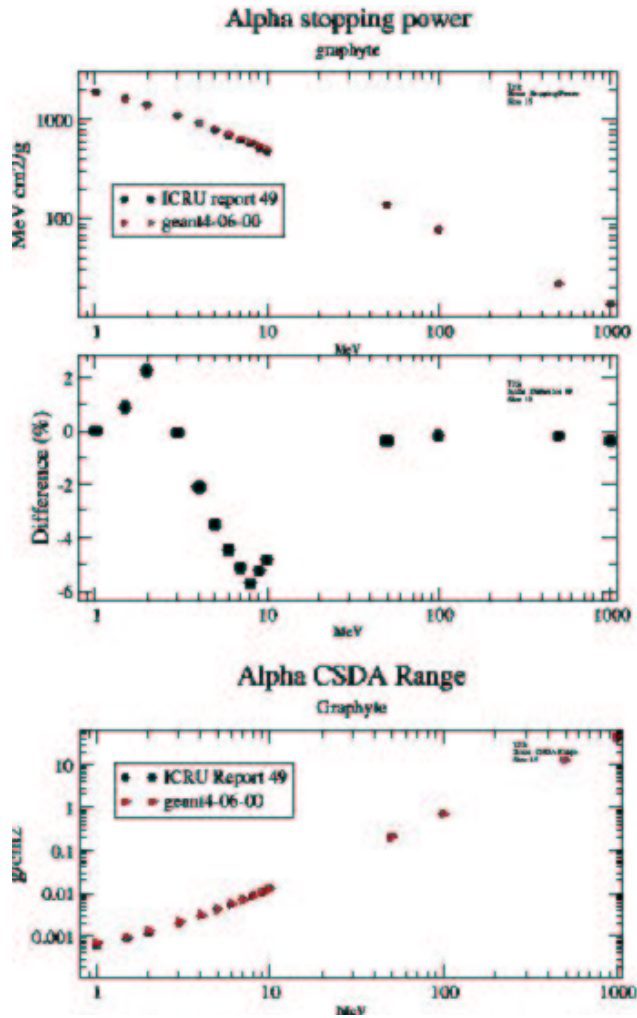


Figure 20: Alpha Stopping Power (higher plot), SP difference between Geant4 test and protocol data (middle plot) and CSDA Range (lower plot) in graphite.

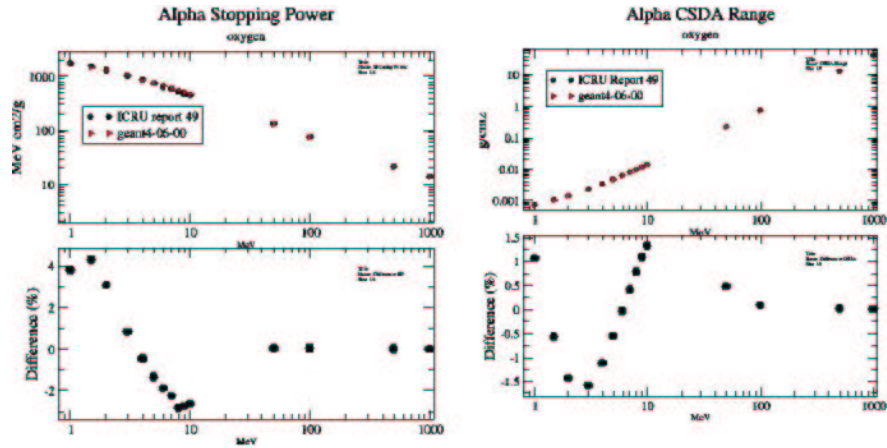


Figure 21: Alpha Stopping Power and CSDA Range in oxygen. The lower plots show respectively the SP and CSDA Range differences between Geant4 test and protocol data.

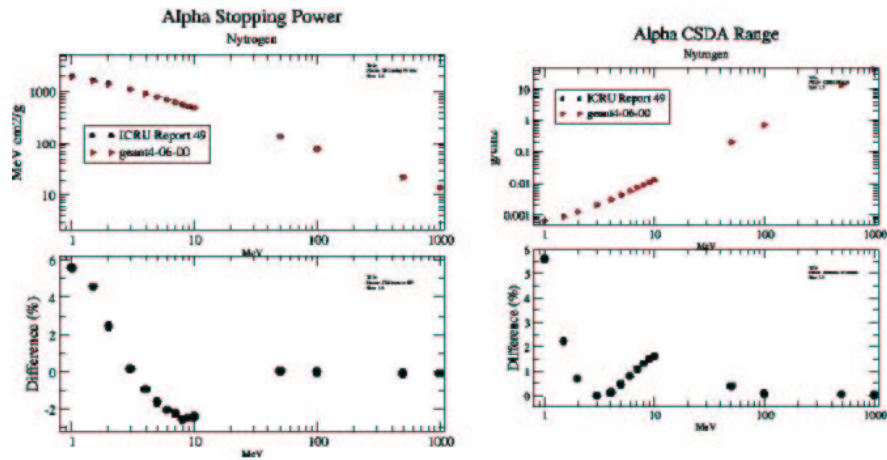


Figure 22: Alpha Stopping Power and CSDA Range in aluminum. The lower plots show respectively the SP and CSDA Range differences between Geant4 test and protocol data.

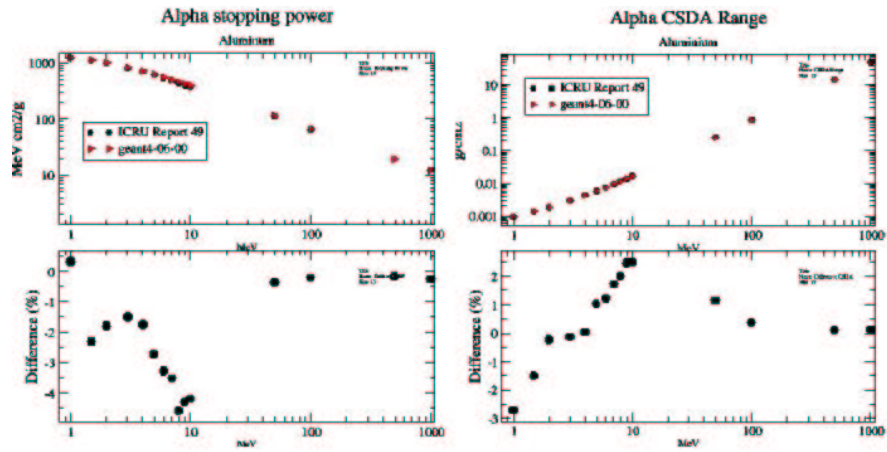


Figure 23: Alpha Stopping Power and CSDA Range in silicon. The lower plots show respectively the SP and CSDA Range differences between Geant4 test and protocol data.

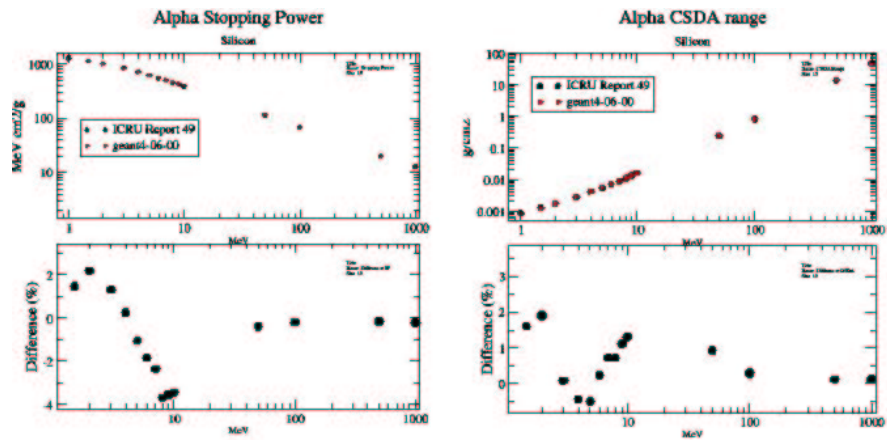


Figure 24: Alpha Stopping Power and CSDA Range in nitrogen. The lower plots show respectively the SP and CSDA Range differences between Geant4 test and protocol data.

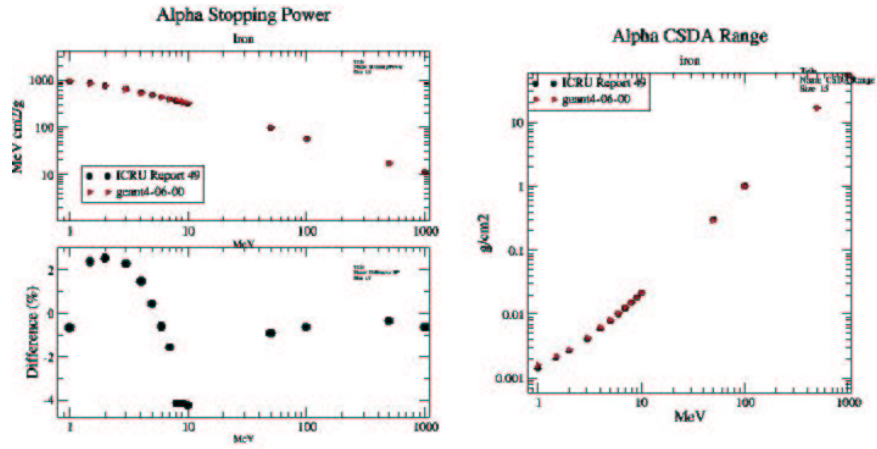


Figure 25: Alpha Stopping Power and CSDA Range in iron.

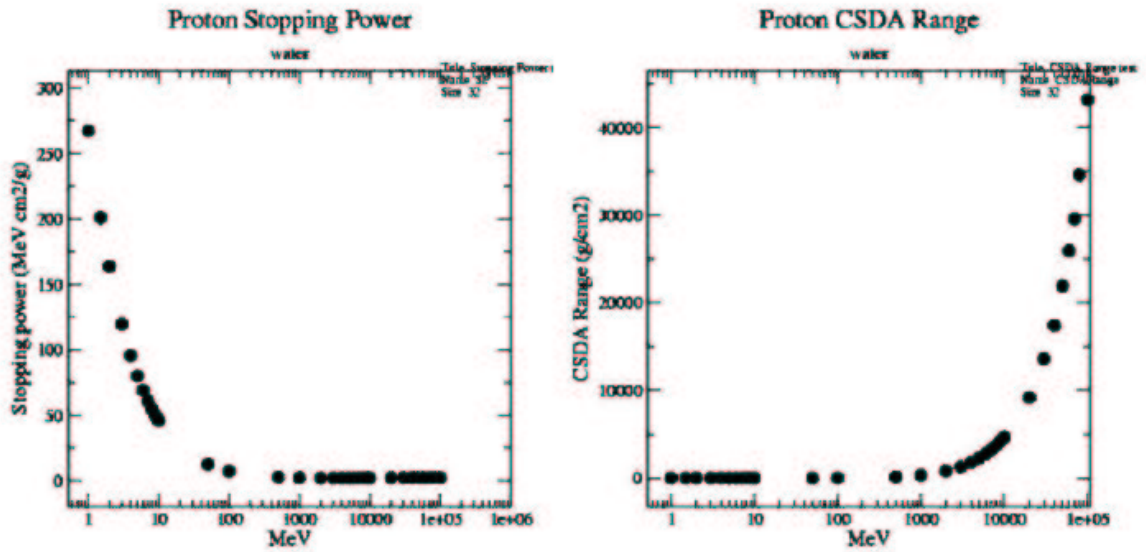


Figure 26: Proton Stopping Power and CSDA Range in water.

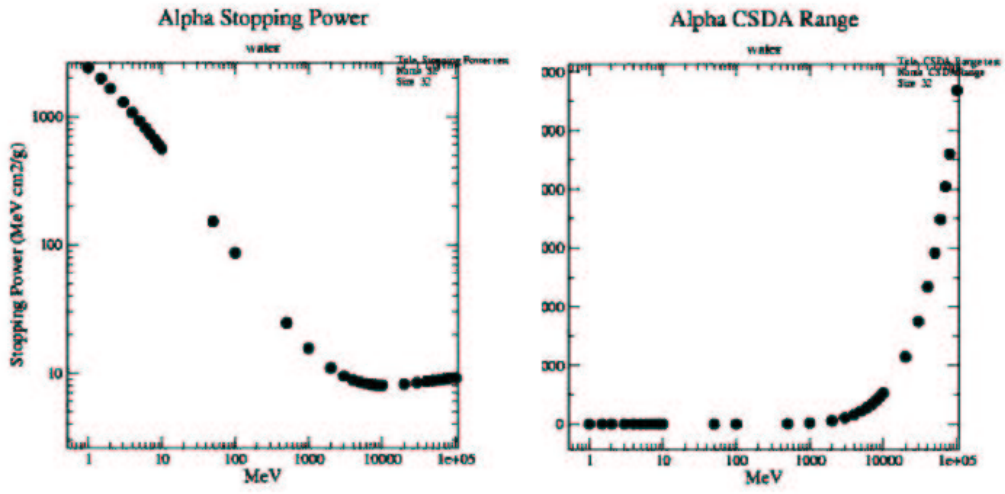


Figure 27: Alpha Stopping Power and CSDA Range in water.

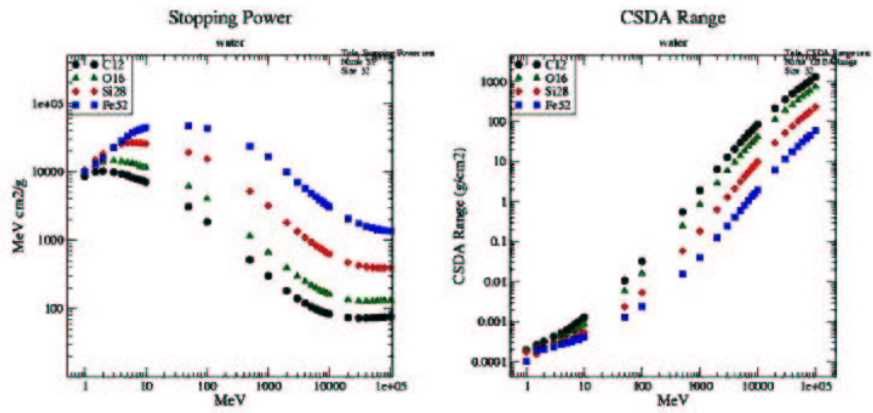


Figure 28: Ion Stopping Power and CSDA Range in water.

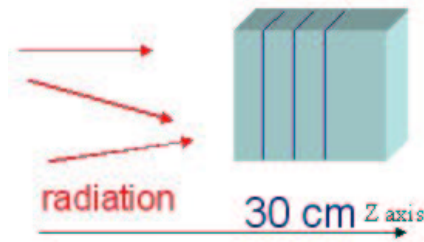


Figure 29: Model of the Astronaut concept.

The maximum step size has been optimised and chosen equal to 1. mm: the energy deposit calculation is not affected as long as the step is significantly smaller than the smallest size of the voxel where the energy deposit is collected (1. cm).

After this optimisation, the threshold of production of secondaries has been fixed.

The threshold (called *cut* in Geant4) is defined in terms of range; a secondary particle is generated if its range is bigger than the value of the cut. Fixing the cut in range properly is important to increase the performance of the software application without affecting the accuracy of the results. The dose calculation does not lose accuracy as long as the cut in range is fixed significantly smaller than the smallest size of the voxel. As a consequence the cut in range has been chosen equal to 1. mm (1/10 of the smallest size of the voxels constituting the Astronaut).

8 Study of vehicle concepts: electromagnetic interactions

The dosimetric study in vehicle concepts followed an incremental method of accuracy in modeling the experimental set-up under study.

This approach has been adopted to study the effect of different aspects of the application independently and to face problems one by one whenever they appeared.

The next sections show the results obtained along the process of increasing the degree of accuracy step by step.

8.1 Model of the experimental set-up

ALENIA-SPAZIO provided a set of sketches of vehicle concepts [24]; their significant conceptual characteristics, relevant to a preliminary simulation study in the REMSIM context, have been identified, and simplified geometrical configurations have been modeled, reflecting these characteristics.

The experimental set-up adopted in this phase of the study corresponds to the model of

the Simplified Inflatable Habitat (SIH) concept shown in fig. 30 [24].

At this stage of the study, the geometrical model provided was simplified to the essential

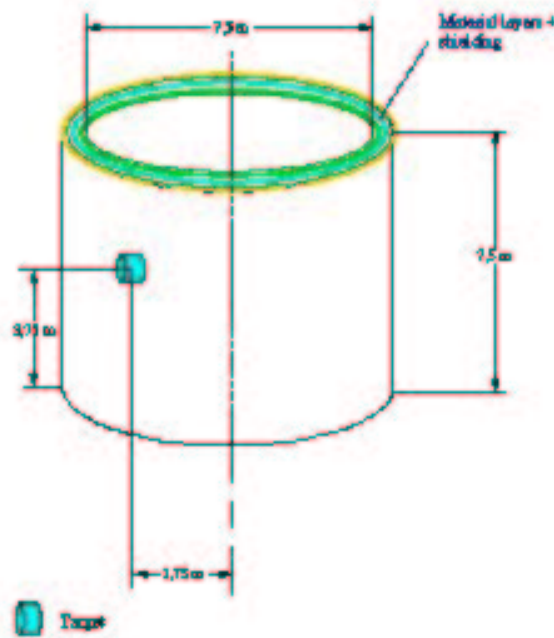


Figure 30: Simplified Inflatable Habitat concept [24]: cylinder consisting of multiple layers of different materials. The target indicates the Astronaut where the dose is calculated.

characteristics suitable for a preliminary evaluation of dosimetric effects in controllable configurations.

This simplification allows to disentangle the physical effects, that are of primary concern at this stage, from geometrical effects that are of secondary importance for the scope of this study. Moreover, the simulation of a simplified set-up allows a quantitative evaluation of the computing resources needed, that was necessary to establish realistic work plan compatible with the available resources.

The simplified geometrical configuration consists of a multilayer box volume, keeping the same material distribution as the original multilayer structure of sketch [24].

The material composition of the multilayer is documented in [24].

Fig. 31 shows the experimental set-up of the study. The multilayer consists of a fixed component, corresponding to the basic vehicle structure, and of optional components representing the shielding.

The thickness and material of the shielding layer can be selected; different options mod-

eled consist of water and polyethylene as materials; thicknesses of 5. and 10. cm have been defined as example cases.



Figure 31: Experimental set-up: the primary particles impinge on the multilayer structure, the highest simplification of the SIH shown in fig. 30, and on the Astronaut.

The primary particle beam, generated with a direction parallel to Z axis, impinges on the multilayer; the energy deposit is collected in the Astronaut. The Astronaut is represented by a water box, sliced along the Z direction into 30 1. cm wide voxels. This set-up allows to study the dose absorbed in relation to the depth in the Astronaut.

The electromagnetic physics is activated for all the particles involved in the simulation as described in subsection 5.1.6.

The initial energy of primary particles entering the Astronaut volume or outgoing it is registered in histograms; this information allows to analyse which component of the GCR primary particles is shielded by the material in front of the Astronaut.

8.2 Strategy of the study

The study has been articulated through two steps:

1. monochromatic beams of particles, at selected energies of interest for the project, shot against the geometrical set-up described above,
2. particle beams modulated according to GCR energy spectra hitting the same experimental set-up.

In the second case additional dosimetric studies have been performed selecting the higher energy portion of the GCR spectra, to ensure an adequate statistical significance also for the depleted regions of the GCR spectra.

Different shielding solutions have been studied, selecting shielding material type and thickness.

8.3 First iteration: study with monochromatic beams

The dosimetric study has been performed with monochromatic beams of protons, alpha particles, C-12, O-16, Si-28, Fe-52 ions impinging on the multilayer structure(see fig. 31), both without any shielding and with a 10 cm thick water shielding.

The purpose of this study is to gain basic information of the effects of shielding materials as a function of energy for a variety of particles of interest for REMSIM.

Initial energies of the monochromatic beams of 100. MeV, 1 GeV, 10. GeV, 100. GeV, spanning the region of the GCR spectra have been selected for this preliminary study. Additional simulations were performed with appropriate initial energies to observe the the Bragg peak within the Astronaut in the presence of different shielding configurations.

The following results are obtained with the basic multilayer structure without any shielding.

Fig. 32, 33, 34 represent the energy deposit in the Astronaut as a function of the depth resulting from monochromatic proton beams.

From the results obtained we can infer that protons with initial energy

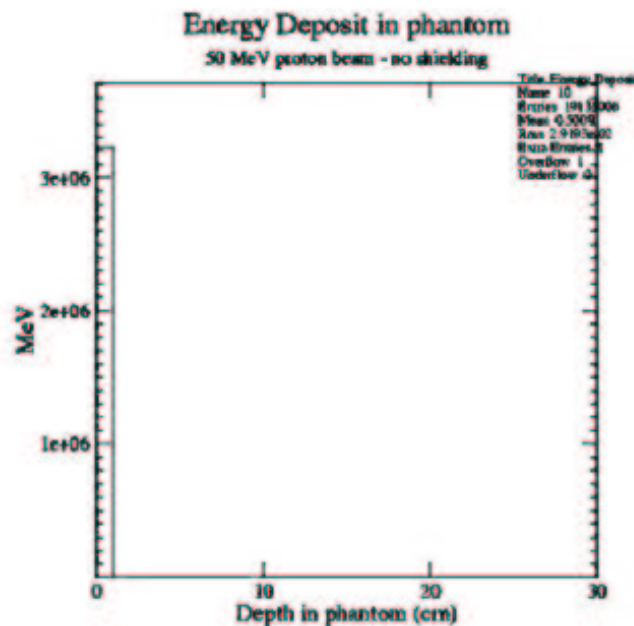


Figure 32: Energy deposit in the Astronaut resulting from 50 MeV proton.

- $E < \sim 50 MeV$ are stopped by the basic multilayer structure,

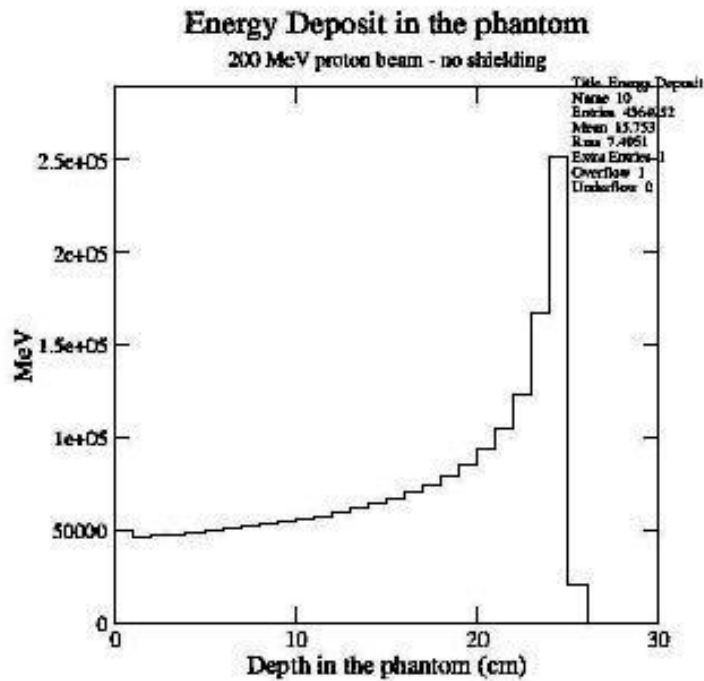


Figure 33: Energy deposit in the Astronaut resulting from a 200 MeV proton beam.

- $\sim 50\text{MeV} < E < \sim 250\text{MeV}$ are absorbed in the Astronaut,
- $E > \sim 250\text{MeV}$ traverse the Astronaut,
- $E > \sim 1\text{GeV}$ behave as minimum ionising particles traversing the whole phantom thickness; the energy deposit is similar for primary protons with initial energy in the range $1\text{GeV} - 100\text{GeV}$.

The same study has been performed for alpha particles hitting the basic multilayer structure. Fig. 35, 36, 37 show the corresponding results. From the results obtained, we can deduce that alpha particles with initial energy

- $E < \sim 200\text{MeV}$ are stopped by the multilayer,
- $\sim 200\text{MeV} < E < \sim 900\text{MeV}$ are absorbed in the Astronaut,
- $E > \sim 900\text{MeV}$ traverse the Astronaut,

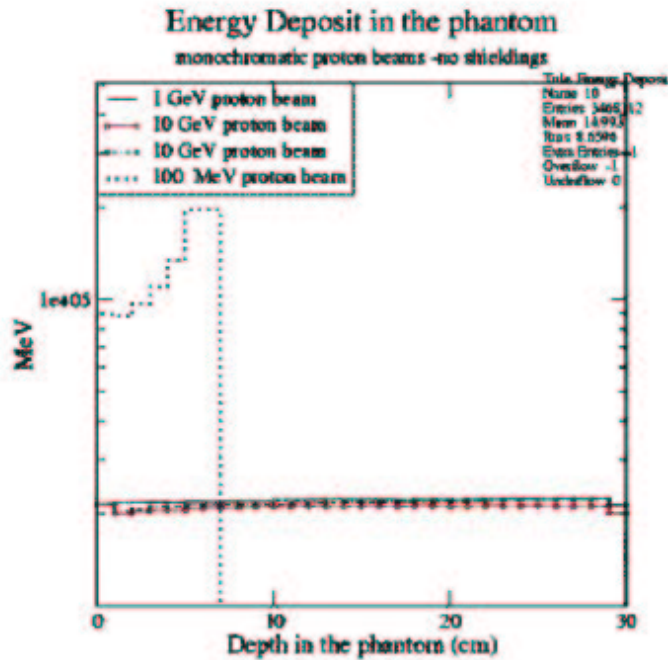


Figure 34: Energy deposit in the Astronaut resulting from monochromatic (100 MeV, 1 GeV, 10 GeV, 100 GeV) proton beams.

- $E > 10\text{GeV}$ behave as minimum ionising particles traversing the whole phantom thickness; the energy deposit is similar for alpha particles with primary energy in range $1\text{GeV} - 100\text{GeV}$.

Fig. 38 and 39 show the results of simulation with C-12 ions as primary particles in the same geometrical configuration. C-12 ions with initial energy

- $E < \sim 1\text{GeV}$ are stopped by the multilayer,
- $\sim 1\text{GeV} < E < \sim 5\text{GeV}$ are absorbed in the Astronaut,
- $E > \sim 5\text{GeV}$ traverse the Astronaut,
- $E > \sim 10\text{GeV}$ behave as minimum ionising particles traversing the whole phantom thickness; the energy deposit is similar C-12 ions with primary energy in range $10\text{GeV} - 100\text{GeV}$.

Fig. 40 and 41 show the results of the simulation with O-16 ions as primary particles. O-16 ions with initial energy

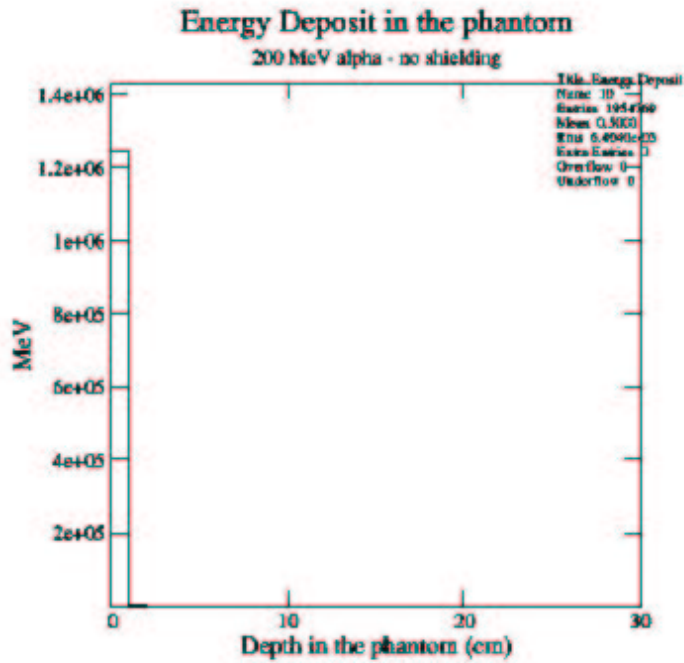


Figure 35: Energy deposit in the Astronaut resulting from a 200 MeV alpha beam.

- $E < \sim 1\text{GeV}$ are stopped by the multilayer,
- $\sim 1\text{GeV} < E < \sim 8\text{GeV}$ are absorbed in the Astronaut,
- $E > \sim 8\text{GeV}$ traverse the phantom,
- $E > \sim 10\text{GeV}$ behave as minimum ionising particles traversing the whole phantom thickness, the energy deposit is similar for impinging O-16 ions with initial energy in range $10\text{GeV} - 100\text{GeV}$.

From fig. 42 we can infer that primary Si-28 ions with initial energy

- $E < \sim 3\text{GeV}$ are stopped by the multilayer,
- $\sim 3\text{GeV} < E < \sim 20\text{GeV}$ are absorbed in the Astronaut,
- $E > \sim 22\text{GeV}$ traverse the phantom,

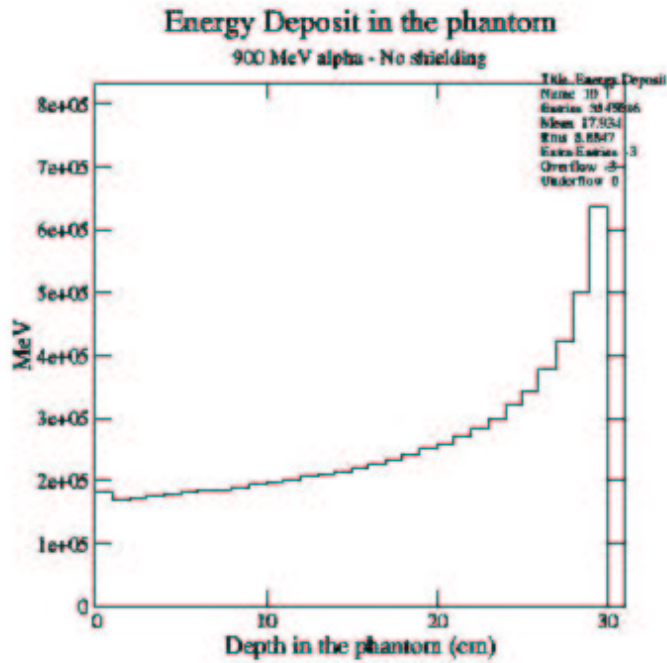


Figure 36: Energy deposit in the Astronaut resulting from a 900 MeV alpha beam.

- $E > \sim 50 GeV$ behave as minimum ionising particles traversing the whole phantom thickness, the energy deposit is similar for Si-28 ions with initial energy in range $50 GeV - 100 GeV$.

Fig. 43 shows that primary Fe-52 ions with initial energy

- $E < \sim 15 GeV$ are stopped by the multilayer,
- $\sim 15 GeV < E < \sim 60 GeV$ are absorbed in the Astronaut,
- $E > \sim 60 GeV$ traverse the phantom.

Monochromatic beams of protons, alpha particles, C-12, O-16, Si-28 and Fe-52 ions are shot against the basic multilayer structure complemented by a 10. cm water shield. The experimental set-up is shown in fig. 44. The results for simulations with protons as primary particles are shown in fig. 45 and in fig. 46. Protons with initial energy

- $E < \sim 100 MeV$ are stopped by the multilayer with shielding,

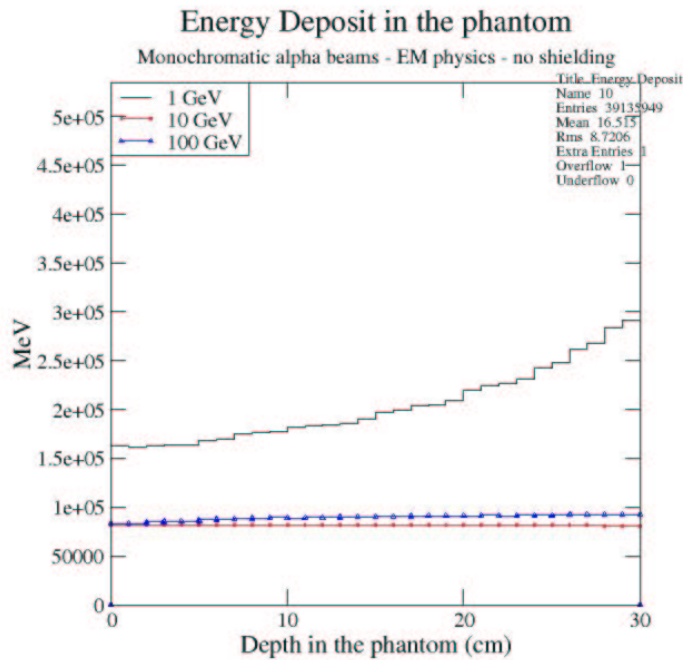


Figure 37: Energy deposit in the Astronaut resulting from a 1 GeV, 10 GeV, 100 GeV alpha beam.

- $\sim 100\text{MeV} < E < \sim 500\text{MeV}$ are absorbed in the Astronaut,
- $E > \sim 500\text{MeV}$ traverse the Astronaut,
- $E > \sim 1\text{GeV}$ behave as minimum ionising particles traversing the whole phantom thickness; the energy deposit is similar for primary protons with energy in the range $1\text{GeV} - 100\text{GeV}$.

The results for incident primary protons in the two geometrical configurations (no shielding, 10. cm water shielding) are collected in table 1. Similar results can be obtained analysing the effect of 10. cm water shielding on alpha particles and heavier ions.

Fig. 47 and 48 show the results of the simulation for primary alpha particles in the experimental set-up shown in fig. 44. Alpha particles with initial energy

- $E < \sim 500\text{MeV}$ are stopped by the multilayer structure with 10. cm water shielding,
- $\sim 500\text{MeV} < E < \sim 1\text{GeV}$ are absorbed in the Astronaut,

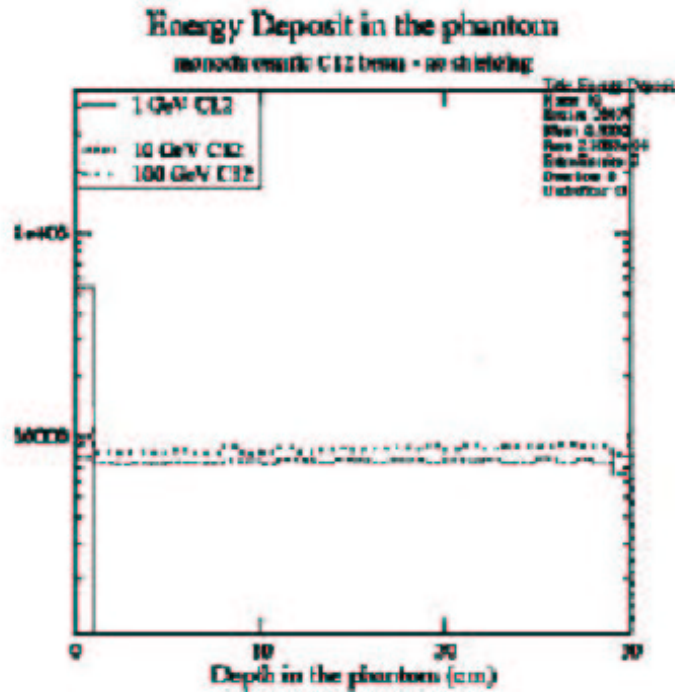


Figure 38: Energy deposit in the Astronaut resulting from a 1 GeV, 10 GeV, 100 GeV C-12 ion beam.

- $E > \sim 10\text{GeV}$ behave as minimum ionising particles traversing the whole phantom thickness; the energy deposit is similar for primary alpha particles with initial energy in the range $10\text{GeV} - 100\text{GeV}$

The results showing the different behaviour of alpha particles in the analysed experimental set-ups are collected in table 2. O-16 ions with initial energy

- $E < \sim 5\text{GeV}$ are stopped by the multilayer with 10. cm water shielding,
- $\sim 5\text{GeV} < E < \sim 10\text{GeV}$ are absorbed in the Astronaut,
- $E > \sim 10\text{GeV}$ traverse the Astronaut,

as shown in fig. 49. The results showing the different behaviour of O-16 ions in the analysed experimental set-ups are collected in table 3. Si-28 ions with initial energy

- $E < \sim 10\text{GeV}$ are stopped by the multilayer with 10. cm water shielding,
- $\sim 10\text{GeV} < E < \sim 25\text{GeV}$ are absorbed in the Astronaut,

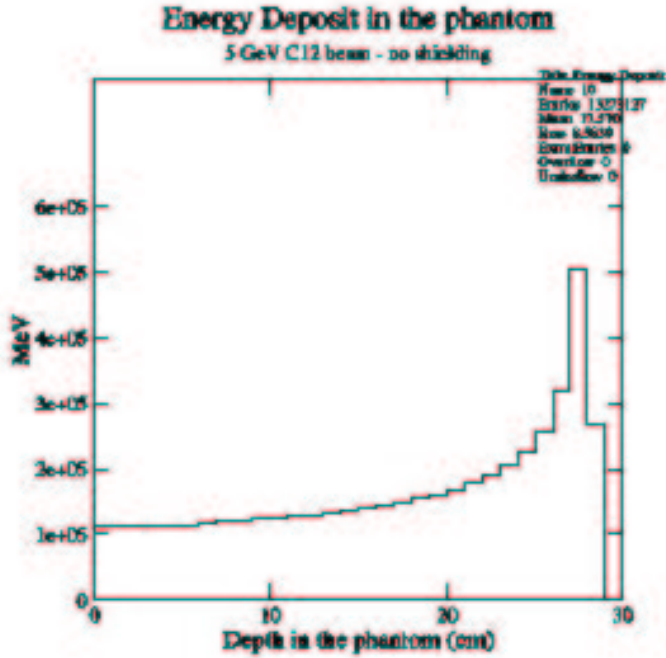


Figure 39: Energy deposit in the Astronaut resulting from a 5 GeV C-12 ion beam.

Table 1: Results for incident protons: region1 = radiation stopped by the vehicle concept, region2 = radiation absorbed in the Astronaut, region3 = radiation traversing the Astronaut.

	no shielding	10 cm water shielding
Region1	$E < \sim 50 MeV$	$E < \sim 100 MeV$
Region2	$\sim 50 MeV < E < \sim 250 MeV$	$\sim 100 MeV < E < \sim 500 MeV$
Region3	$E > \sim 250 MeV$	$E > \sim 500 MeV$

Table 2: Results for incident alpha: region1 = radiation stopped by the vehicle concept, region2 = radiation absorbed by the Astronaut, region3 = radiation outgoing from the Astronaut.

	no shielding	10 cm water shielding
Region1	$E < \sim 200 MeV$	$E < \sim 500 MeV$
Region2	$\sim 200 MeV < E < \sim 900 MeV$	$\sim 500 MeV < E < \sim 1 GeV$
Region3	$E > \sim 900 MeV$	$E > \sim 1 GeV$.

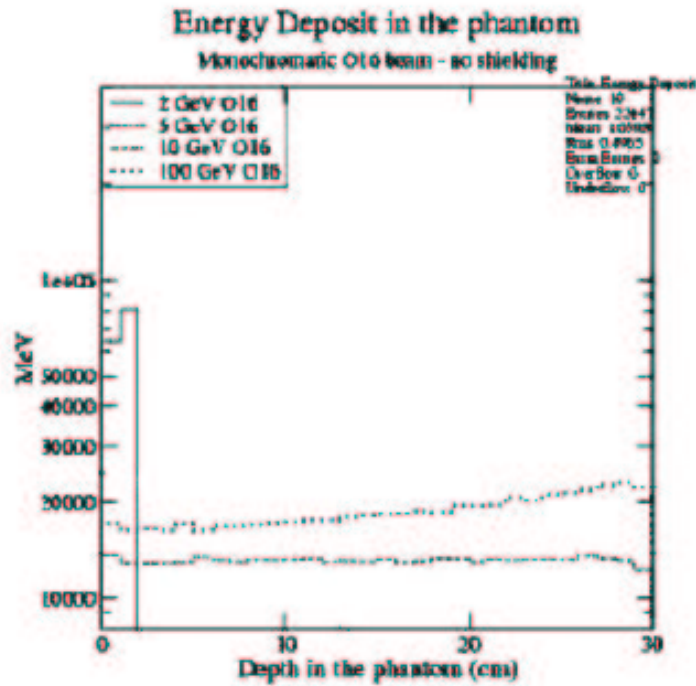


Figure 40: Energy deposit in the Astronaut resulting from a 2 GeV, 10 GeV, 100 GeV O-16 ion beam.

- $E > \sim 25 GeV$ traverse the Astronaut,

as shown in fig. 50.

The results showing the different behaviour of Si-28 ions in the analysed experimental set-ups are collected in table 4.

Fe-52 ions with initial energy

- $E < \sim 30 GeV$ are stopped by the multilayer with 10. cm water shielding,
- $\sim 30 GeV < E < \sim 80 GeV$ are absorbed in the Astronaut,
- $E > \sim 80 GeV$ traverse the Astronaut,

as shown in fig. 51.

The results showing the different behaviour of Fe-52 ions in the analysed experimental set-ups are collected in table 5.

Table 3: Results for incident O-16: region1 = radiation stopped by the vehicle concept, region2 = radiation absorbed by the Astronaut, region3 = radiation outgoing from the Astronaut.

	no shielding	10. cm water shielding
Region1	$E < \sim 1\text{GeV}$	$E < \sim 5\text{GeV}$
Region2	$\sim 1\text{GeV} < E < \sim 8\text{GeV}$	$\sim 5\text{GeV} < E < \sim 10\text{GeV}$
Region3	$E > \sim 8\text{GeV}$	$E > \sim 10\text{GeV}$

Table 4: Results for incident Si-28: region1 = radiation stopped by the vehicle concept, region2 = radiation absorbed in the Astronaut, region3 = radiation outgoing from the Astronaut.

	no shielding	10 cm water shielding
Region1	$E < \sim 3\text{GeV}$	$E < \sim 10\text{GeV}$
Region2	$\sim 3\text{GeV} < E < \sim 20\text{GeV}$	$\sim 10\text{GeV} < E < \sim 25\text{GeV}$
Region3	$E > \sim 20\text{GeV}$	$E > \sim 25\text{GeV}$

Table 5: Results for Fe-52: region1 = radiation stopped by the vehicle concept, region2 = radiation absorbed in the Astronaut, region3 = radiation outgoing from the Astronaut.

	no shielding	10. cm water shielding
Region1	$E < \sim 15\text{GeV}$	$E < \sim 30\text{GeV}$
Region2	$\sim 15\text{GeV} < E < \sim 60\text{GeV}$	$\sim 30\text{GeV} < E < \sim 80\text{GeV}$
Region3	$E > \sim 60\text{GeV}$	$E > \sim 80\text{GeV}$

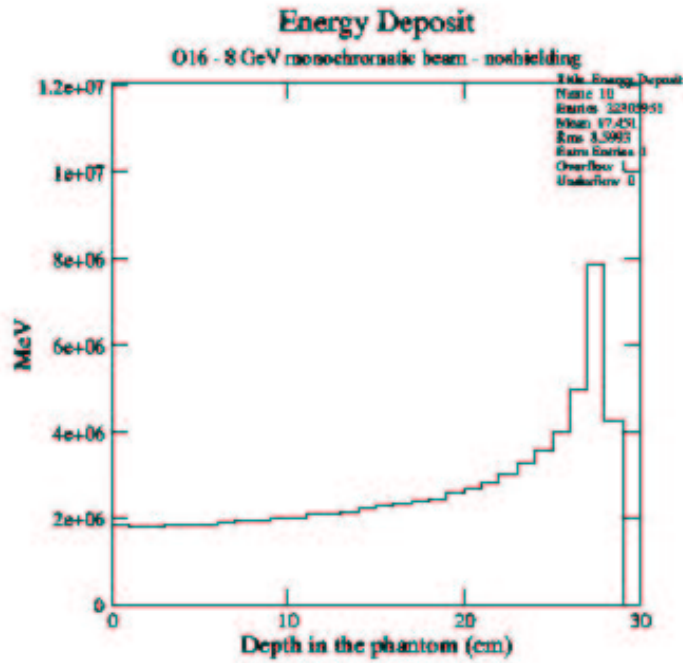


Figure 41: Energy deposit in the Astronaut resulting from a 8 GeV O-16 ion beam.

8.3.1 Conclusions from the study with monochromatic beams

The effect of the shielding layer consists in shifting the energy range of incident particles absorbed in the Astronaut to higher values.

For primaries that behave as minimum ionising particles the presence of a shielding structure is completely irrelevant.

From these first results we can infer that the core of the radioprotection study is the evaluation of possible shielding materials and thicknesses that optimises the shift effect of the shielding itself on the basis of the energy spectra of primary particles in physically relevant configurations (Galactic Cosmic Rays and Solar Particle Events).

The next subsection is dedicated to the analysis of different shielding solutions, taking into account the Galactic Cosmic Rays energy spectra.

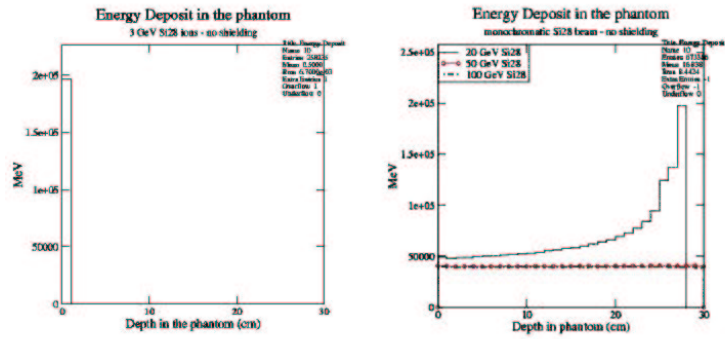


Figure 42: Energy deposit in the Astronaut resulting from a 3 GeV (first plot), 20 GeV, 50 GeV, 100 GeV Si-28 ion beam.

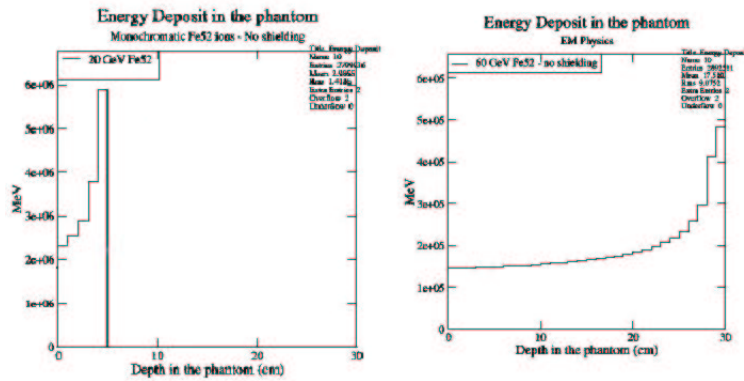


Figure 43: Energy deposit in the Astronaut resulting from 20 GeV (first plot) and 60 GeV Fe-52 ion beam.

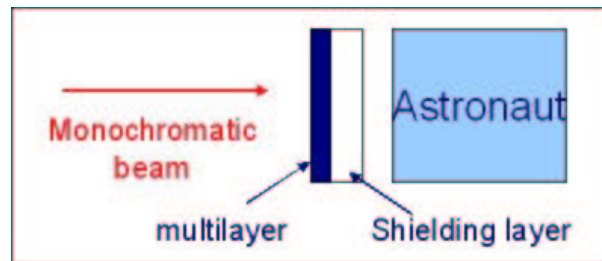


Figure 44: Experimental set-up: particle beam impinges on the multilayer + 10. cm water shielding.

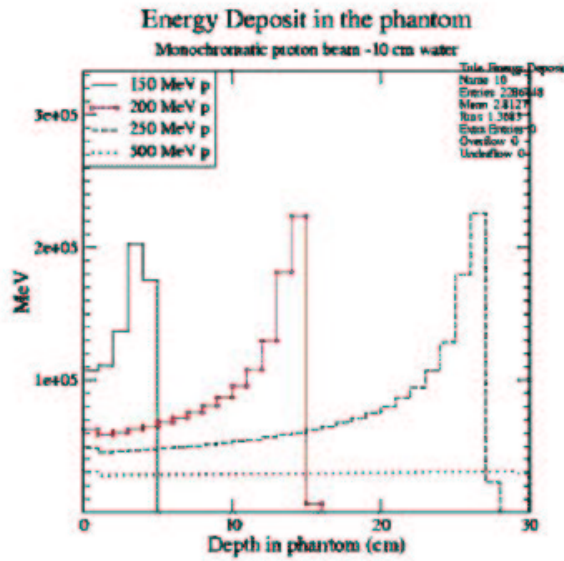


Figure 45: Energy deposit in the Astronaut resulting from 150. MeV, 200. MeV, 250. MeV, 500. MeV proton beam with 10. cm water shielding.

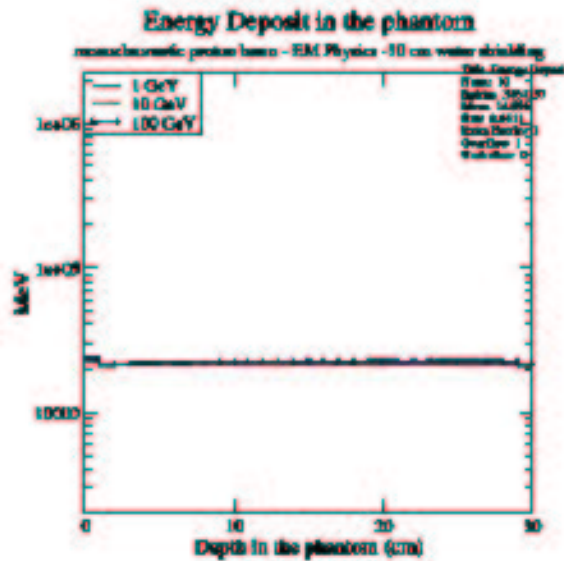


Figure 46: Energy deposit in the Astronaut resulting from 1. GeV, 10. GeV, 100. GeV proton beams with 10. cm water shielding.

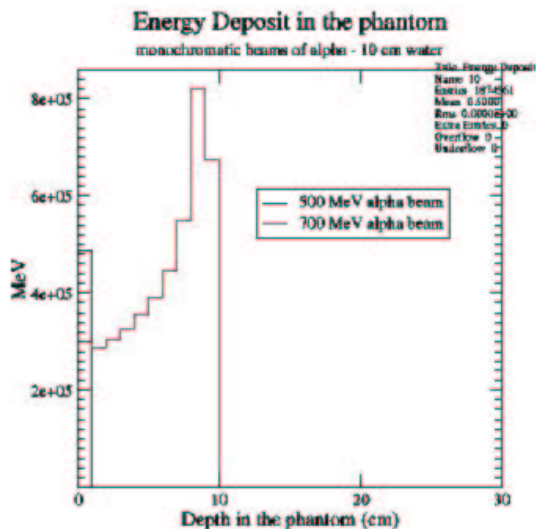


Figure 47: Energy deposit in the Astronaut resulting from 500. MeV, 700. MeV primary alpha particle beams incident on the multilayer structure with 10. cm water shielding.

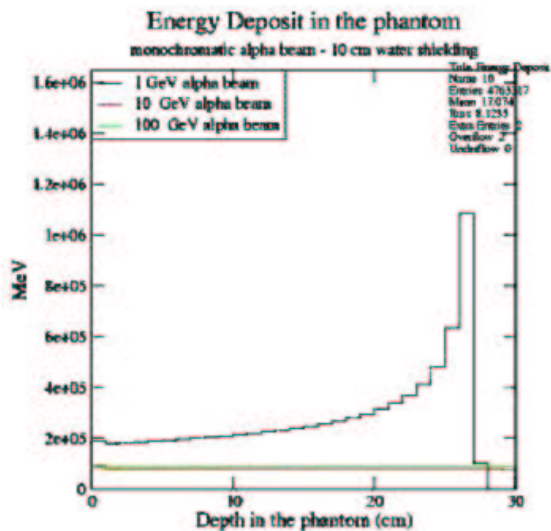


Figure 48: Energy deposit in the Astronaut resulting from 1. GeV, 10. GeV, 100. GeV primary alpha particle beams incident on the multilayer structure with 10. cm water shielding.

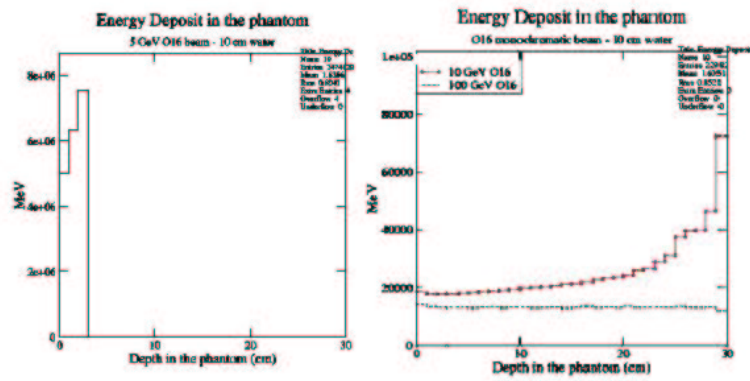


Figure 49: Energy deposit in the Astronaut resulting from 5. GeV (first plot), 10. GeV, 100. GeV (second plot) primary O-16 ions incident on the multilayer structure with 10. cm water shielding.

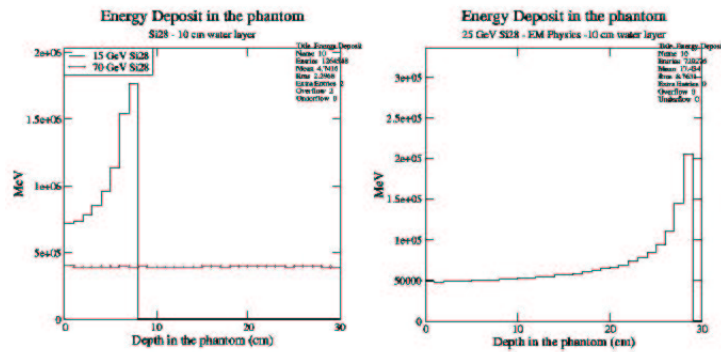


Figure 50: Energy deposit in the Astronaut resulting from 15. GeV, 70. GeV (first plot), 25. GeV Si-28 ions incident on the multilayer structure with 10. cm water shielding.

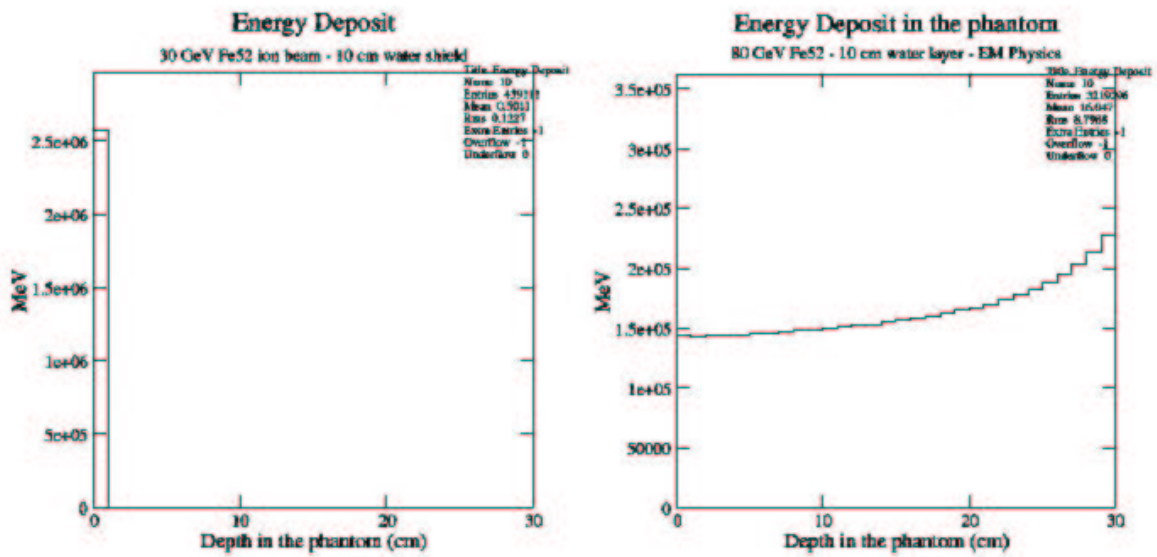


Figure 51: Energy deposit in the Astronaut resulting from 30. GeV (first plot), 80 GeV (second plot) Fe-52 ions incident on the multilayer structure with 10. cm water shielding.

8.4 GCR rays on vehicle concepts

This subsection illustrates the results of a similar study with Galactic Cosmic Rays as primary particles, taking into account their full energy spectra. The experimental set-up is shown in fig. 52. The vehicle configurations considered are four:

- basic multilayer structure
- basic multilayer structure with 5. cm water shielding,
- basic multilayer structure with 10. cm water shielding,
- basic multilayer structure with 10. cm polyethylene shielding.

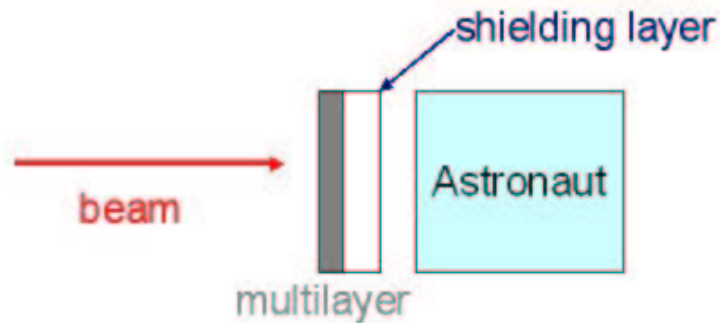


Figure 52: Experimental set-up for dosimetric studies with primary GCR beams.

Fig. 53 shows clearly the initial energy shift of primary particles absorbed in the Astronaut, due to the presence of shielding; primary protons with an initial energy lower than 40. MeV are stopped by the basic multilayer structure while primary protons with an initial energy lower than about 90. MeV are stopped by the basic multilayer structure with 5. cm water shielding.

Fig. 54, 55, 56, 57, 58 illustrate the results concerning GCR alpha particles, C-12, O-16, Si-28, Fe-52 ions generated in the experimental set-up shown in fig. 52.

Table 6 and table 7 collect the results of the simulations concerning Galactic Cosmic Rays shot against the experimental set-up (see fig. 52), where a similar effect of shielding structure as described above can be observed.

8.5 Energy deposit in the Astronaut

The energy deposit of the Galactic Cosmic Rays in the Astronaut has been calculated in the Astronaut placed behind the basic multilayer structure and different shielding solu-

Table 6: GCR particles shielded respectively by the basic multilayer structure and the the basic multilayer structure with 5. cm water shielding. E is the initial energy of primary GCR particles.

	no shielding	5. cm water shielding
GCR p	$E < \sim 40MeV$	$E < \sim 90MeV$
GCR alpha	$E < \sim 160MeV$	$E < \sim 350MeV$
GCR C12 ions	$E < \sim 1GeV$	$E < \sim 2.5GeV$
GCR O16 ions	$E < \sim 2GeV$	$E < \sim 3GeV$
GCR Si28 ions	$E < \sim 3GeV$	$E < \sim 10GeV$
GCR Fe52 ions	$E < \sim 10GeV$	$E < \sim 20GeV$

Table 7: GCR particles traversing respectively the basic multilayer structure and the basic multilayer structure with 5 cm water shielding. E is the initial energy of primary GCR particles.

	no shielding	5. cm water shielding
GCR p	$E > \sim 220MeV$	$E > \sim 250MeV$
GCR alpha	$E > \sim 900MeV$	$E > \sim 1GeV$
GCR C12 ions	$E > \sim 5GeV$	$E > \sim 6GeV$
GCR O16 ions	$E > \sim 8GeV$	$E > \sim 9GeV$
GCR Si28 ions	$E > \sim 20GeV$	$E > \sim 22GeV$

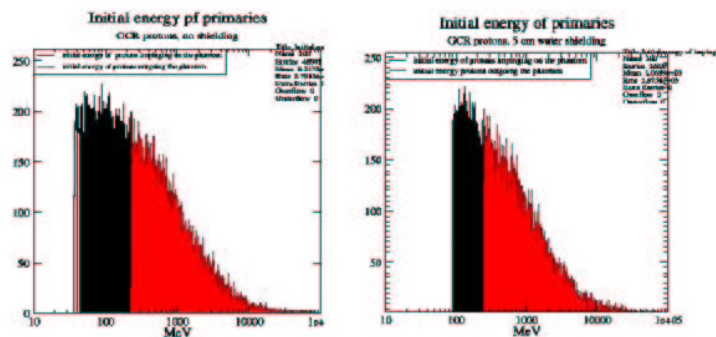


Figure 53: A GCR proton beam hits the basic multilayer structure in the first plot, the basic multilayer structure with 5. cm water shielding in the second plot. The initial energy of primaries impinging on the phantom is in black; the initial energy of primaries traversing the phantom is in red.

tions. Fig. 59, 60, 61, 62, 63, 64 show the results obtained with GCR protons, alpha particles, C-12 ions, O-16 ions, Si-28 ions, Fe-52 ions as primary particles impinging on the basic multilayer structure with 10. cm water layer.

Fig. 62, 63, 64 show clearly that the energy deposit calculation is based on too low statistics in the case of primary GCR ions; the energy deposit is given by few events and, as a consequence, it is necessary to study the effects of GCR high energy particles in order to achieve statistically significant results.

8.6 Optimisation of the production strategy

If we look at the energy spectra of the Galactic Cosmic Rays, we notice that the probability to generate high energy particles (for example with a primary energy $E > 10\text{GeV}$) is very low with respect to lower energies. As a consequence, the dosimetric studies would be affected by low statistics of the contribution of higher energy primary particles.

Since the generation of a large enough number of events to obtain a statistical significance also from the high energy end of the primary spectrum is prohibitive in terms of computing resources needed, an appropriate strategy has been devised to evaluate the dosimetric contribution of the low energy component of the GCR spectrum. For this purpose the simulation production for GCR spectra has been split into two distinct sets of runs; one involves all the original GCR energy spectra, while the second concerns the GCR energy spectra imposing $E > E_{limit}$. Both sets of runs consist of the same number of events generated, thus obtaining a statistically significant sample also for high energy GCR com-

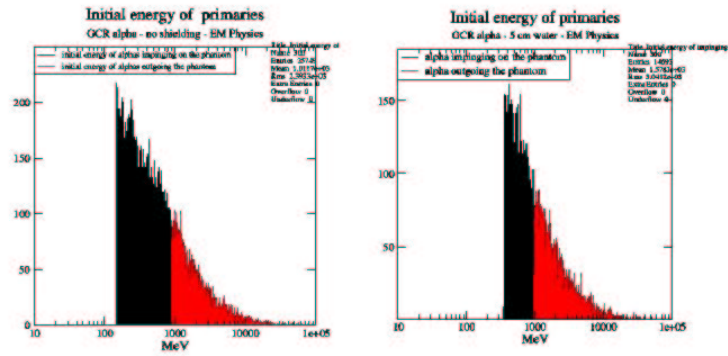


Figure 54: A GCR alpha particle beam hits the basic multilayer structure in the first plot, the basic multilayer structure with 5. cm water shielding in the second plot. The initial energy of primaries impinging on the phantom is in black; the initial energy of primaries traversing the phantom is in red.

ponents; for the final dosimetric evaluation the relative contributions should be properly scaled.

8.7 Dose calculation

The dose represents a measurement of the effect of the passage of radiation in a medium. The dose is defined as the energy of radiation absorbed per mass unit of the medium:

$$Dose(Gray) = \frac{dE}{dm} \left(\frac{J}{kg} \right).$$

The biological effect is not taken into account in the dosimetric study, object of the Geant4 REMSIM application.

The dose in the phantom is calculated starting from the energy deposit collected in each voxel ($voxelVolume = 0.01 \times 5. \times 5.m^3$) of the Astronaut in the following way:

$$dose = \frac{energyDep}{voxelVolume \times d}$$

where d is the density of water expressed in $\frac{kg}{m^3}$.

The dose is calculated separately for GCR particles (protons, alpha particles, C-12, O-16, Si-28, Fe-52 ions); then the partial results are weighted as described in section 6.

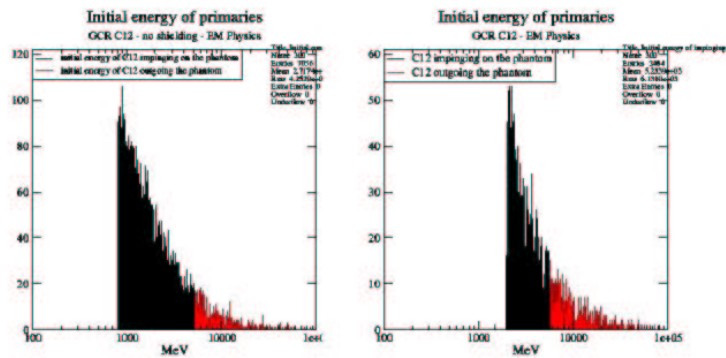


Figure 55: A GCR C-12 ion beam hits the basic multilayer structure in the first plot, the basic multilayer structure with 5. cm water shielding in the second plot. The initial energy of primaries impinging on the phantom is in black; the initial energy of primaries traversing the phantom is in red.

8.7.1 Dose in presence of the basic multilayer structure

The energy deposit (fig. 65) and the corresponding dose (fig. 66) versus the depth in the Astronaut have been calculated with GCR particles as primaries with a geometrical set-up consisting of the basic multilayer structure only.

Fig. 65 demonstrates clearly that the energy deposit given by GCR Fe-52 ions is affected by low statistics; this result stresses the need of an appropriate strategy to evaluate the contribution to the dose of the high energy component of the GCR spectra.

8.7.2 Dose with 5. cm water shielding

The results shown in fig. 67 and 68 are obtained with GCR particles impinging on the basic multilayer structure with 5. cm water shielding.

Fig. 67 and fig. 68 show the energy deposit and the dose in the Astronaut resulting from the Galactic Cosmic Rays particle.

8.7.3 Dose with 10. cm water shielding

Fig. 69 and 70 illustrate the energy deposit and the dose versus the depth in the Astronaut resulting from GCR particles in the presence of the basic multilayer structure with 10 cm water shielding.

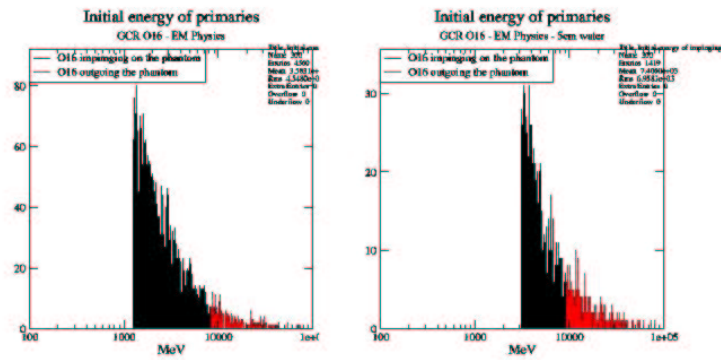


Figure 56: A GCR O-16 ion beam hits the basic multilayer structure in the first plot, the basic multilayer structure with 5. cm water shielding in the second plot. The initial energy of primaries impinging on the phantom is in black; the initial energy of primaries traversing the phantom is in red.

8.8 Comparison of different thicknesses of water shielding

Fig. 71, fig. 72, fig. 73, fig. 74, fig. 75 show the energy deposit in the Astronaut for all the Galactic Cosmic Rays components in the three different shielding configuration considered in the previous sections (0., 5. cm, 10. cm water).

As it is shown, the effect of thicker water shielding layers is to reduce the energy deposit in the Astronaut. This can be easily justified as a consequence of the energy shift effect produced by the shielding as described in subsection 8.3.1, considering that the GCR fluxes exhibit a decreasing behaviour as a function of particle energy.

The dose calculation regarding GCR Fe-52 ions has a too low statistics to infer any significant evaluation of the results obtained.

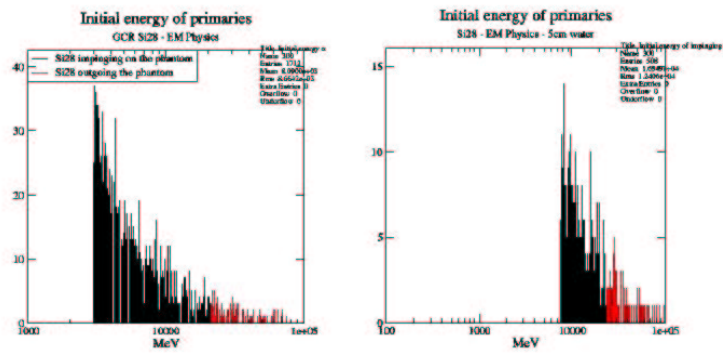


Figure 57: A GCR Si-28 ion beam hits the basic multilayer in the first plot, on the basic multilayer structure with 5 cm water shielding in the second plot. The initial energy of primaries impinging on the phantom is in black; the initial energy of primaries traversing the phantom is in red.

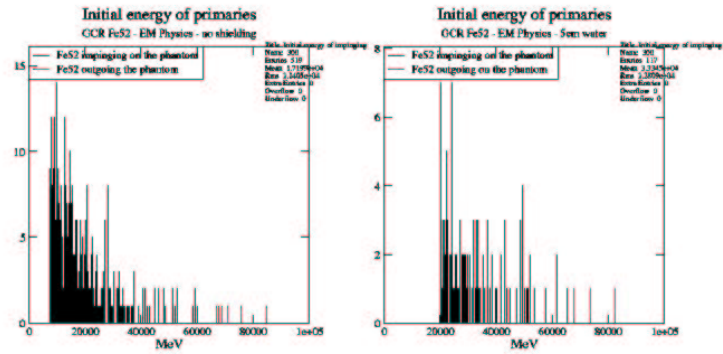


Figure 58: A GCR Fe-52 ion beam hits on the basic multilayer structure in the first plot, the basic multilayer structure + 5 cm water shielding in the second plot. The initial energy of primaries impinging on the phantom is in black; the initial energy of primaries traversing the phantom is in red.

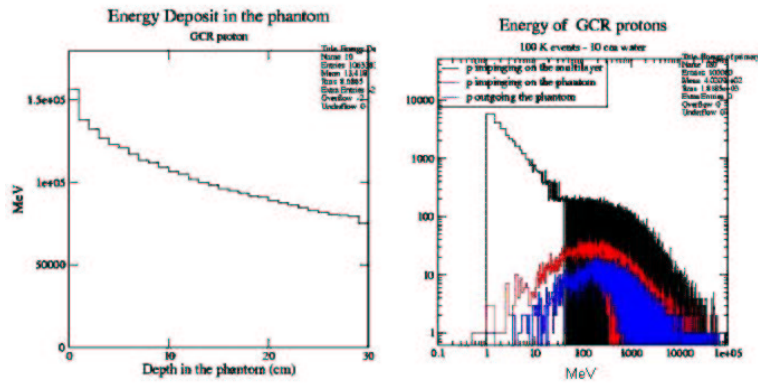


Figure 59: The first plot shows the energy deposit in the Astronaut versus the depth along Z axis. The second plot shows the initial energy of primary protons (in black), the energy of protons reaching the Astronaut (in red) and the energy of protons outgoing the phantom (in blue).

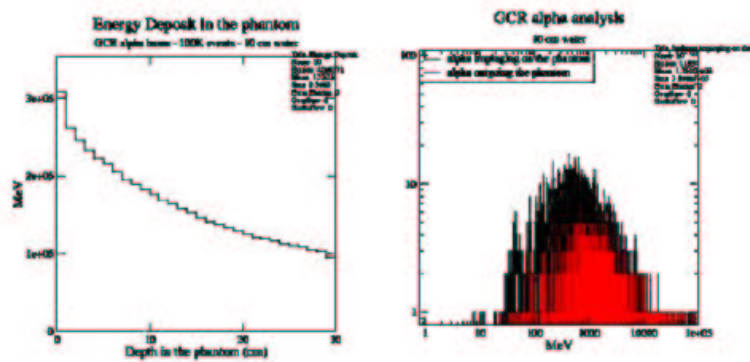


Figure 60: The first plot shows the energy deposit in the Astronaut versus the depth along Z axis. The second plot shows the energy of alpha particles reaching the Astronaut (in black), the energy of alpha particles outgoing the phantom (in red).

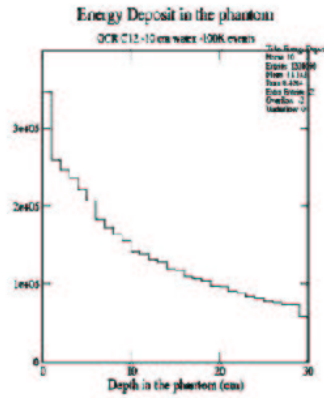


Figure 61: Energy deposit in the Astronaut in respect to the depth along Z axis produced by GCR C-12 ions.

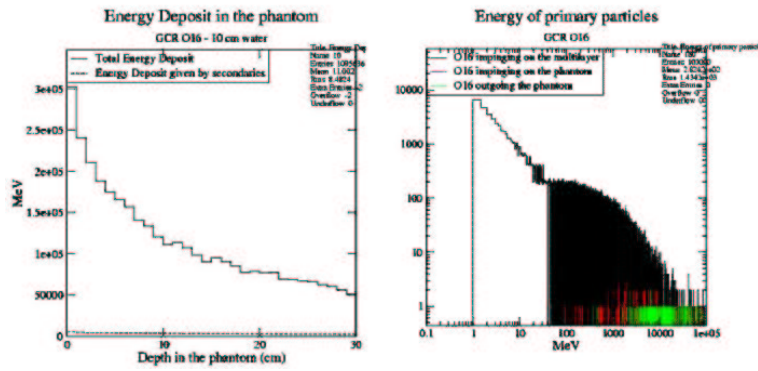


Figure 62: The first plot shows the energy deposit in the Astronaut versus the depth along Z axis. The second plot shows the initial energy of the GCR O-16 ions (in black), the energy of O-16 ions reaching the Astronaut (in red), the energy of O-16 ions outgoing the Astronaut (in green).

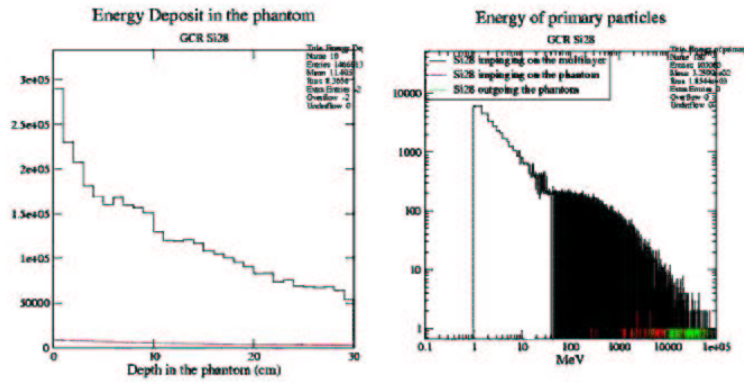


Figure 63: The first plot shows the energy deposit in the Astronaut versus the depth along Z axis. The second plot shows the initial energy of the GCR Si-28 ions (in black), the energy of Si-28 ions reaching the Astronaut (in red), the energy of Si-28 ions outgoing the Astronaut (in green).

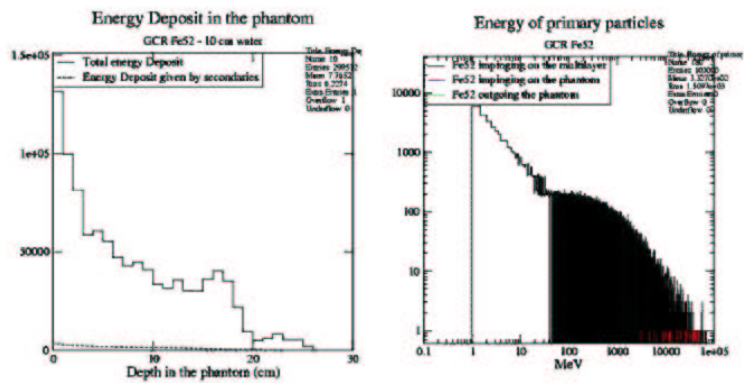


Figure 64: The first plot shows the energy deposit in the Astronaut in respect to the depth along Z axis. The second plot shows the initial energy of the GCR Fe-52 ions (in black), the energy of Fe-52 ions reaching on the Astronaut.

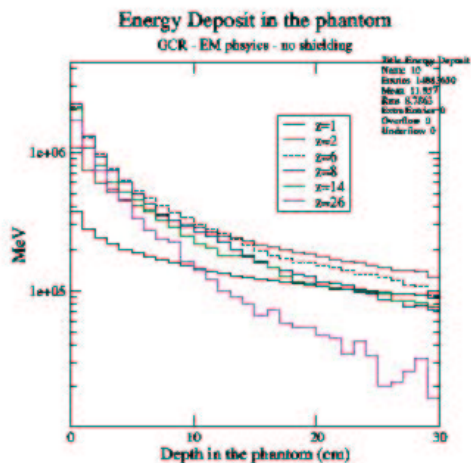


Figure 65: Energy deposit in the Astronaut resulting from GCR protons, alpha particles, C-12, O-16, Si-28, and Fe-52 ions in the presence of the basic multilayer structure.

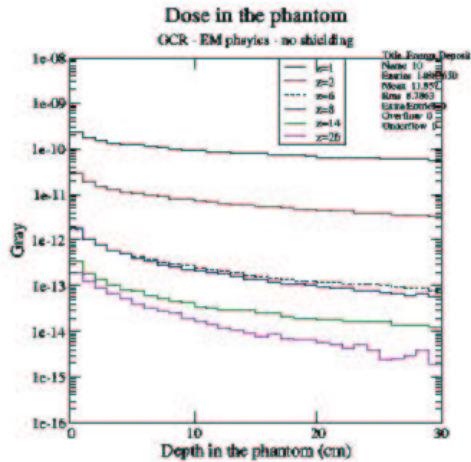


Figure 66: Dose in the Astronaut resulting from GCR particles in the presence of the basic multilayer structure.

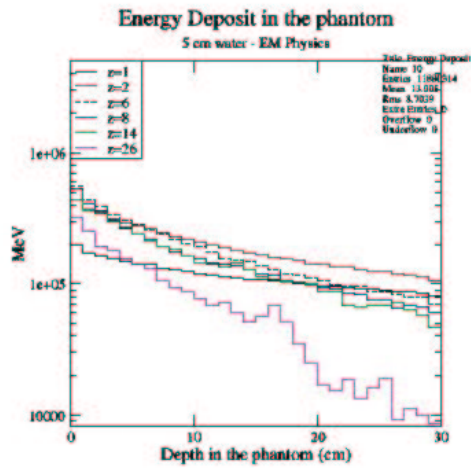


Figure 67: Energy deposit in the Astronaut resulting from GCR particles in the presence of the basic multilayer structure with 5 cm water shielding.

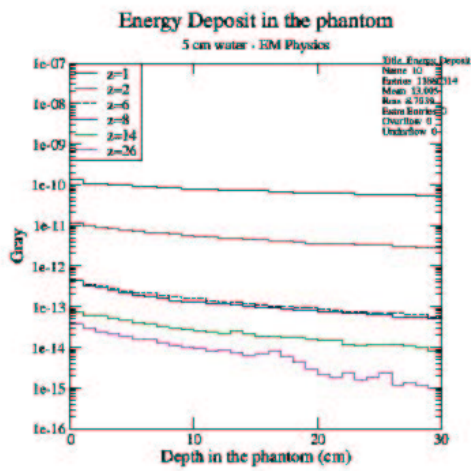


Figure 68: Dose in the Astronaut resulting from GCR particles in the presence of the basic multilayer structure with 5 cm water shielding.

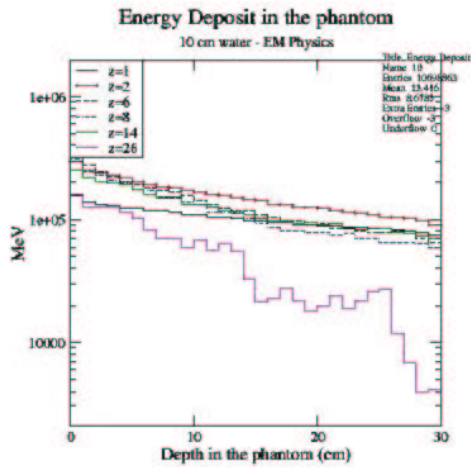


Figure 69: Energy deposit in the Astronaut resulting from GCR particles in the presence of the basic multilayer structure with 10 cm water shielding.

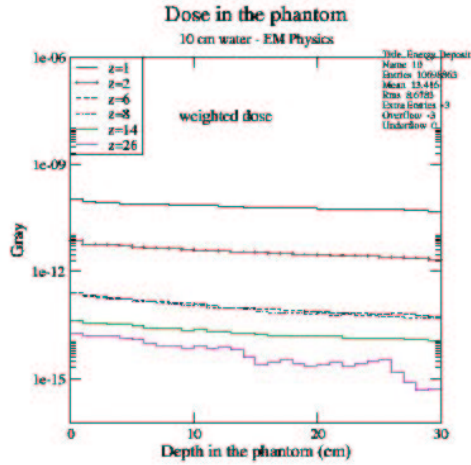


Figure 70: Dose in the Astronaut resulting from GCR particles in the presence of the basic multilayer structure with 10 cm water shielding.

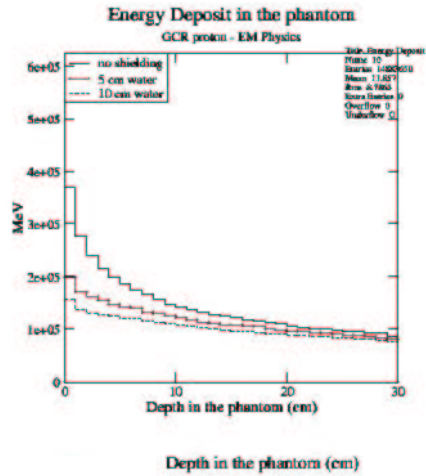


Figure 71: Energy deposit in the Astronaut resulting from GCR protons in the presence of three different configurations: basic multilayer structure with 0., 5. cm, 10. cm water shielding.

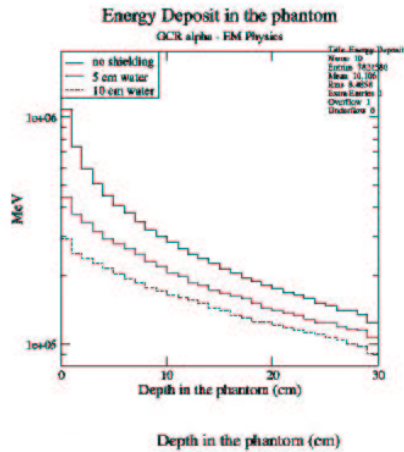


Figure 72: Energy deposit in the Astronaut resulting from GCR alpha particles in the presence of three different configurations: basic multilayer structure with 0., 5. cm, 10. cm water shielding.

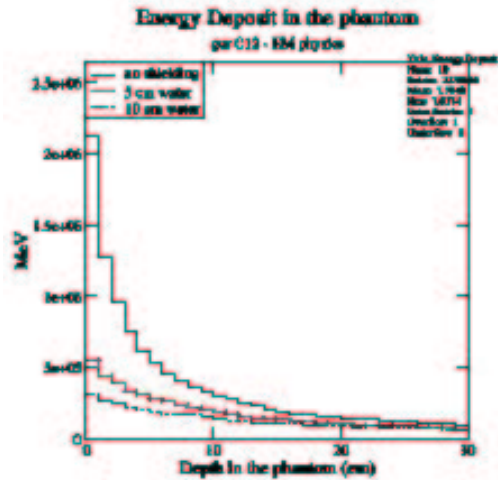


Figure 73: Energy deposit in the Astronaut resulting from GCR C-12 ions in the presence of three different configurations: basic multilayer structure with 0., 5. cm, 10. cm water shielding.

8.9 Dose with 10. cm polyethylene shielding

Fig. 76 and 77 show the energy deposit and the relative dose versus the depth in the Astronaut in the presence of the basic multilayer structure with 10. cm polyethylene shielding.

8.10 Comparison of 10. cm water and polyethylene shielding

Fig. 80, fig. 81, fig. 82, fig. 83, fig. 84, fig. 85 show the energy deposit in the Astronaut for all the Galactic Cosmic Rays components in the different shielding set-ups: basic multilayer structure with 10. cm water or polyethylene shielding; the energy deposit in the Astronaut is similar for GCR protons, alpha particles, C-12 ions in the two cases.

This result can be justified by the similar proton and alpha Stopping Power in water and polyethylene (fig. 78 and fig. 79) in the energy range of interest.

Further investigation is needed for the results obtained with GCR O-16, Si-28 and Fe-52 ions as primary particles because of the low statistics of the simulation results.

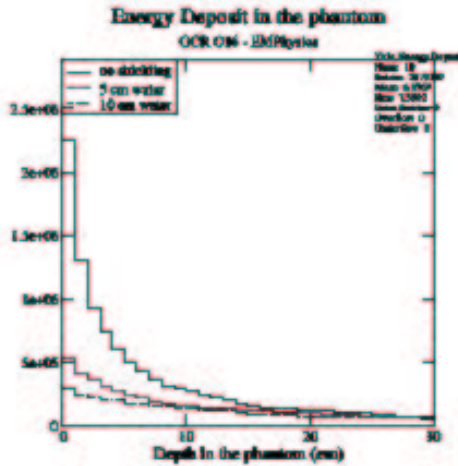


Figure 74: Energy deposit in the Astronaut resulting from GCR O-16 ions in the presence of three different configurations: basic multilayer structure with 0., 5. cm, 10. cm water shielding.

8.11 Dose resulting from high energy GCR particles

As mentioned above, the dose calculation is affected by low statistics in the region of high energy Galactic Cosmic Rays. This problem is caused by the very low probability of generating a high energy GCR particle, given the flux distribution of GCR as a function of energy. For example, the probability of generating a Fe-52 ion with energy $E \sim 20\text{GeV}$ is 1/100 of generating a Fe-52 ions with $E \sim 1\text{MeV}$. In addition to that, heavy ions (differently from protons and alpha particles) penetrate in the Astronaut, without being stopped by the material in front of it, if their initial energy is higher than few GeV.

Therefore, the dose in the Astronaut has been calculated in the same experimental set-up conditions of the cases shown above, limiting the production to the higher energy component of the GCR spectrum above 10 GeV.

8.11.1 Dose contribution from high energy GCR with 5. cm water shielding

Fig. 86, 87, 88 show that all the GCR protons, alpha particles and C-12 ions generated with $E > 10\text{GeV}$ traverse the Astronaut, behaving as minimum ionising particles.

The behaviour of GCR O-16 ions is very similar to GCR C-12 ions as primary particles because of the similar charge and flux.

Fig. 89, 90 show that Si-28 ions with initial energy $10\text{GeV} < E < 22\text{GeV}$ and Fe-52

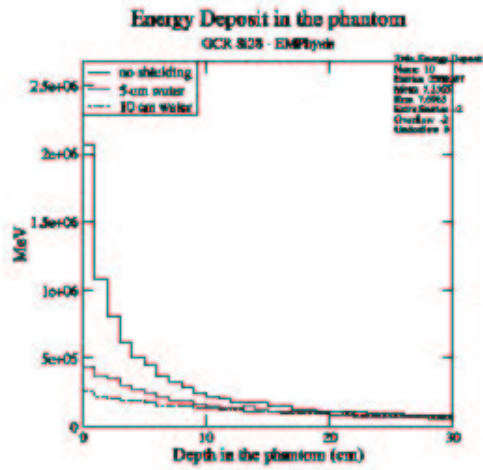


Figure 75: Energy deposit in the Astronaut resulting from GCR Si-28 ions in the presence of three different configurations: basic multilayer structure with 0., 5. cm, 10. cm water shielding.

ions with initial energy $20\text{GeV} < E < 70\text{GeV}$ are completely absorbed in the Astronaut.

Fig. 91 and 92 show the energy deposit in the Astronaut and the relative calculated dose, weighted with the factors shown above.

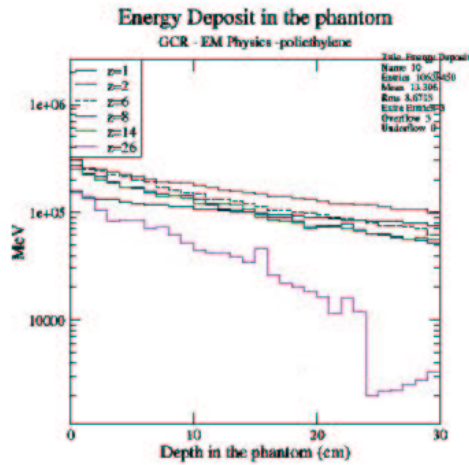


Figure 76: Energy deposit in the Astronaut resulting from GCR particles in the presence the basic multilayer structure with 10. cm polyethylene shielding.

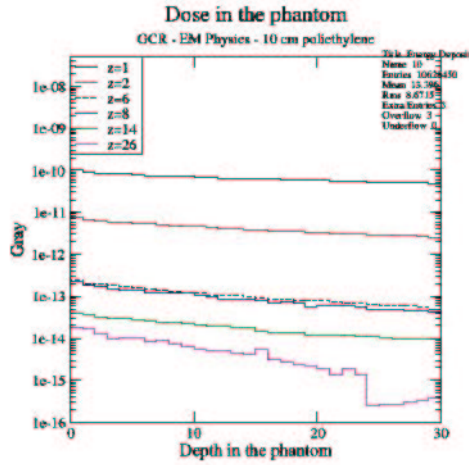


Figure 77: Dose in the Astronaut resulting from GCR particles in the presence the basic multilayer structure with 10. cm polyethylene shielding.

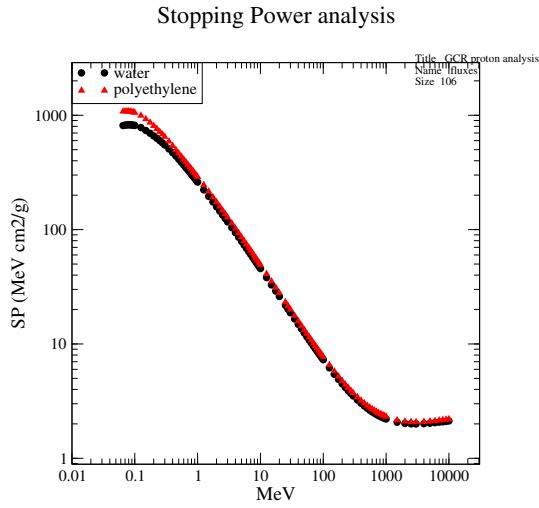


Figure 78: Proton Stopping Power in water and in polyethylene (ICRU Report 49 [23]).

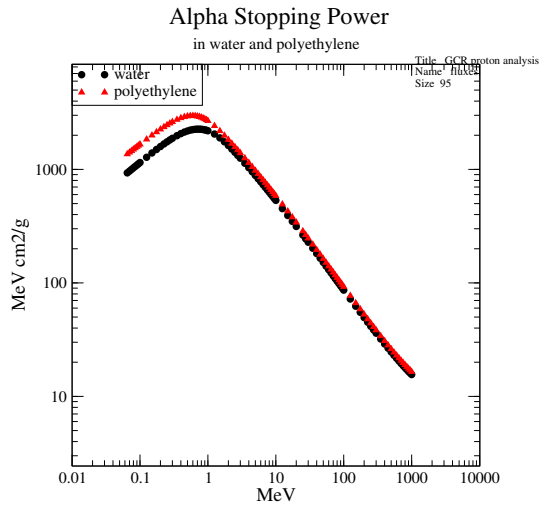


Figure 79: Alpha Stopping Power in water and in polyethylene (ICRU Report 49 [23]).

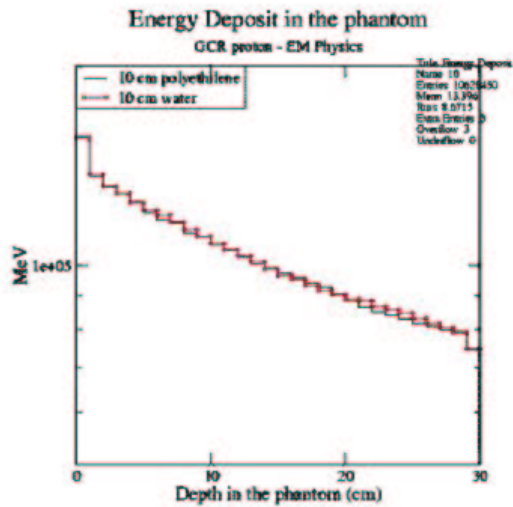


Figure 80: Energy deposit in the Astronaut resulting from GCR protons with 10. cm water and polyethylene shielding.

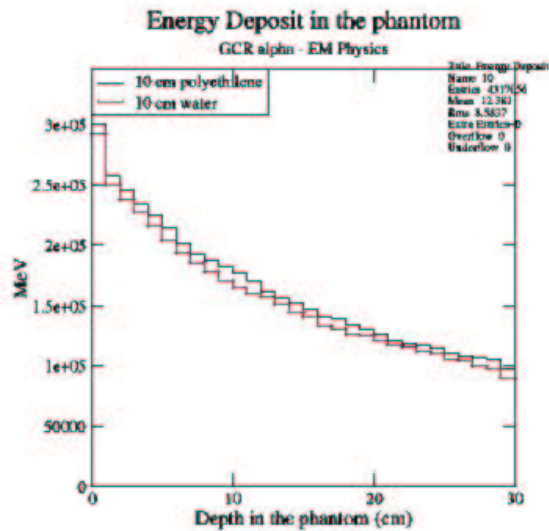


Figure 81: Energy deposit in the Astronaut resulting from GCR alpha particles with 10. cm water and polyethylene shielding.

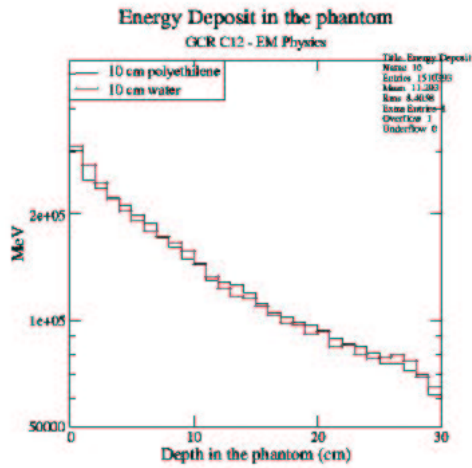


Figure 82: Energy deposit in the Astronaut resulting from GCR C-12 ions with 10. cm water and polyethylene shielding.

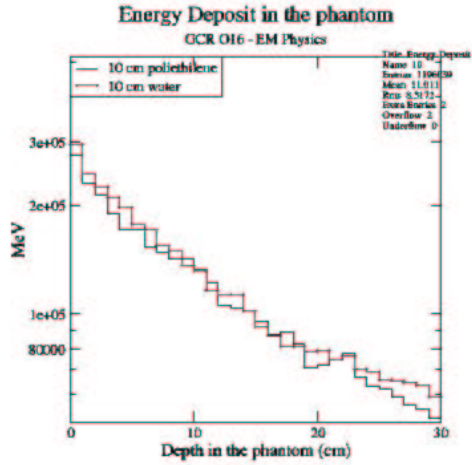


Figure 83: Energy deposit in the Astronaut resulting from GCR O-16 ions with 10. cm water and polyethylene shielding.

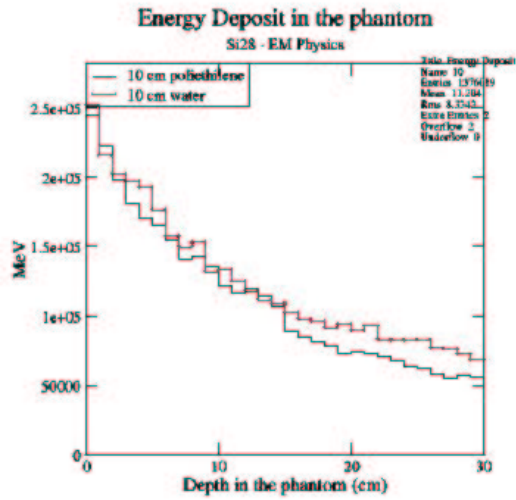


Figure 84: Energy deposit given by GCR Si-28 ions in the Astronaut with the 10. cm water and 10. cm polyethylene shields.

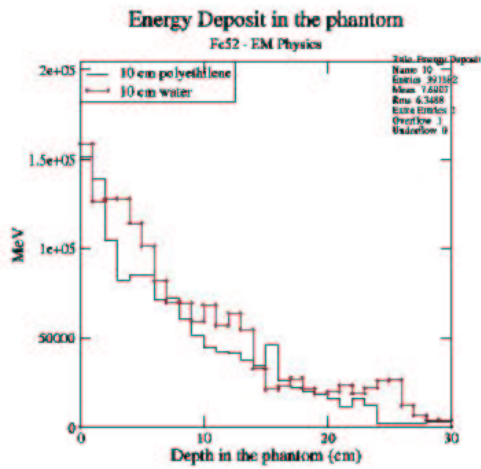


Figure 85: Energy deposit given by GCR Fe-52 ions in the Astronaut with the 10. cm water and 10. cm polyethylene shields.

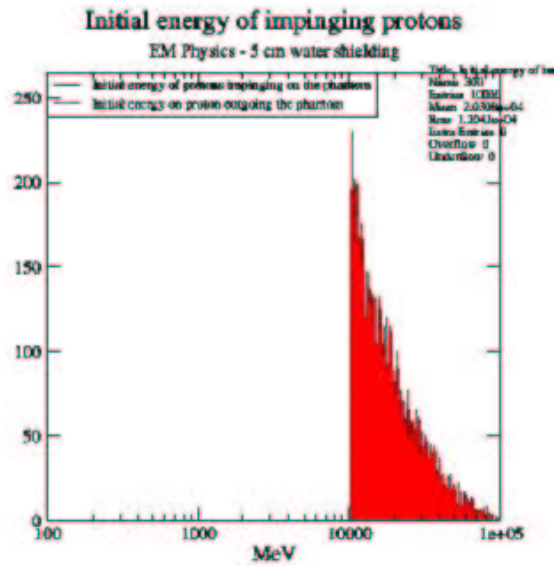


Figure 86: 5. cm water shielding: the histogram of the initial high energy GCR protons reaching the Astronaut is in black; the histogram of the initial high energy GCR protons outgoing the phantom is in red.

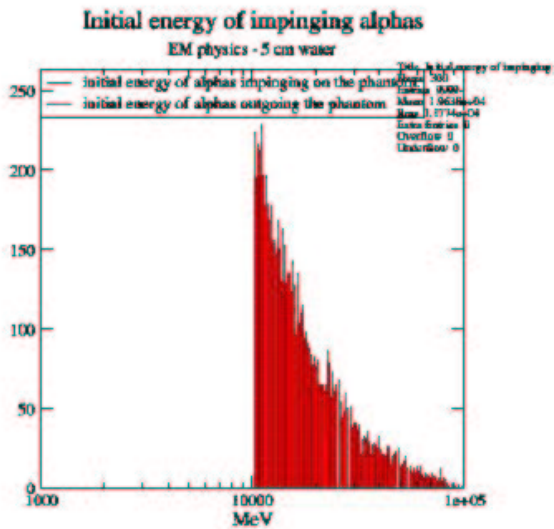


Figure 87: 5. cm water shielding: the histogram of the initial high energy GCR alpha particles reaching the Astronaut is in black; the histogram of the initial high energy GCR alpha particles outgoing the phantom is in red.

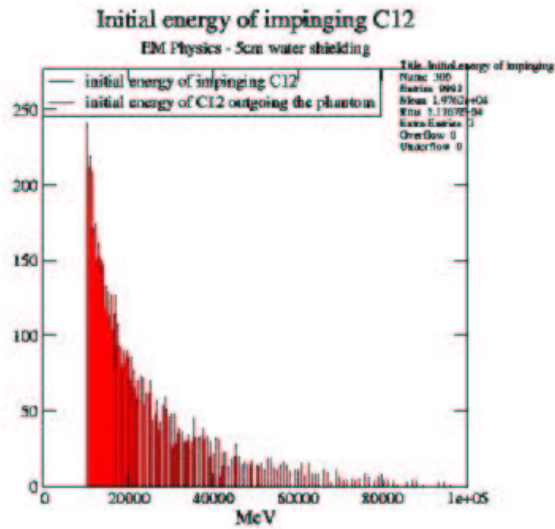


Figure 88: 5. cm water shielding: the histogram of the initial high energy GCR C-12 ions reaching the Astronaut is in black; the histogram of the initial high energy GCR C-12 ions outgoing the phantom is in red.

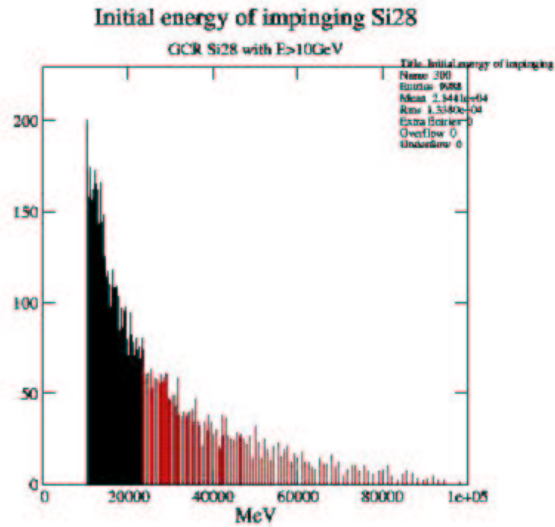


Figure 89: 5. cm water shielding: the histogram of the initial high energy GCR Si-28 ions reaching the Astronaut is in black; the histogram of the initial high energy GCR Si-28 particles outgoing the phantom is in red.

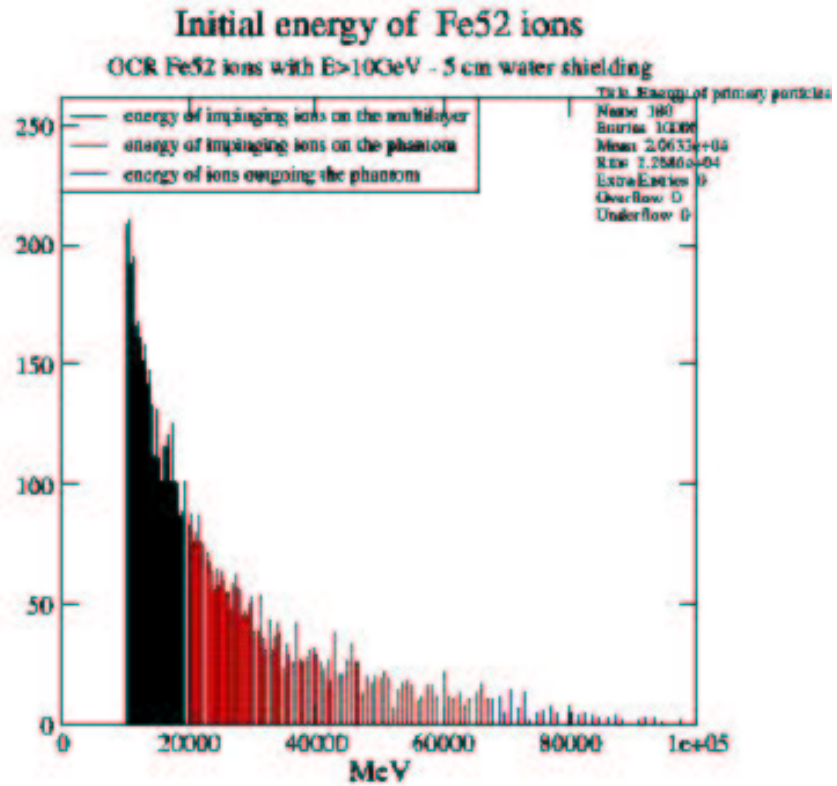


Figure 90: 5. cm water shielding: the histogram of the initial high energy Fe-52 ions is in black; the histogram of the initial high energy GCR Fe-52 ions reaching the Astronaut is in red; the histogram of the initial energy GCR Fe-52 ions outgoing the phantom is in blue.

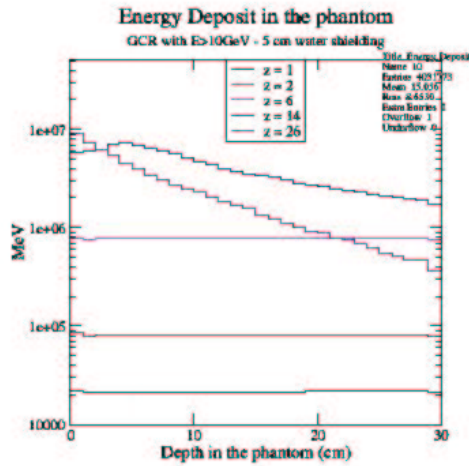


Figure 91: 5. cm water shield case: energy deposit in the Astronaut given by the GCR particle components, generated with initial energy $E > 10\text{GeV}$.

8.11.2 Dose contribution from high energy GCR with 10. cm water shielding

Fig. 93, 94, 95 show that all the GCR protons, alpha particles and C-12 ions generated with $E > 10\text{GeV}$ traverse the Astronaut, behaving as minimum ionising particles. The behaviour of GCR O-16 ions is very similar to GCR C-12 ions as primary particles.

Fig. 96, 97 show that Si-28 ions with initial energy $11\text{GeV} < E < 25\text{GeV}$ and Fe-52 ions with initial energy $30\text{GeV} < E < 75\text{GeV}$ are completely absorbed in the Astronaut. Fig. 98 and 99 show the energy deposit and the corresponding dose in the Astronaut.

8.11.3 Comparison of 5. cm and 10. cm water shielding

From the comparison of the results of energy deposits deriving from the higher energy component of the GCR spectra, one can infer:

- the energy deposit in the Astronaut resulting from GCR protons, alpha particles and C-12 ions is the same in the case of 5. and 10. cm water shielding; this is a consequence of the fact that these GCR components behave as minimum ionising particles.
- The energy deposit in the Astronaut resulting from Si-28 and Fe-52 ions is lower with 10. cm water shielding.

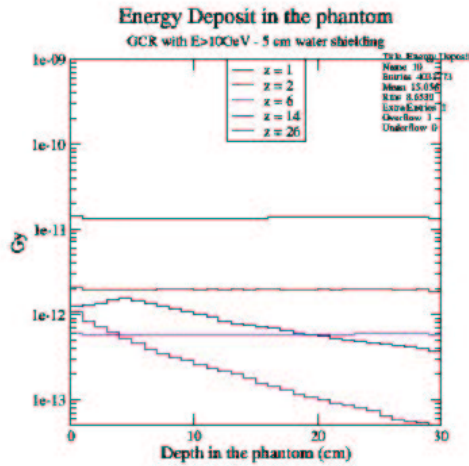


Figure 92: 5. cm water shield case: dose in the Astronaut given by the GCR particle components, generated with initial energy $E > 10 \text{ GeV}$.

Fig. 100 shows the energy deposit in the Astronaut resulting from GCR Fe-52 ions in the presence of 5. cm and 10 cm water shielding.

8.11.4 Dose contribution from high energy GCR with 10. cm polyethylene

Fig. 101, 102, 103 show that all the GCR protons, alpha particles and C-12 ions generated with $E > 10 \text{ GeV}$ traverse the Astronaut behaving as minimum ionising particles. The behaviour of GCR O-16 ions is very similar to GCR C-12 ions.

Fig. 104, 105 show that Si-28 ions with initial energy $11 \text{ GeV} < E < 25 \text{ GeV}$ and Fe-52 ions with initial energy $30 \text{ GeV} < E < 75 \text{ GeV}$ are completely absorbed in the Astronaut.

Fig. 106 shows the energy deposit in the Astronaut in the two configuration of 10. cm of water and polyethylene shielding, due to the high energy GCR particles. The results are comparable in the two cases.

8.12 Conclusions

The dosimetric effect of Galactic Cosmic Rays has been studied in different shielding configurations:

- basic multilayer structure with no shielding,
- basic multilayer structure with 5. cm water shielding,

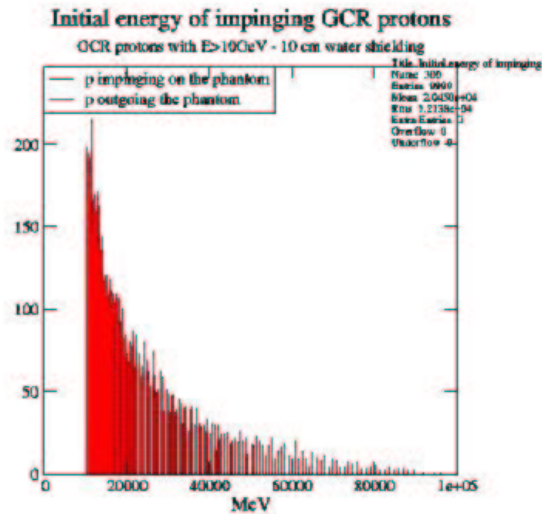


Figure 93: 10. cm water shielding: the histogram of the initial high energy GCR protons reaching the Astronaut is in black; the histogram of the initial high energy GCR protons outgoing the phantom is in red.

- basic multilayer structure with 10. cm water shielding,
- basic multilayer structure with 10. cm polyethylene shielding.

These cases have been analysed to study the effect of different thicknesses and materials of the shielding.

The dosimetric analysis has been performed generating Galactic Cosmic Rays according to their energy spectra; to enhance the statistics relevance of the effects due to the high energy component of the spectra, a special optimisation of the production strategy has been applied.

The analysis of the simulation results shows that thicker shielding layers limit the energy deposit in the Astronaut and that the choice of water or polyethylene as shielding material has no significant effect on the dosimetric calculations.

The accuracy of the calculations of the energy deposit in the Astronaut can be estimated to be of the order of a few percent for what concerns the precision of Geant4 electromagnetic models.

However the accuracy of the energy deposit also depends on the precision of the models of the Galactic Cosmic Rays.

Possible developments for the future could be:

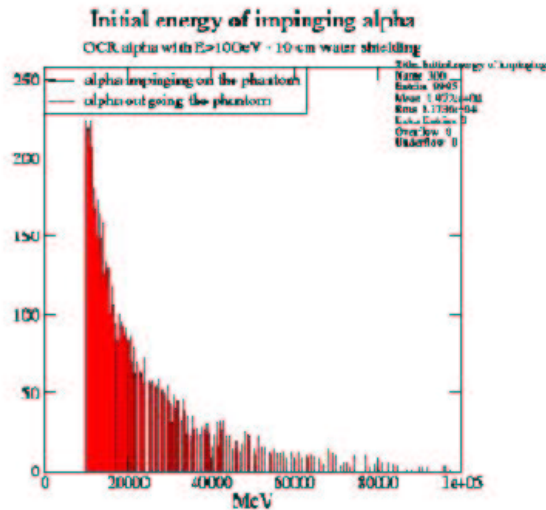


Figure 94: 10. cm water shielding: the histogram of the initial high energy GCR alpha particles reaching the Astronaut is in black; the histogram of the initial high energy GCR alpha particles outgoing the phantom is in red.

- the refinement of the dosimetric studies with angular dependencies of the incident GCR beam,
- the dosimetric analysis with other possible shielding materials and other possible thicknesses than the ones chosen in the context of the Geant4 REMSIM simulation.

9 Study of vehicle concepts: hadronic interactions

This section deals with the contributions of hadronic interactions to the dosimetric studies for vehicle concepts.

Geant4 provides an ample set of complementary and alternative models of hadronic physics. Because of its intrinsic complexity, this Geant4 domain is still the object of validation studies and of the further refinements of the models. Therefore the dosimetric studies involving hadronic interactions performed in the context of REMSIM should be considered as a preliminary indication of the hadronic contributions, rather than quantitative estimates.

The dosimetric studies described in the previous chapter have been repeated in the same geometrical and environment configurations, activating Geant4 hadronic processes too.

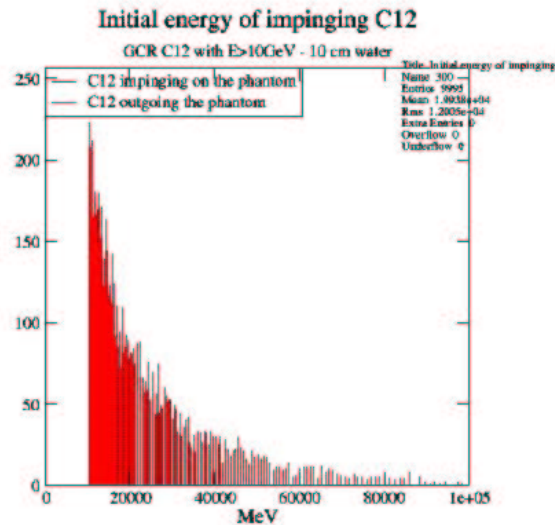


Figure 95: 10. cm water shielding: the histogram of the initial high energy GCR C-12 ions reaching the Astronaut is in black; the histogram of the initial high energy GCR C-12 ions outgoing the phantom is in red.

9.1 Geant4 hadronic models

Geant4 hadronic package offers a variety of models, based on different approaches: parameterised models, theory and data driven models.

Among the primary particles of interest for REMSIM, hadronic models are available in Geant4 for protons and alpha particles. At the present time Geant4 does not provide any models for the hadronic interactions of heavy ions yet.

The user is invested of the responsibility of selecting the hadronic models more appropriate for his own application among those available in Geant4.

9.2 Selection of hadronic models

The processes of elastic and inelastic scattering have been activated in REMSIM application for protons, neutrons and pions. To describe hadronic inelastic scattering across the whole energy range relevant to REMSIM, a set of complementary hadronic models has been selected:

- Quark Gluon String (QGS) Model for high energies ($15.GeV < E < 100.TeV$),
- Low Energy Parameterised (LEP) model ($2.8GeV < E < 25.GeV$),

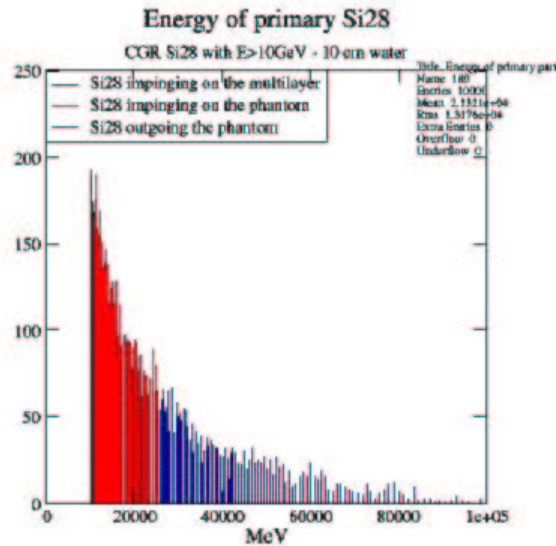


Figure 96: 10. cm water shielding: the histogram of the initial high energy GCR Si-28 ions reaching the Astronaut is in black; the histogram of the initial high energy GCR Si-28 ions outgoing the phantom is in red.

- Bertini Cascade ($0. < E < 3.2\text{GeV}$).

Hadronic elastic and inelastic scattering for alpha particles too; for inelastic scattering, the following models have been activated to cover the energy range of interest:

- Low Energy Parameterised (LEP) model ($0. < E < 100.\text{MeV}$),
- Binary Ion model ($80.\text{MeV} < E < 100.\text{GeV}$).

The choice of hadronic physics models for REMSIM application represents an educated guess, based on previous studies and preliminary validation activity performed by some Geant4 collaborators expert in this domain. The selection of models in the low energy range ($E < O(100\text{MeV})$) derives from the experience and experimental validation studies of the CATANA group at INFN-LNS [25]. The selection of models at higher energies derives from the experience and validation studies of the BaBar experiment at SLAC [26]. It is important to observe that, even if this model selection is based on the experience of usage in other experiments, the physics objectives and experimental configurations of both BaBar and CATANA differ from the scope of REMSIM. While this approach is adequate for a preliminary evaluation, further investigations and more in depth studies are

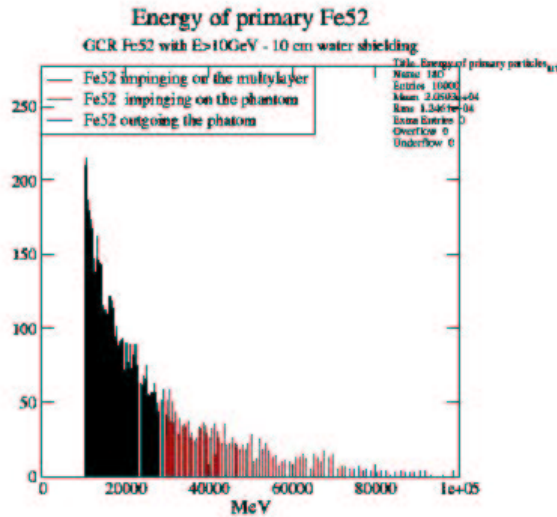


Figure 97: 10. cm water shielding: the histogram of the initial high energy GCR Fe-52 ions reaching the Astronaut is in black; the histogram of the initial high energy GCR Fe-52 ions outgoing the phantom is in red.

recommended to identify the selection of hadronic models most appropriate for shielding optimisation in interplanetary missions.

9.3 Verification of the proton Bragg peak

The validation of the Geant4 hadronic models is the object of extensive activity both within the Geant4 Collaboration and among experimental user groups. A thorough validation of the hadronic physics models relevant to REMSIM exceeds the scope of the present project.

However, because of its relevance in radioprotection studies, a verification of the accuracy of reproduction of the Bragg peak has been performed.

The experimental set-up, adopted for the verification of the proton Bragg peak in the context of the Geant4 REMSIM application, is shown in fig. 107. Fig. 108 shows the Bragg peaks in water deriving from 60., 80., 100. MeV proton beams. The results obtained are compatible with the experimental measurements of the CATANA group [25].

9.4 Model of the experimental set-up

The effect of the hadronic processes in the dose calculation in the Astronaut has been evaluated in the experimental set-up shown in fig. 109, corresponding to the basic ve-

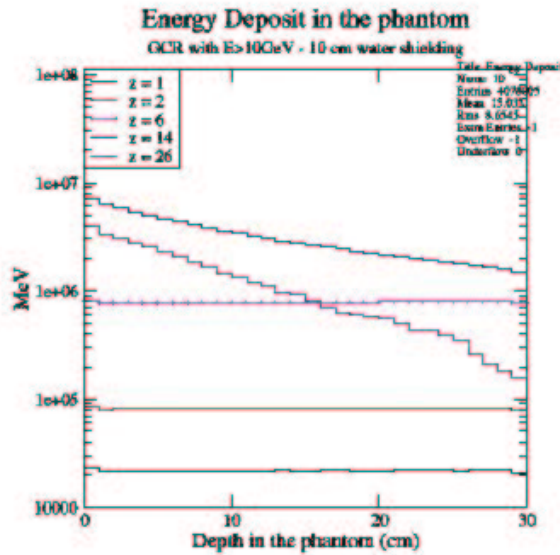


Figure 98: 10. cm water shielding; energy deposit in the Astronaut resulting from the GCR particle components, generated with initial energy $E > 10\text{GeV}$.

hicle structure with optional components representing the shielding. The configurations considered are:

- basic multilayer structure,
- basic multilayer structure with 5. cm water,
- basic multilayer structure with 10. cm water,
- basic multilayer structure with 10. cm polyethylene.

Both electromagnetic and hadronic processes are active. The primary particles are generated with direction parallel to Z axis. The result of the simulation is the energy deposit versus the depth in the Astronaut.

9.5 Strategy of the study

In a first phase monochromatic proton and alpha particle beams have been shot into the experimental set-up to gain a first quantitative evaluation of the effect of hadronic physics on the simulation results.

Then the energy deposit in the Astronaut resulting from GCR protons and alpha particles, generated in the same experimental set-up, has been calculated to study the dosimetric effect of different shielding solutions. This phase has been repeated generating high energy

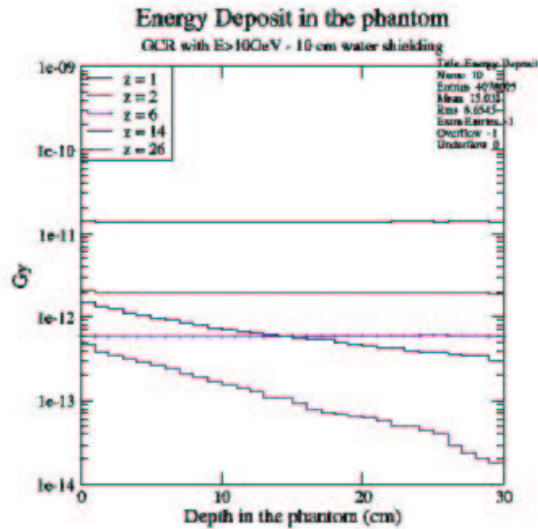


Figure 99: 10. cm water shielding; dose in the Astronaut resulting from the GCR particle components, generated with initial energy $E > 10 \text{ GeV}$,

($E > 10 \text{ GeV}$) GCR particles to obtain statistically significant results for the high energy component of the spectrum.

9.6 First iteration: study with monochromatic beams

The dosimetric study has been performed with monochromatic proton and alpha beams, hitting the basic multilayer structure.

Initial energies of the monochromatic proton beams of 100. MeV, 1 GeV, 10. GeV, 100. GeV, spanning the region of the GCR energy spectrum, have been selected for this preliminary study.

The results, illustrated in fig. 110, 111, 112, 113, show a significant effect in the calculation of energy deposit in the Astronaut due to hadronic processes, with respect to the case with electromagnetic interactions only. In particular, the effect is especially relevant for primary proton beams with initial energies above 1. GeV. This study has been repeated in the same experimental set-up for primary monochromatic alpha beams of 500 MeV, 1 GeV, 10 GeV, 100 GeV, spanning the region of the GCR energy spectrum.

Fig. 114 illustrates the energy deposit in the Astronaut resulting from a 500 MeV alpha beam; the effect observed is that secondaries, produced by hadronic interactions, deposit energy along the whole depth of the Astronaut.

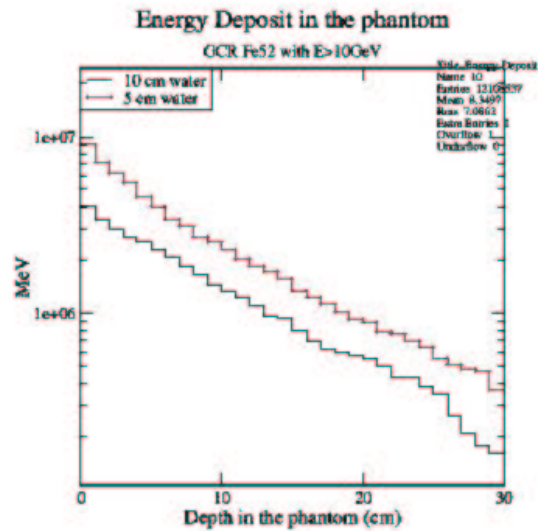


Figure 100: Energy deposit in the Astronaut resulting from high energy GCR Fe-52 ions in the configuration with 10. cm water shielding (in black), with 5. cm water shielding (in red).

Fig.115 and fig. 116 illustrate the energy deposit in the Astronaut resulting from 1 GeV and 10 GeV alpha beams respectively; also in these cases the hadronic processes have a relevant impact in the energy deposit calculation.

From this first iteration we can infer that the effect of hadronic processes in dose calculation in the Astronaut is significant and increasing with higher initial energy of primary particles beams. The same monochromatic proton and alpha particle beams have been shot against the basic multilayer structure with 5 and 10 cm water shielding.

Fig. 117 shows the energy deposit in the Astronaut resulting from monochromatic proton beams. From the results, we can infer that proton beams with an initial energy of 100. MeV are stopped by the basic multilayer structure with 10. cm water shielding, while they produce a Bragg peak in the Astronaut in the case of basic multilayer structure with 5. cm water shielding; this effect is consistent with what found in the previous study with the activation of the electromagnetic processes only. Primary 1. GeV and 10. GeV proton beams deposit the same energy in the Astronaut both in the configurations of 5. cm and 10. cm water shielding.

Fig. 118 illustrates that 100. GeV protons deposit more energy in the Astronaut in the configuration with 10. cm with respect to 5. cm water shielding. This effect results

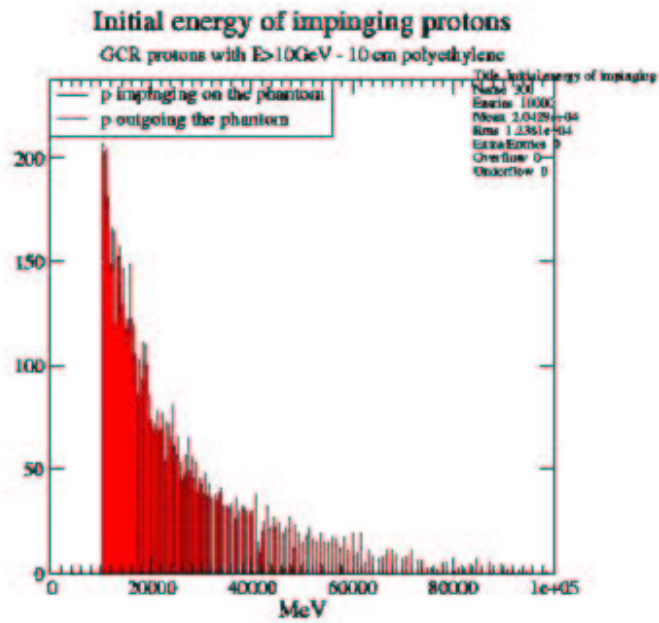


Figure 101: 10. cm polyethylene shielding: histogram of the initial energy of GCR protons (generated with $E > 10\text{GeV}$) impinging on the Astronaut (in black), histogram of the initial energy of GCR protons traversing the phantom (in red).

from differences in the generation of secondary particles, due to hadronic processes. The energy deposit in the Astronaut is the same in the two configurations activating Geant4 electromagnetic processes only.

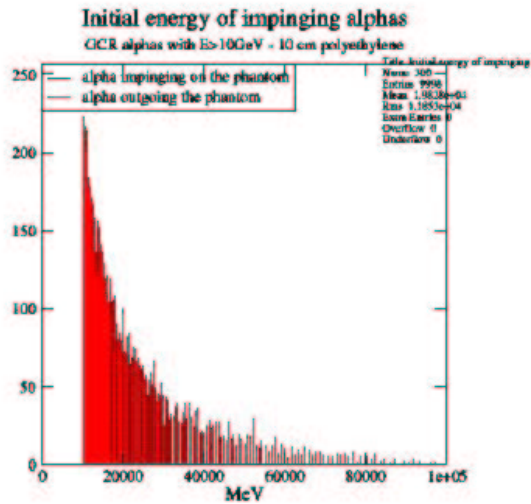


Figure 102: 10. cm polyethylene shielding: histogram of the initial energy of GCR alpha particles (generated with $E > 10\text{GeV}$) impinging on the Astronaut (in black), histogram of the initial energy of GCR alpha particles traversing the phantom (in red).

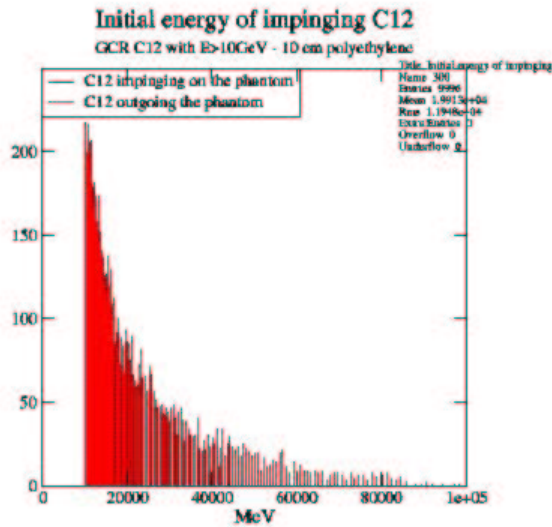


Figure 103: 10. cm polyethylene shielding: histogram of the initial energy of GCR C-12 ions (generated with $E > 10\text{GeV}$) impinging on the Astronaut (in black), histogram of the initial energy of GCR C-12 ions traversing the phantom (in red).

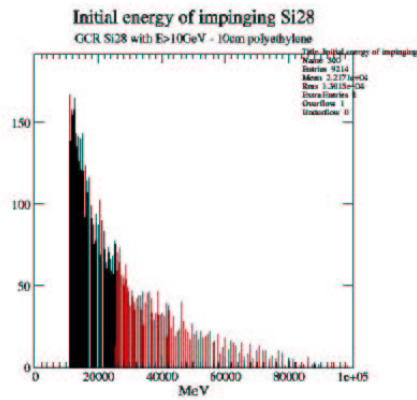


Figure 104: 10. cm polyethylene shielding: histogram reporting the primary energy spectrum (in black), histogram of the initial high energy of GCR Si-28 ions reaching the Astronaut (in red), histogram of the initial high energy of GCR Si-28 ions outgoing the phantom (in blue).

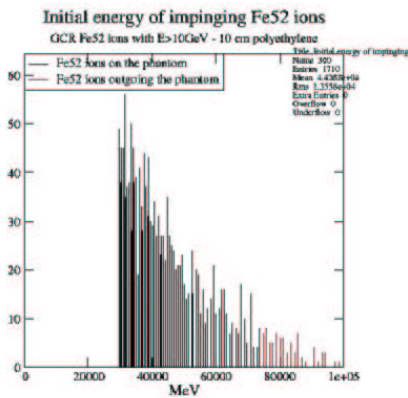


Figure 105: 10. cm polyethylene shielding: histogram reporting the primary energy spectrum (in black), histogram of the initial high energy of GCR Fe-52 ions reaching the Astronaut (in red), histogram of the initial high energy of GCR Fe-52 ions outgoing the phantom (in blue).

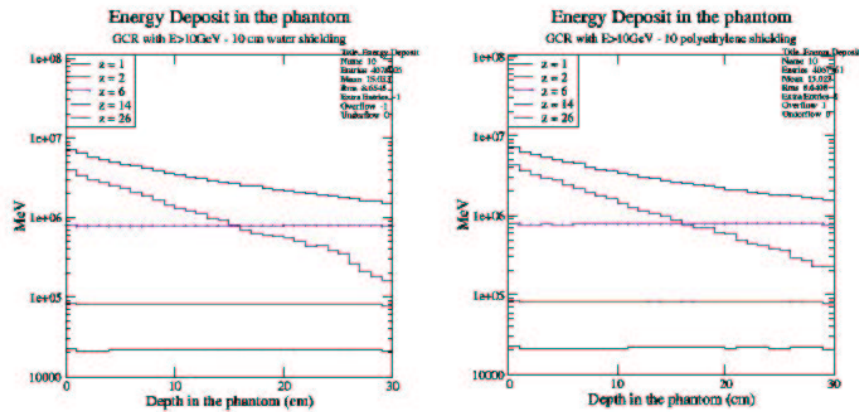


Figure 106: First plot: energy deposit in the Astronaut in the configuration with 10. cm water shielding; second plot: energy deposit in the Astronaut in the configuration with 10. cm polyethylene; both plots concern the high energy GCR particles.

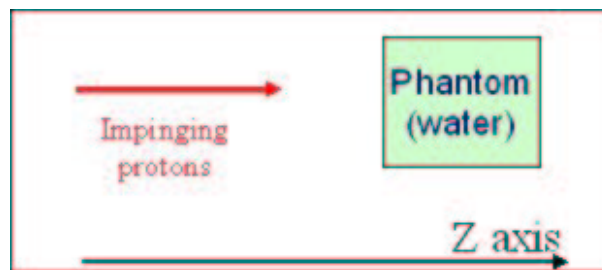


Figure 107: Experimental set-up adopted for the verification of the proton Bragg peak: a monochromatic proton beam, with initial direction parallel to the Z axis, impinges on a water phantom. The energy deposit is collected in the phantom as a function of the depth along the Z axis.

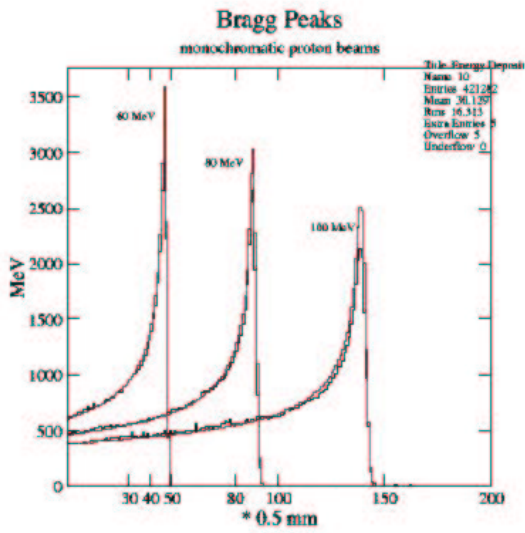


Figure 108: Bragg peaks in water deriving from 60., 80., 100. MeV proton beams.

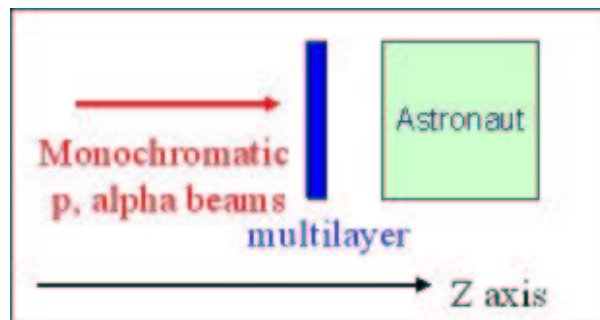


Figure 109: Experimental set-up consisting of basic multilayer structure with shielding.

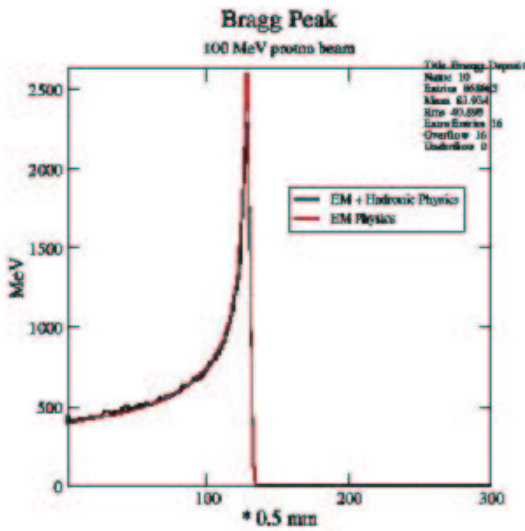


Figure 110: 100 MeV proton beam; comparison of energy deposit in the Astronaut activating Geant4 electromagnetic physics only (in red) and both electromagnetic and hadronic physics (in black).

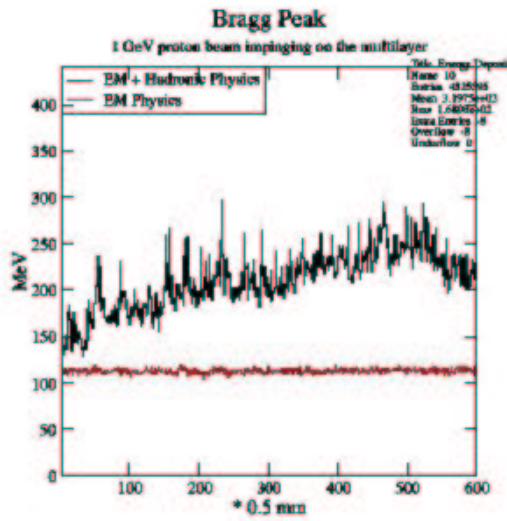


Figure 111: 1 GeV proton beam; comparison of energy deposit in the Astronaut activating Geant4 electromagnetic physics only (in red) and both electromagnetic and hadronic physics (in black).

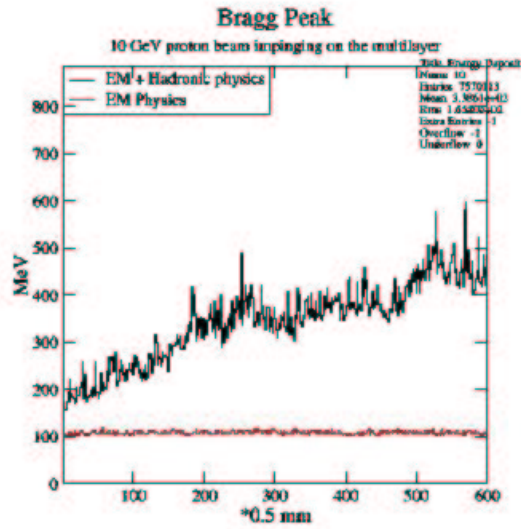


Figure 112: 10 GeV proton beam; comparison of energy deposit in the Astronaut activating electromagnetic Geant4 physics only (in red) and both electromagnetic and hadronic physics (in black).

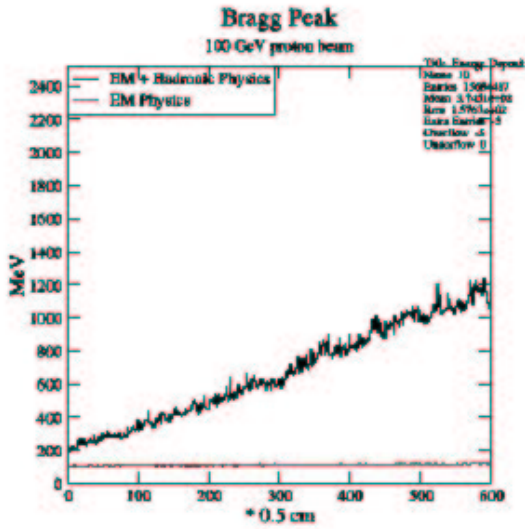


Figure 113: 100 GeV proton beam; comparison of energy deposit in the Astronaut activating Geant4 electromagnetic physics only (in red) and both electromagnetic and hadronic physics (in black).

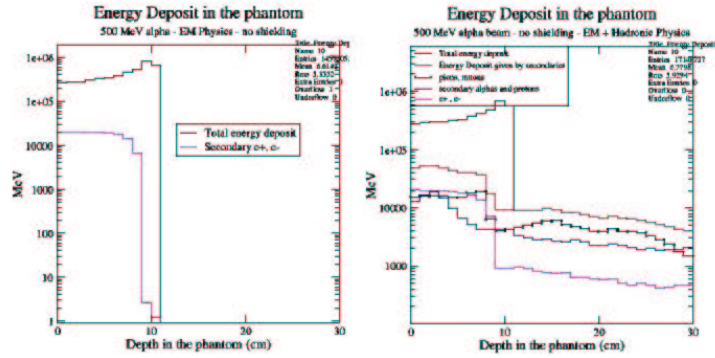


Figure 114: 500 MeV alpha beam; comparison of energy deposit in the Astronaut activating Geant4 electromagnetic physics only (first plot) and both electromagnetic and hadronic physics (second plot).

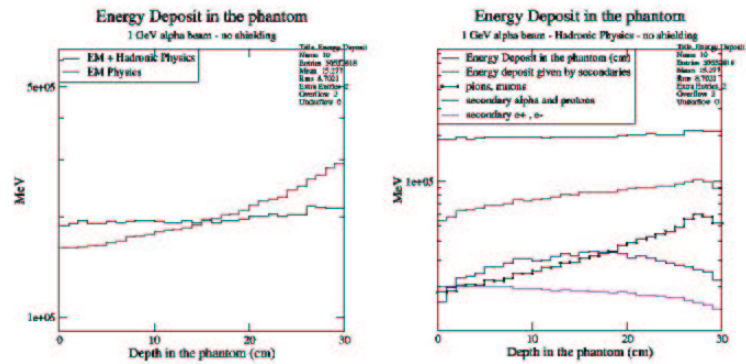


Figure 115: 1 GeV alpha beam; first plot: comparison of the energy deposit in the Astronaut obtained activating Geant4 electromagnetic physics only and both electromagnetic and hadronic physics. Second plot: analysis of the energy deposit in the Astronaut, resulting from secondary particles, with hadronic processes active.

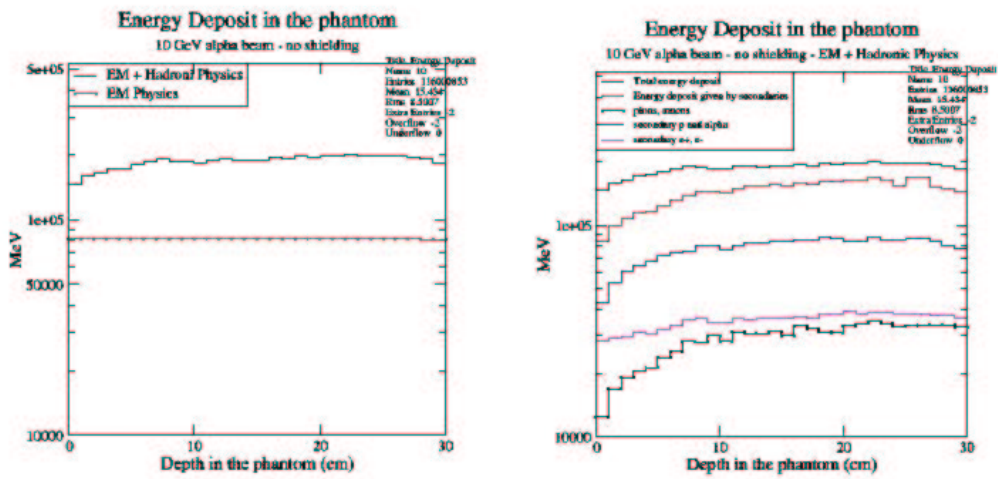


Figure 116: 10 GeV alpha beam; first plot: comparison of the energy deposit obtained activating Geant4 electromagnetic physics only and both electromagnetic and hadronic physics. Second plot: analysis of the energy deposit in the Astronaut, resulting from secondary particles, with hadronic processes active. (second plot).

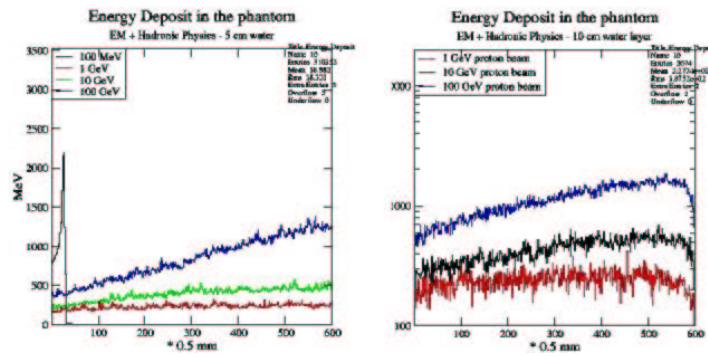


Figure 117: 100 MeV, 1 GeV, 10 GeV, 100 GeV monochromatic proton beams hit the basic multilayer structure with 5. cm (first plot) and 10. cm water shielding (second plot).

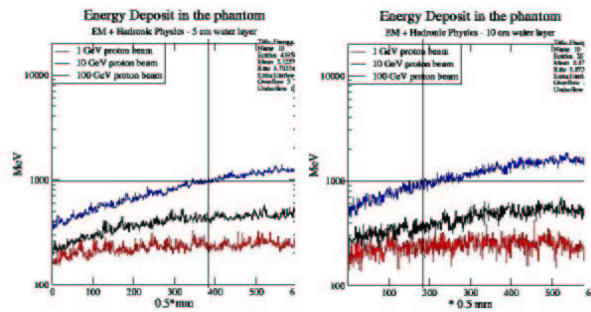


Figure 118: 1 GeV, 10 GeV, 100 GeV monochromatic proton beams hit the basic multilayer structure with 5. cm (first plot) and 10. cm water shielding (second plot).

Fig. 119, 120, 121 show the energy deposit resulting from 500. MeV, 1. GeV, 10. GeV monochromatic alpha particle beams shot against the basic multilayer structure with 10. cm water shielding. Fig. 122, 123, 124 illustrate the energy deposit in the presence of the basic multilayer structure with no shielding and with 10. cm water shielding. Fig. 125 shows the energy deposit in the Astronaut resulting from monochromatic 1 GeV, 10 GeV, 100 GeV proton beams impinging on the basic multilayer structure with 10. cm polyethylene and with 10. cm water shielding. Fig. 126 illustrates the energy deposit in the Astronaut resulting from monochromatic 500. MeV, 1. GeV, 10. GeV alpha beams shot against the basic multilayer structure with 10. cm polyethylene shielding. Fig. 127, 128, 129 show the the comparison of the energy deposit in the Astronaut resulting from monochromatic 500. MeV, 1. GeV, 10. GeV alpha particle beams in the

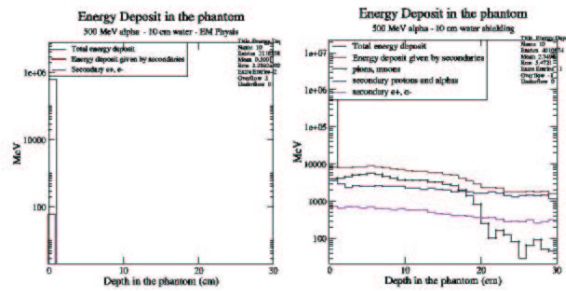


Figure 119: Monochromatic 500. MeV alpha beams hitting the basic multilayer structure with 10. cm water shielding activating Geant4 electromagnetic physics only (first plot), both electromagnetic and hadronic physics (second plot).

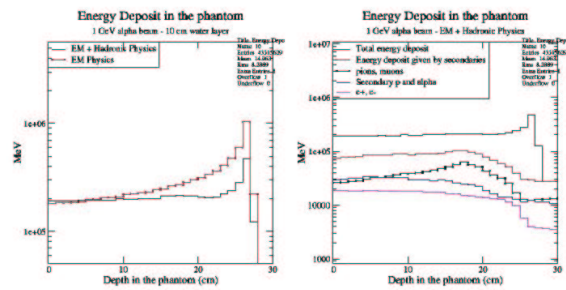


Figure 120: Monochromatic 1. GeV alpha beams hitting the basic multilayer structure with 10. cm water, activating the electromagnetic physics only (first plot), both electromagnetic and hadronic physics (second plot).

configuration of basic multilayer structure with 10. cm water and 10. cm polyethylene shielding; both Geant4 electromagnetic and hadronic processes are active.

From the results, we can infer that in most cases the thicker water shielding limits the energy deposit in the Astronaut. However, with primary 100. GeV protons, a high energy deposit in the Astronaut is observed in the configuration of 10. cm with respect to 5. cm water shielding. The 10. cm water and 10. cm polyethylene shielding exhibit a similar behaviour.

9.7 Second iteration: study with GCR protons and alpha particles

The effect of the hadronic processes has been studied in the same experimental configuration with the GCR protons and alpha particles.

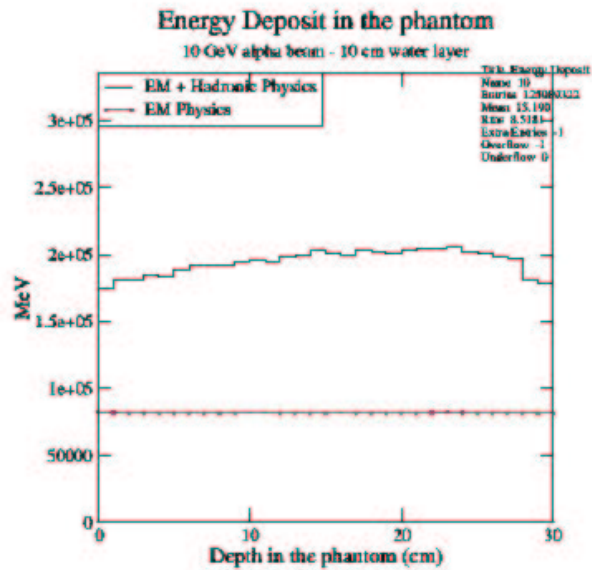


Figure 121: Monochromatic 10. GeV alpha beam hitting the basic multilayer structure with 10. cm water shield activating the electromagnetic physics only and both electromagnetic and hadronic physics.

Fig. 130 shows the energy deposit in the Astronaut resulting from GCR proton and alpha particles, shot against the basic multilayer structure with 10. cm water shielding, activating Geant4 electromagnetic physics only and both electromagnetic and hadronic physics.

Fig. 131 and 132 illustrate the energy deposit in the Astronaut resulting from high energy GCR protons and alpha particles shot against the basic multilayer structure with 10. cm water shielding. Fig. 133 and 134 illustrate the energy deposit in the Astronaut, resulting from GCR and high energy GCR proton and alpha beams impinging on the basic multilayer structure with 5. cm water shielding. Fig. 135 shows the the energy deposit in the Astronaut resulting from GCR particles, interacting with the basic multilayer structure with 5. cm and 10. cm water shielding respectively. Fig. 136 shows the the energy deposit in the Astronaut resulting from high energy GCR particles in the same configuration as above. Fig. 136 illustrates the energy deposit in the Astronaut resulting from GCR protons and alpha particles impinging on the basic multilayer structure with 10. cm polyethylene shielding. Fig. 137 illustrates the contribution from high energy GCR protons and alpha particles in the same configuration. This plot, differently from the others comparing the effects of water and polyethylene shielding, exhibits a different behaviour

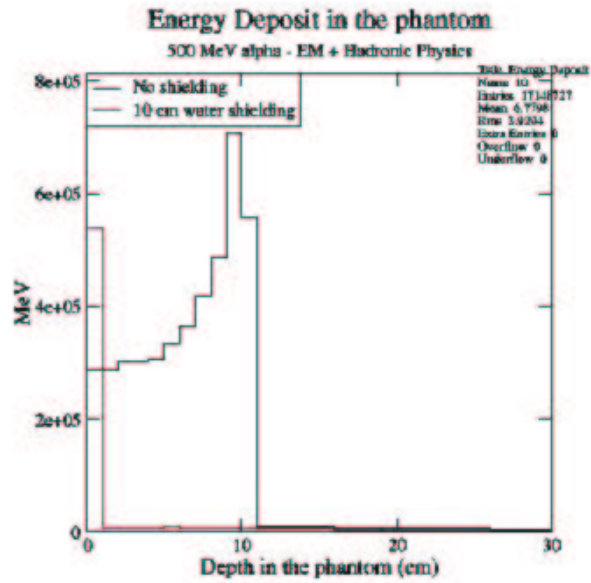


Figure 122: Monochromatic 500 MeV alpha particle beam shot against the basic multi-layer structure with no shielding and with 10. cm water. Both Geant4 electromagnetic and hadronic processes are active.

in the two cases; however, before reaching hasty conclusions about the relative shielding power of the two materials for high energy GCR alpha particles, further investigations about the reliability of Geant4 hadronic models for alpha particles should be performed.

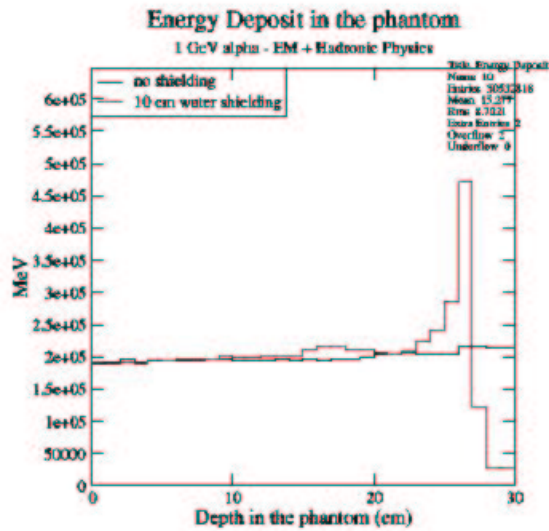


Figure 123: Monochromatic 1 GeV alpha beam shot against the basic multilayer structure with no shielding and with 10. cm water. Both Geant4 electromagnetic and hadronic processes are active.

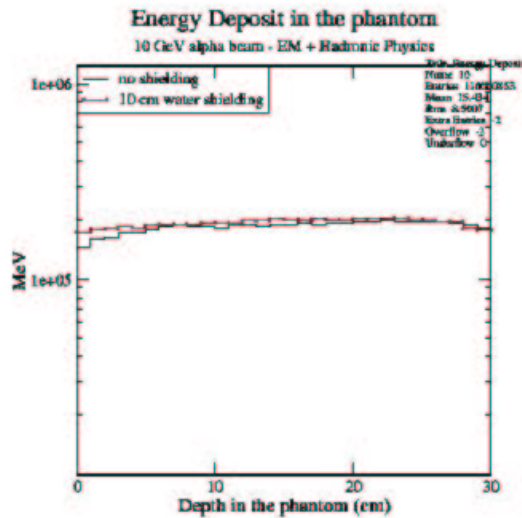


Figure 124: Monochromatic 10 GeV alpha beam shot against the basic multilayer structure with no shielding and with 10. cm water. Both Geant4 electromagnetic and hadronic processes are active.

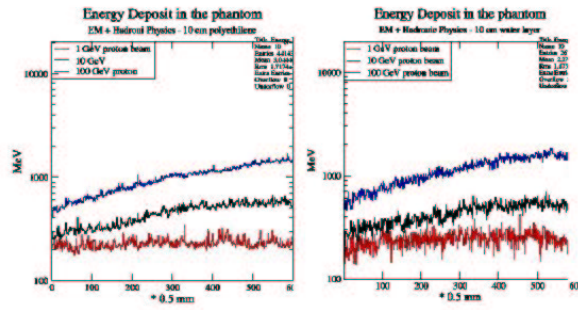


Figure 125: Monochromatic 1. GeV, 10. GeV, 100. GeV proton beams impinging on basic multilayer structure with 10. cm polyethylene (first plot) and with 10. cm water shielding (second plot). Both Geant4 electromagnetic and hadronic processes are active.

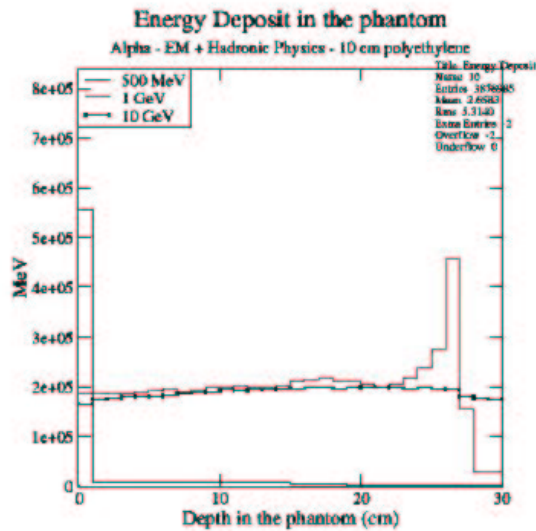


Figure 126: Energy deposit resulting from monochromatic (500. MeV, 1. GeV, 10. GeV) alpha beams in the case of a 10. cm polyethylene shielding.

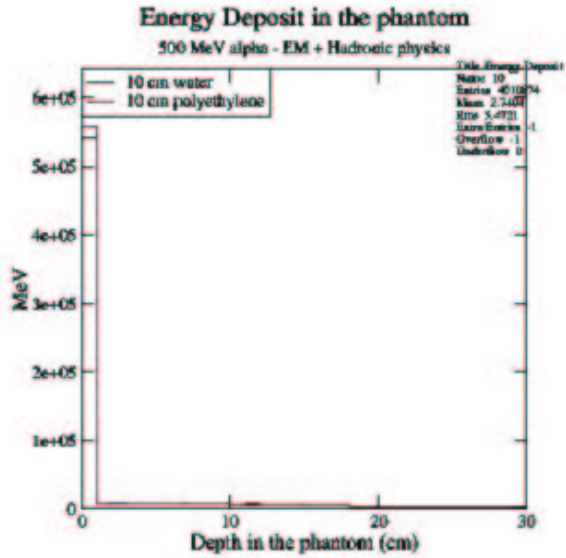


Figure 127: 500 MeV alpha beam: comparison of the energy deposit in the Astronaut in the configurations multilayer + 10. cm water and multilayer + 10. cm polyethylene.

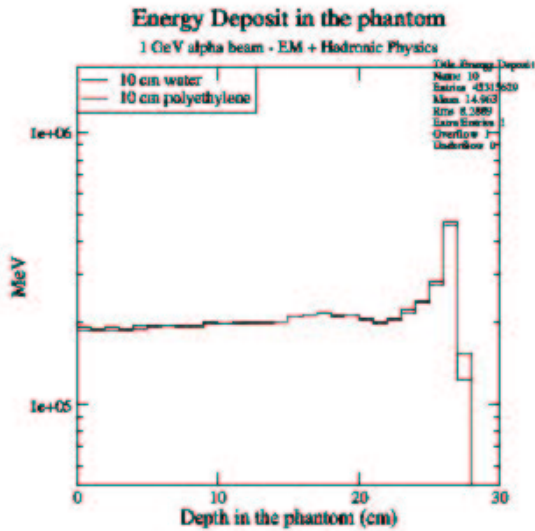


Figure 128: 1GeV alpha beam: comparison of the energy deposit in the Astronaut in the configurations multilayer+ 10. cm water and multilayer + 10. cm polyethylene.

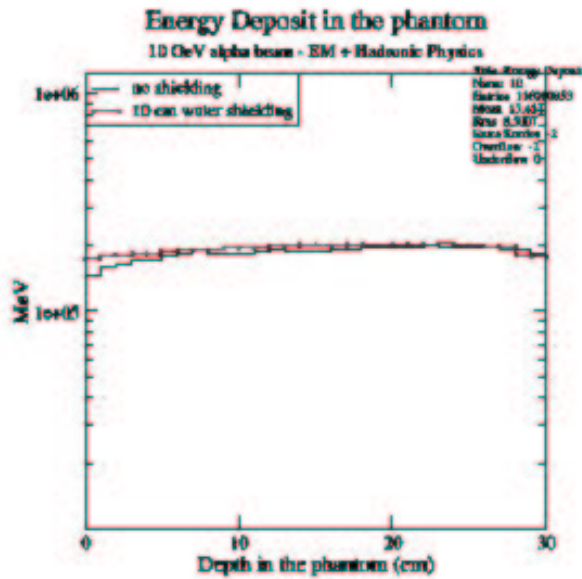


Figure 129: 10GeV alpha beam: comparison of the energy deposit in the Astronaut in the configurations multilayer+ 10. cm water and multilayer + 10. cm polyethylene.

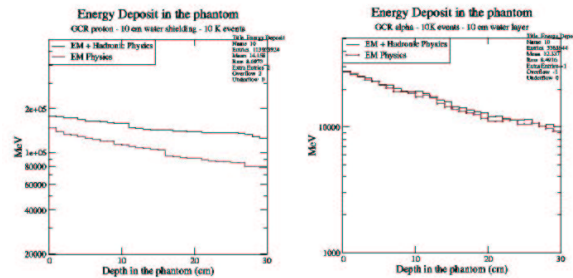


Figure 130: Energy deposit in the Astronaut resulting from GCR proton beam (first plot) and GCR alpha beam (second plot), impinging on the basic multilayer structure with 10. cm water shielding, activating Geant4 electromagnetic and both electromagnetic and hadronic processes.

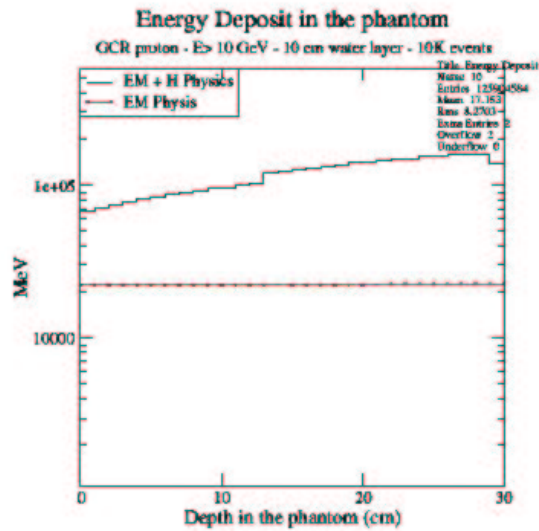


Figure 131: Energy deposit in the Astronaut, resulting from high energy GCR proton beam, impinging on the basic multilayer with 10. cm water shielding, activating Geant4 electromagnetic physics only and both electromagnetic and hadronic physics.

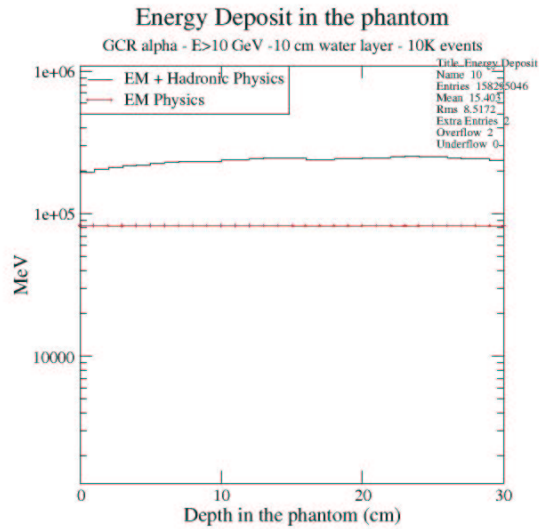


Figure 132: Energy deposit in the Astronaut, resulting from high energy GCR alpha beam, impinging on the basic multilayer structure with 10. cm water shielding activating Geant4 electromagnetic processes only and both electromagnetic and hadronic processes.

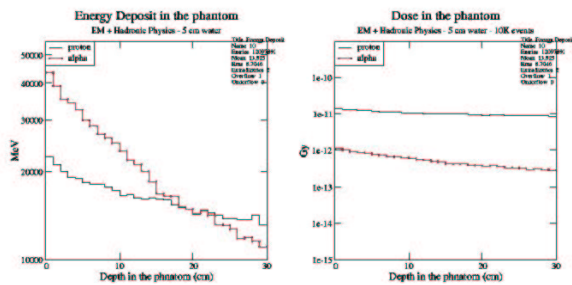


Figure 133: Energy deposit in the Astronaut resulting from GCR proton and a lpha beam interacting with the basic multilayer structure and 5. cm water shielding, activating Geant4 electromagnetic physics only and both electromagnetic and hadronic physics.

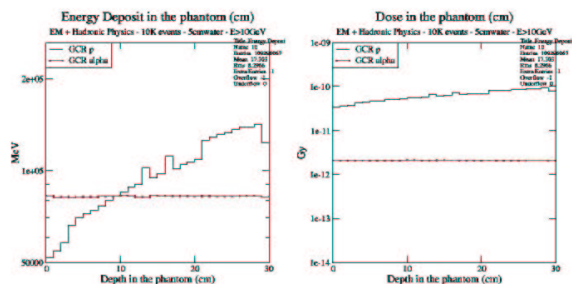


Figure 134: Energy deposit in the Astronaut resulting from high energy GCR proton and alpha beam interacting with the basic multilayer structure and 5. cm water shielding, activating Geant4 electromagnetic physics only and both electromagnetic and hadronic physics.

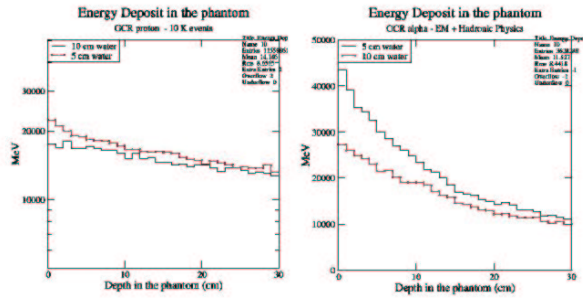


Figure 135: Energy deposit in the Astronaut with the activation of both electromagnetic and hadronic physics resulting from GCR protons (first plot), GCR alpha particle (second plot) with two different shielding options(5.cm water, 10. cm water).

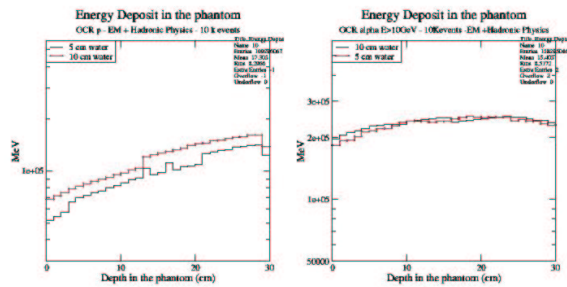


Figure 136: Energy deposit in the Astronaut with the activation of both electromagnetic and hadronic physics resulting from high energy GCR protons (first plot) and alpha particles (second plot) with two different shielding options(5.cm water, 10. cm water).

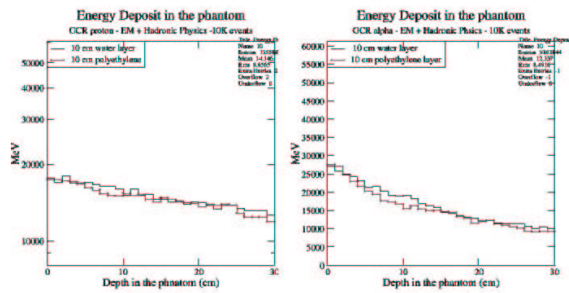


Figure 137: Energy deposit in the Astronaut resulting from GCR protons (first plot) and GCR alpha particles (second plot), hitting the basic multilayer structure with 10. cm polyethylene and 10. cm water shielding, activating both electromagnetic and hadronic processes.

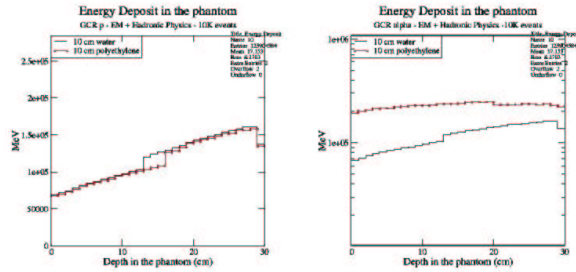


Figure 138: Energy deposit in the Astronaut resulting from GCR protons (first plot) and GCR alpha particles (second plot), hitting the basic multilayer structure with 10. cm polyethylene and 10. cm water shielding, activating both electromagnetic and hadronic processes.

9.8 Conclusions

This preliminary study of the dosimetric effects of hadronic interactions indicates that such contributions should be taken into account and may be significant. However, since Geant4 hadronic physics is still a domain under development, and validation studies are still in progress, the results collected in this section should not be treated as conclusive. We recommend more in depth studies of the dosimetric contributions from hadronic interactions at a later stage.

10 Study of vehicle concepts: protection from SPE

Special structures are required to protect the crews from the effects of Solar Particle Events. This section illustrates the study of configurations of vehicle concepts especially designed for the protection from Solar Particle Events.

10.1 Model of the experimental set-up

The experimental set-up adopted in this phase of the study derives from the sketch of vehicle concept [24], provided by ALENIA-SPAZIO (fig. 139). In ALENIA-SPAZIO sketch, the Simplified Inflatable Habitat (SIH) concept is complemented by a shelter consisting of a water cylinder.

At this stage of the study, the geometrical model provided by ALENIA-SPAZIO was

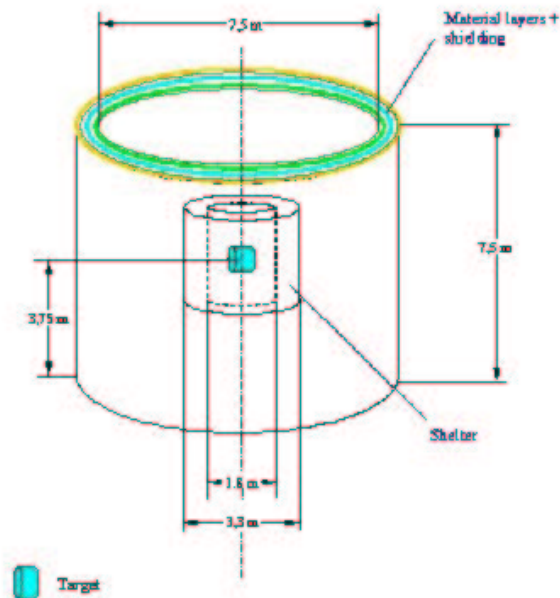


Figure 139: Model of the vehicle habitat [24]: the Simplified Inflatable Habitat (SIH) concept is complemented by a cylinder of water (called shelter), set in the center of the vehicle. The Astronaut (called Target) is placed inside the shelter.

simplified to its essential characteristics suitable for a preliminary evaluation of dosimetric effects.

The simplified geometrical configuration (fig. 140) consists of an additional layer of water (corresponding to the shelter concept), of 0.75 m thickness, placed in between the

basic multilayer with its 10. cm water shielding and the Astronaut, at a distance of 2.1 m from the multilayer structure. This geometrical configuration will be referred to as *shelter configuration* in the following.

The primary particles are shot against the experimental set-up as shown in figure 141, with direction parallel to the Z axis.

The result of the simulation is the energy deposit versus the depth in the Astronaut.

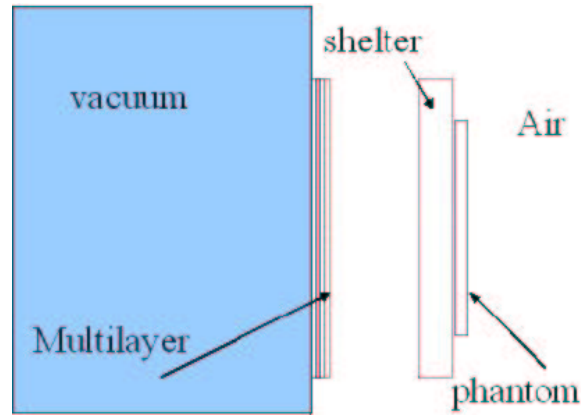


Figure 140: Geometrical configuration for the study of SPE shelter.

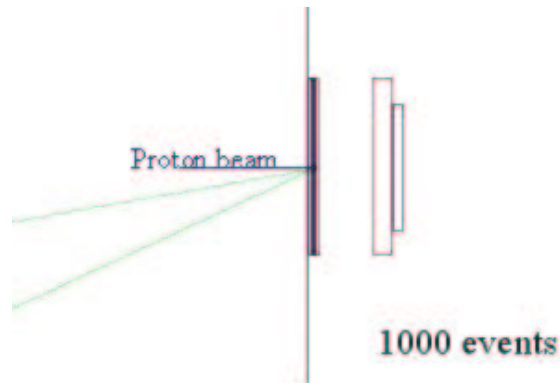


Figure 141: Experimental set-up for the study of the SPE radioprotection: a particle beam impinges on the multilayer structure with 10. cm water shielding complemented by an additional shelter.

10.2 Strategy of the study

The dosimetric study has been performed in two steps; in the first phase only electromagnetic processes have been activated, in the second one hadronic processes have been added. This procedure has been adopted to isolate the effects of hadronic physics from the electromagnetic interactions.

The dosimetric study has been done for the following primary particles components:

- GCR protons, alpha particles, C-12, O-16, Si-28, Fe-52 ions,
- SPE protons and alpha particles.

The GCR components have been studied to verify whether they could originate harmful effects.

Special production limited to the high energy part of the GCR ($E > 10\text{GeV}$) and SPE ($E > 300\text{MeV}$ and $E > 10\text{GeV}$) have been performed to obtain statistically significant results.

10.3 Study of the shelter with Galactic Cosmic Rays

Fig. 142 and 143 show the energy deposit and the dose in the Astronaut resulting from Galactic Cosmic Rays interacting with the experimental set-up shown above. Geant4 electromagnetic processes are activated only. Fig. 144, 145, 146, 147 show a set of results deriving from high energy GCR particles shot against the shelter configuration. The Fe-52 ions are completely absorbed in the shelter structure.

Fig. 148 shows the energy deposit and the corresponding dose in the Astronaut, resulting from high energy GCR particles.

10.4 Study of the shelter with Solar Particle Events

The same studies described in the previous sections have been repeated with SPE spectra as primary particles.

Fig. 149), resulting from 10 K events SPE and GCR protons and alpha particles generated, shows that the additional water layer absorbs the SPE particles almost completely, while the GCR proton and alpha components reach the Astronaut. This effect is due to the different behaviour (fig. 150) of the flux curves as a function of energy in the two cases. Therefore, the energy deposit and dose distributions (fig. 151) resulting from SPE particles in this configuration are not statistically significant. The simulations have been repeated considering the higher energy ($E > 300\text{MeV}$, $E > 10\text{GeV}$) components of the SPE spectrum only to obtain statistically significant results.

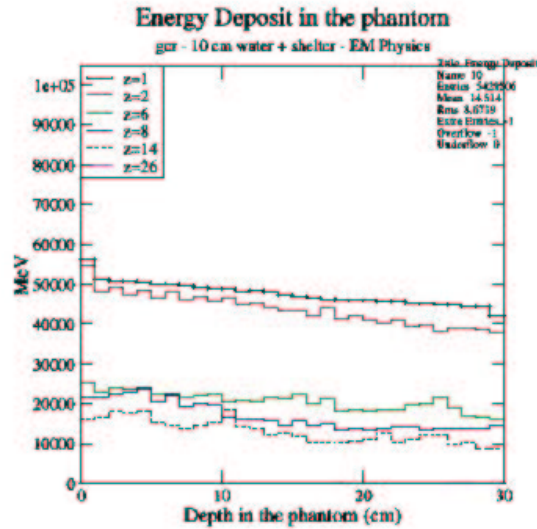


Figure 142: Energy deposit in the Astronaut resulting from GCR particles interacting with the shelter configuration.

Fig. 152 illustrates the energy deposit and the corresponding dose in the Astronaut resulting from $SPE_{E>300MeV}$, interacting with the shelter configuration.

The dose should be weighted according to the relative probability of generating a $SPE E > 300MeV$ particles with respect to the original SPE energy spectra.

Fig. 153 shows the fraction of $SPE_{E>300MeV}$ primary particles reaching and traversing the Astronaut. Fig. 154 shows the initial energy of primary high energy ($E > 10GeV$) SPE particles reaching and traversing the Astronaut.

Fig. 155 illustrates the energy deposit and the corresponding dose in the Astronaut resulting from SPE particles.

10.5 Contribution of hadronic processes

Fig. 156 illustrates the energy deposit in the Astronaut resulting from Geant4 electromagnetic processes only and both electromagnetic and hadronic interactions of GCR particles with the shelter configuration. Fig. 157 shows the energy deposit in the Astronaut resulting from high energy GCR particles activating Geant4 electromagnetic processes only and both electromagnetic and hadronic processes. Fig. 158 illustrates the energy deposit in the Astronaut resulting from $SPE_{E>300MeV}$ and $SPE_{E>10GeV}$ in the shelter configuration, activating both Geant4 electromagnetic and hadronic processes.

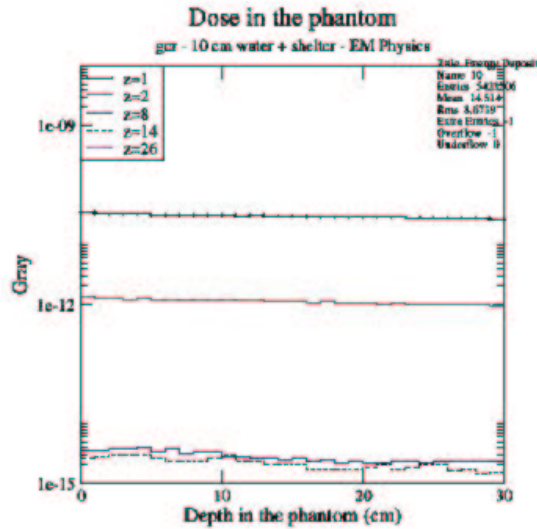


Figure 143: Dose in the Astronaut resulting from GCR particles interacting with the shelter configuration.

10.6 Conclusions

The additional shielding layer constituting the shelter has the effect of absorbing most of the SPE particles. Some fraction of GCR particle reaches the Astronaut even in the presence of the shelter layer, except for the GCR Fe-52 ion component, which is completely absorbed.

This preliminary study indicates that the contribution of hadronic interactions should be taken into account in the design of the SPE shelter, since its effects may be significant. However, since Geant4 hadronic physics is still a domain under development, and validation studies are still in progress, we recommend more in depth studies at a later stage.

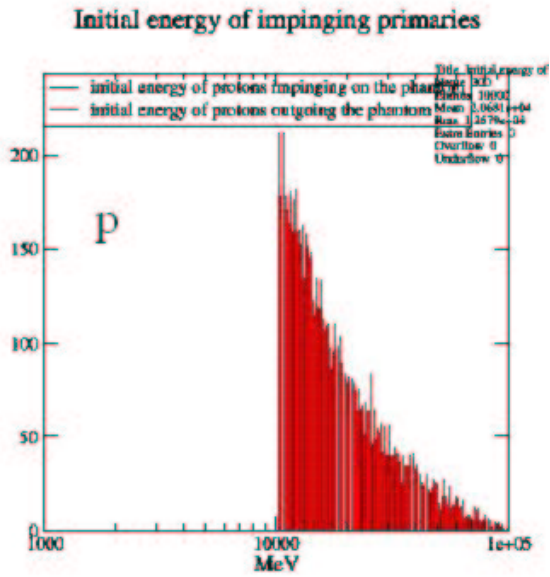


Figure 144: Shelter configuration; initial energy of high energy GCR protons hitting the Astronaut (histogram in black), initial energy of high energy GCR protons traversing the Astronaut.

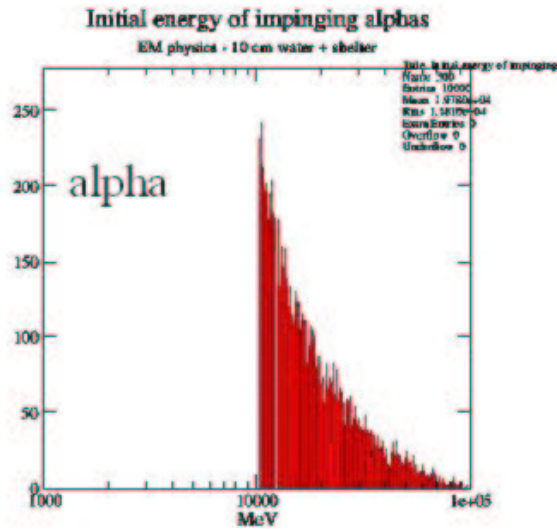


Figure 145: Shelter configuration; initial energy of high energy GCR alpha particles hitting the Astronaut (histogram in black), initial energy of high energy GCR alpha particles traversing the Astronaut.

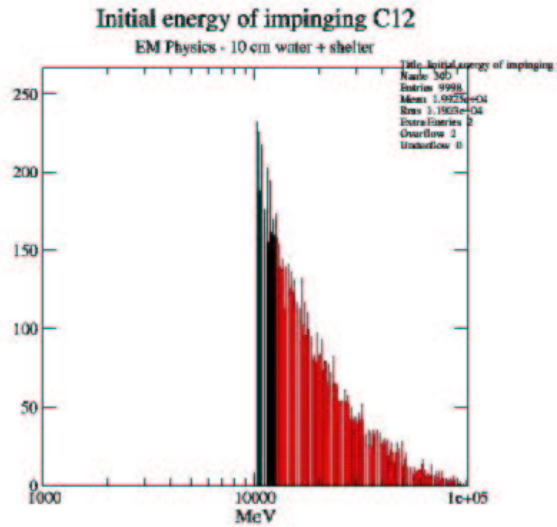


Figure 146: Shelter configuration; initial energy of high energy GCR C-12 ions hitting the Astronaut (histogram in black), initial energy of high energy GCR C-12 ions traversing the Astronaut.

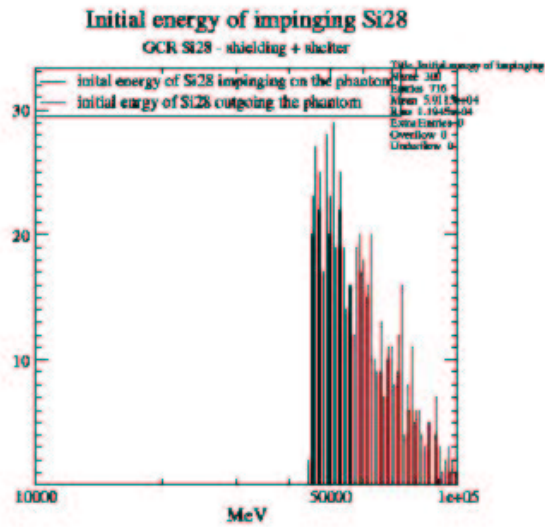


Figure 147: Shelter configuration; initial energy of high energy GCR Si-28 ions hitting the Astronaut (histogram in black), initial energy of high energy GCR Si-28 ions traversing the Astronaut.

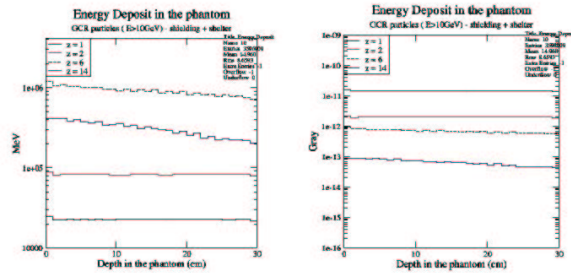


Figure 148: Energy deposit and the corresponding dose in the Astronaut resulting from high energy GCR particles interacting with the shelter configuration.

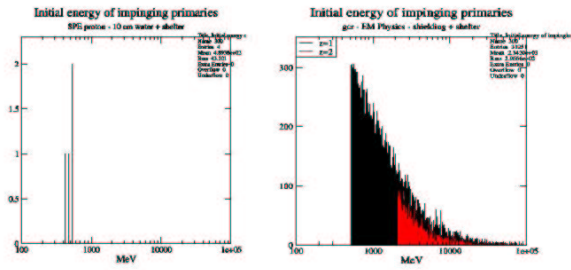


Figure 149: First plot: primary SPE protons reaching the Astronaut (SPE alpha particles are completely absorbed in the shelter layer); second plot: primary GCR protons and alpha particles reaching the Astronaut. The same number of primary events is generated in the two cases.

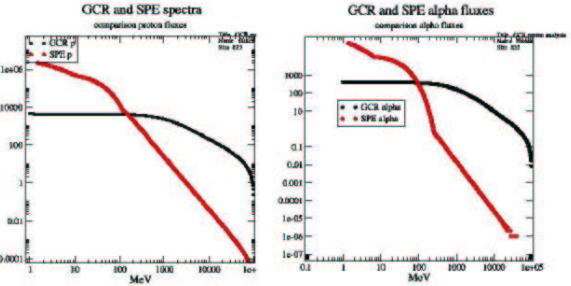


Figure 150: Energy spectrum of GCR and SPE protons (first plot), energy spectrum of GCR and SPE alpha particles (second plot).

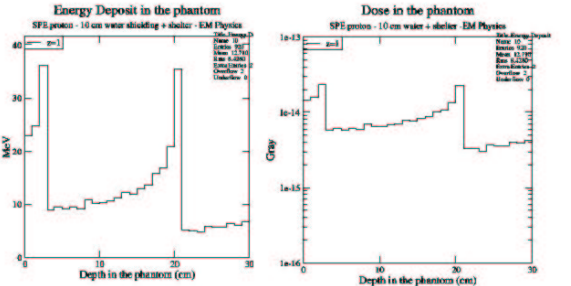


Figure 151: Energy deposit (first plot) and corresponding dose (second plot) in the Astronaut resulting from SPE protons in the shelter configuration. Alpha particles are completely stopped by the shelter layer.

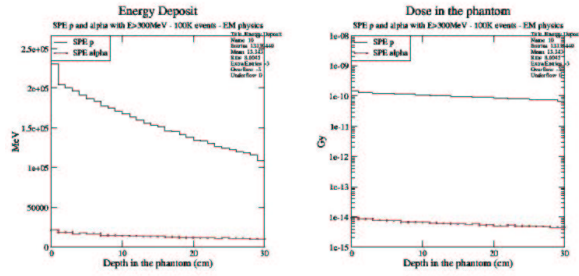


Figure 152: Energy deposit and correspondent dose in the Astronaut resulting from $SPE_{E>300MeV}$ protons and alpha particles.

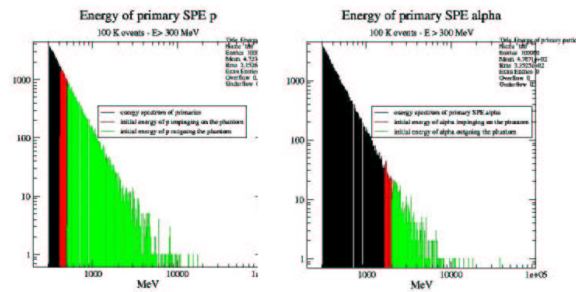


Figure 153: Primary energy (in black), initial energy of $SPE_{E>300MeV}$ particles reaching the Astronaut (in red), initial energy of $SPE_{E>300MeV}$ particles traversing the Astronaut (in green). SPE protons are on the left, SPE alpha particles on the right.

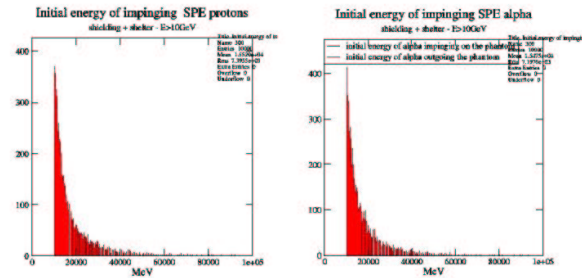


Figure 154: Initial energy of primary high energy SPE particles reaching (black histogram) and traversing the Astronaut (red histogram); SPE protons are on the left, SPE alpha on the right.

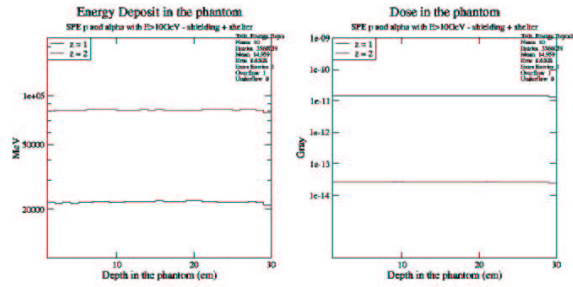


Figure 155: Energy deposit and dose in the Astronaut resulting from SPE protons and alpha particles interacting with the shelter configuration.

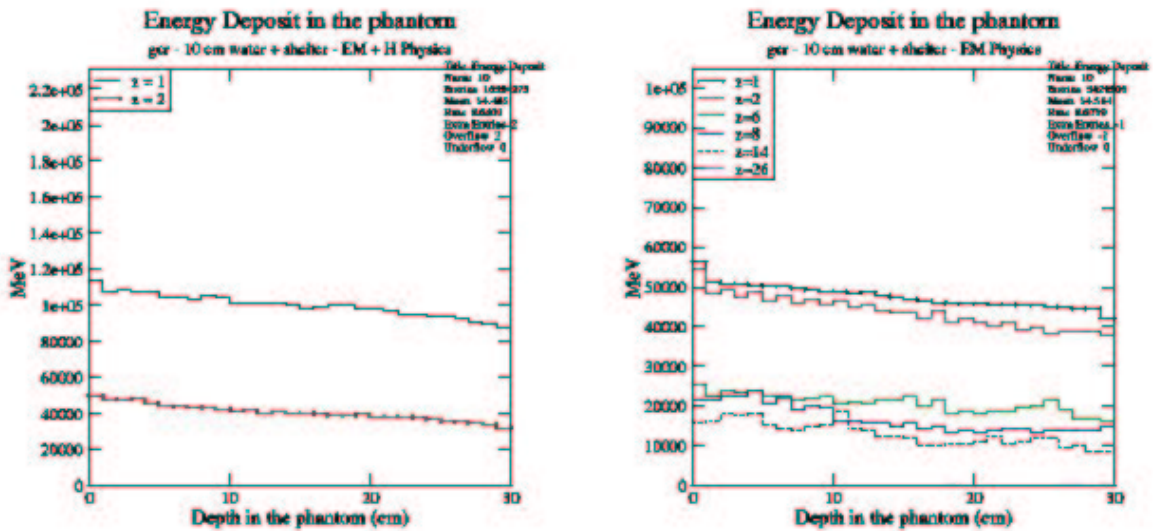


Figure 156: Energy deposit in the Astronaut resulting from GCR particles, activating both Geant4 electromagnetic and hadronic physics (first plot) and the electromagnetic processes only (second plot).

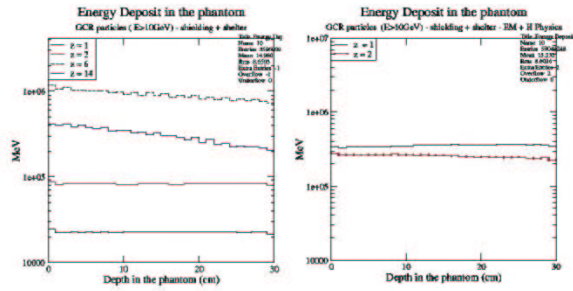


Figure 157: Energy deposit in the Astronaut resulting from GCR particles activating Geant4 electromagnetic interactions only (first plot) and both electromagnetic and hadronic processes (second plot).

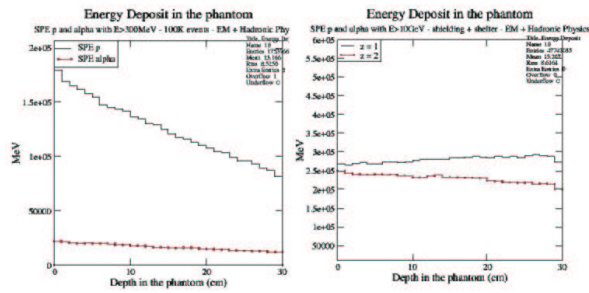


Figure 158: Energy deposit resulting from $SPE_{E>300MeV}$ (first plot) and $SPE_{E>10GeV}$ particles, activating both hadronic and electromagnetic physics.

11 Moon habitats

This section is dedicated to the study of the dosimetric effect of GCR and SPE particles in moon habitats, conceived to protect the crews from harmful effects resulting from the radiation on the moon surface.

11.1 Model of the experimental set-up

ALENIA-SPAZIO provided the sketch of moon habitat concepts [27]; its significant conceptual characteristics, relevant to simulation study in the REMSIM context, have been identified, and simplified geometrical configurations have been modeled, reflecting these characteristics.

The experimental set-up adopted in this phase of the study corresponds to the moon surface habitats illustrated in fig. 159; the habitat consists in a moon soil shelter, the Astronaut is set inside it. In fig. 159 X indicates the height of the pyramid log set on the moon surface. 0.5 m moon soil is placed between the pyramid log and the Astronaut's shelter. The moon surface habitat has been modeled in Geant4 REMSIM application as shown in fig. 160. Two different geometrical configuration have been considered; one corresponds to the moon surface habitat with $X = 0$. and the other one to the habitat solution with $X = 3$. m. The dosimetric effect of:

- GCR protons, alpha particles, C-12, O-16, Si-28, Fe-52 ions,
- SPE protons and alpha particles with initial energy $E > 300MeV$,
- high energy GCR protons, alpha particles, C-12, O-16, Si-28, Fe-52 ions,
- high energy SPE protons and alpha particles.

has been studied in this configuration, activating in a first moment the Geant4 electromagnetic processes only, then adding the hadronic physics component.

The Astronaut is a water box set inside the moon habitat, sliced in 1 cm thick voxels along the Z axis. The result of the simulation is the energy deposit versus the depth in the Astronaut.

11.2 Strategy

A preliminary study has been done with a simple configuration to obtain a first evaluation of the shielding effect of the moon soil layer: the geometry consists of a single slab of moon soil in front of the Astronaut phantom; primary particles according to GCR spectra are shot perpendicularly to the moon slab; Geant4 electromagnetic physics only has been

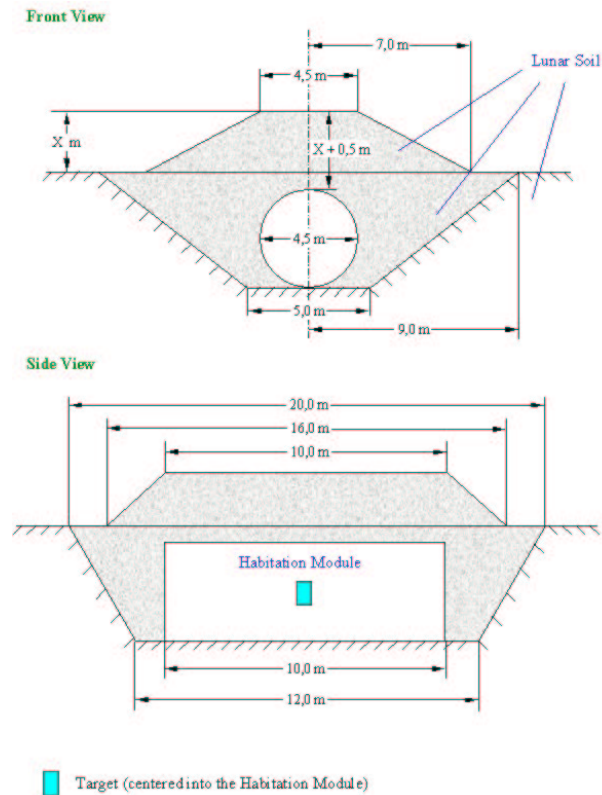


Figure 159: Moon surface habitats [27]; X can be 0., 1., 2., 3. m.; the material of the habitat is moon soil. The Astronaut is placed inside the shelter.

activated.

A more refined study has been performed in a more complex configuration: the geometry consists of moon habitat models with different shielding options; primary particles, according to GCR spectra, are generated according to a more realistic angular distribution; Geant4 electromagnetic physics only has been activated. This study has been repeated for $SPE_{E>300MeV}$ and for high energy GCR and SPE particles.

Finally, the contribution of hadronic processes has been evaluated.

11.3 Preliminary study of moon soil shielding effects

The experimental set-up adopted in this phase is shown in fig. 161, where the moon soil thickness has been fixed equal to 0.5 m and 3.5 m (corresponding to $X = 0.$ m and $X = 3.$ m in the moon habitat configuration). The Astronaut is set behind the moon soil layer.

GCR particles are generated perpendicularly to the moon soil slab, Geant4 electromag-

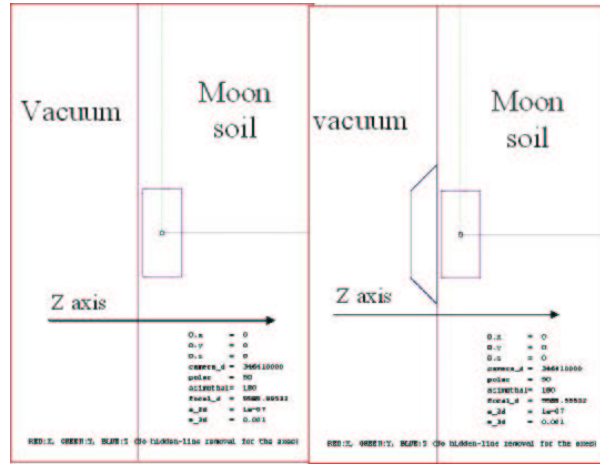


Figure 160: Experimental set-ups corresponding to moon surface habitats (fig. 159) with $X = 0$. m (first plot) and $X = 3$. m (second plot).

netic processes are active only.

The results, shown in fig. 162, 163, 164, 165, 166, illustrate the initial energy of GCR primary particles (in black), the initial energy of GCR primary particles reaching the Astronaut (in red), the initial energy of GCR primary particles traversing the Astronaut (in green). The results are collected in tab. 8. The Fe-52 ions are stopped by the moon soil layer². The study has been repeated in the experimental set-up shown in fig. 161 fixing

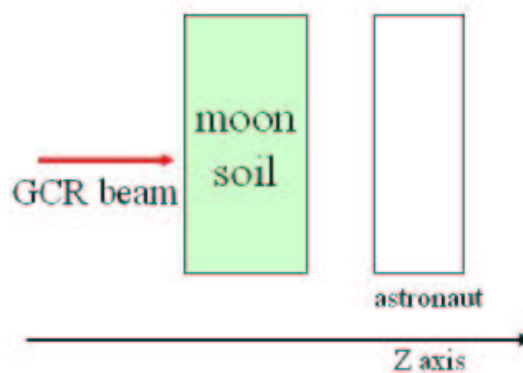


Figure 161: Geometrical set-up of the preliminary moon soil shielding study.

the moon soil thickness equal to 3.5 m.

²This statement has been verified shooting 100. GeV Fe-52 ions onto the moon soil layer.

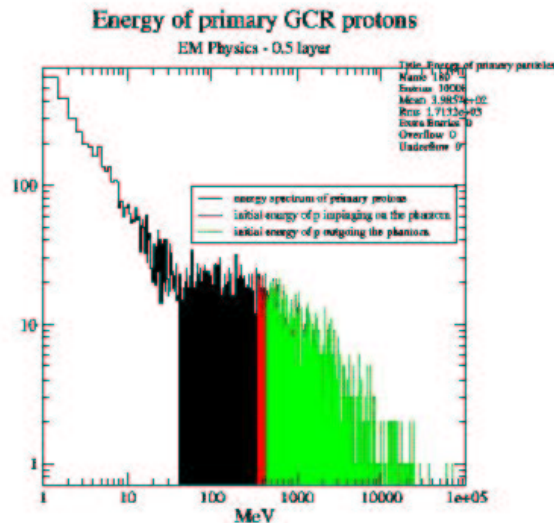


Figure 162: 0.5 m moon layer: initial energy (in black) of GCR protons, initial energy of GCR protons reaching the Astronaut (in red), initial energy of protons traversing the Astronaut (in green).

The results, shown in fig. 167, 168, 169 illustrate the initial energy of GCR primary particles (in black), the initial energy of GCR primary particles reaching the Astronaut (in red), the initial energy of GCR primary particles traversing the Astronaut (in green). The results are collected in tab. 9. The GCR Si-28 and Fe-52 ions are completely stopped by the 3.5 m thick moon soil ³. From this preliminary study, it is possible to infer that thicker slabs of moon soil limit the exposure of the Astronaut to harmful GCR and SPE radiation. Moreover this study has been useful to see which components of the GCR spectra reach the shelter.

11.4 Dosimetry in moon habitat concepts

The experimental set-up of the dosimetric study is shown in figure 170. The primary particles are generated with energies according to the GCR and SPE spectra. The primary vertex is generated on the hemisphere shown in figure 170; the radius has been fixed equal to about 3 times the largest size of the habitat concept. The initial direction of the primary particles is randomized as illustrated in fig. 171: it can vary within the region indicated by the arrows. Fig. 173 shows the energy deposit and the dose in the Astronaut resulting

³This statement has been verified shooting 100. GeV Fe-52 ions onto the moon soil layer.

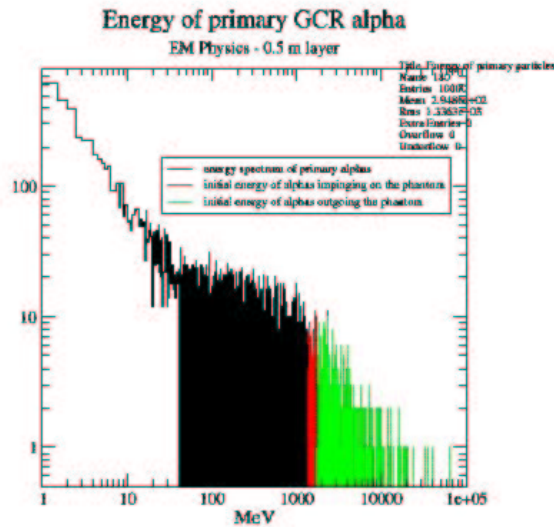


Figure 163: 0.5 m moon layer: initial energy (in black) of GCR alpha particles, initial energy of GCR alpha particles reaching the Astronaut (in red), initial energy of GCR alpha particles traversing the Astronaut (in green).

from GCR particles. The habitat concept analysed corresponds to the configuration without the pyramid log (illustrated in fig.172). An analysis of the primary particles reaching the Astronaut is shown in fig. 174. The initial energy of generated primaries is black, the initial energy of primaries reaching the Astronaut is red, the initial energy of primaries traversing the Astronaut is green. Fig. 175 shows that few C12 ions reach the Astronaut; as a consequence the energy deposit calculation is affected by very low statistics. This holds also for the other heavy ions. Specialised studies limited to the high energy and of the GCR spectrum have proven to require too much computation time to be practically feasible with the available computing resources.

Fig. 176 shows the energy deposit and the dose in the Astronaut resulting from $SPE_{E>300MeV}$.

The dosimetric study has been repeated in the experimental set-up shown in fig. 177, the primary particles are originated with the same conditions than before (see fig. 170). This configuration corresponds to the more radioprotective moon shelter (X = 3. m). Fig. 178 shows the energy deposit and the dose in the Astronaut given by the GCR radiation environment.

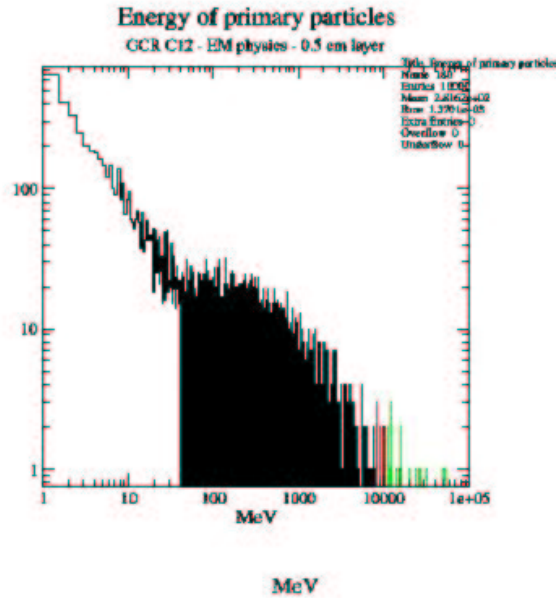


Figure 164: 0.5 m moon layer: initial energy (in black) of GCR C-12 ions, initial energy of GCR C-12 ions reaching the Astronaut (in red), initial energy of GCR C-12 ions traversing the Astronaut (in green).

Table 8: GCR particles interacting with 0.5 m moon soil; region 1 indicates the initial energy of GCR primary particles absorbed in the soil layer; region 2 refers to the initial energy of GCR primary particles absorbed in the Astronaut; region 3 refers to the initial energy of GCR primary particles traversing the Astronaut;

	Region 1	Region 2	Region 3
GCR p	$E < \sim 300.MeV$	$\sim 300.MeV < E < \sim 400.MeV$	$E > \sim 400.MeV$
GCR alpha	$E < \sim 1.GeV$	$\sim 1.GeV < E < \sim 1.5GeV$	$E > \sim 1.5GeV$
GCR C12 ions	$E < \sim 8.GeV$	$\sim 8.GeV < E < \sim 10.GeV$	$E > \sim 10.GeV$
GCR O16 ions	$E < \sim 10.GeV$	$\sim 10.GeV < E < \sim 20.GeV$	$E > \sim 20.GeV$
GCR Si28 ions	$E < \sim 30.GeV$	$\sim 30.GeV < E < \sim 45.GeV$	$E > \sim 45.GeV$

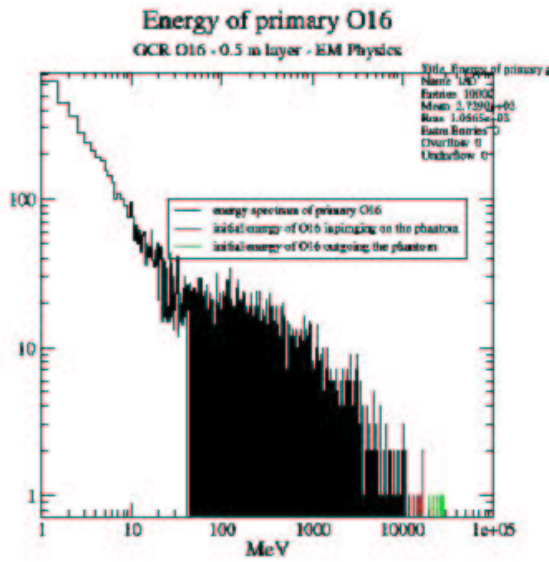


Figure 165: 0.5 m moon layer: initial energy (in black) of GCR O-16 ions, initial energy of GCR O-16 ions reaching the Astronaut (in red), initial energy of GCR O-16 ions traversing the Astronaut (in green).

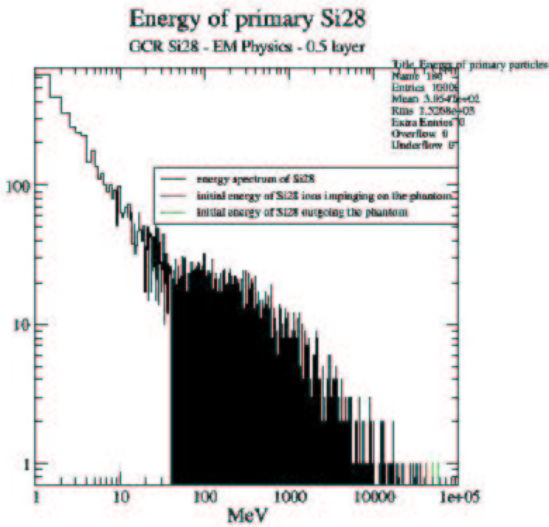


Figure 166: 0.5 m moon layer: initial energy (in black) of GCR Si-28 ions, initial energy of GCR Si-28 ions reaching the Astronaut (in red), initial energy of Si-28 ions traversing the Astronaut (in green).

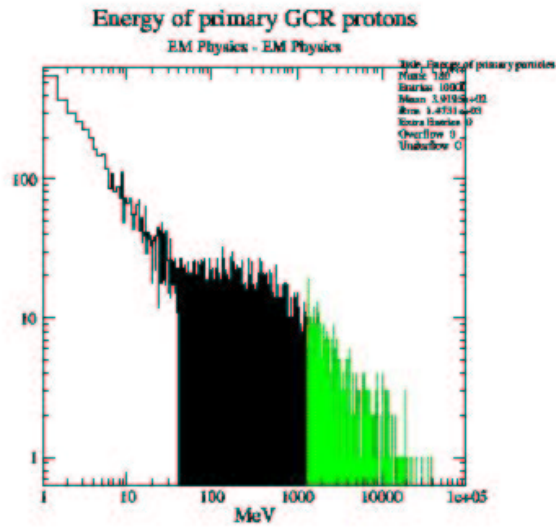


Figure 167: 3.5 m moon layer: initial energy (in black) of GCR protons, initial energy of GCR protons reaching the Astronaut (in red), initial energy of GCR protons traversing the Astronaut (in green).

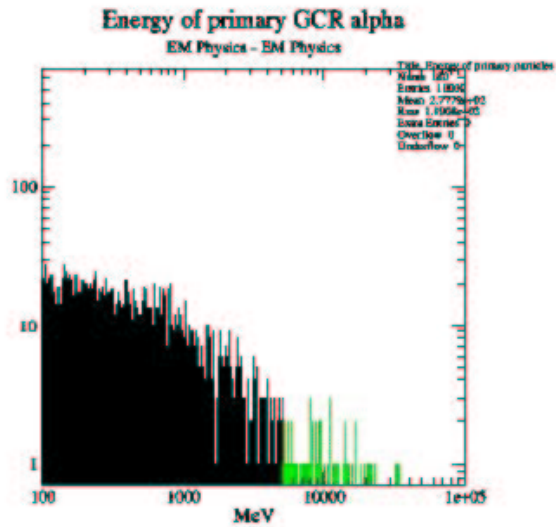


Figure 168: 3.5 m moon layer: initial energy (in black) of GCR alpha particles, initial energy of GCR alpha particles reaching the Astronaut (in red), initial energy of GCR alpha particles traversing the Astronaut (in green).

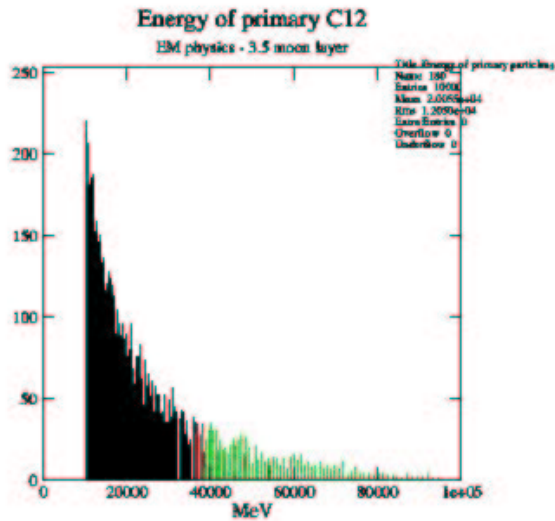


Figure 169: 3.5 m moon layer: initial energy (in black) of high energy GCR C-12 ions, initial energy of high energy GCR C-12 ions reaching the Astronaut (in red), initial energy of GCR C-12 ions traversing the Astronaut (in green).

Table 9: GCR particles impinging on 3.5 m moon soil; region 1 indicates the initial energy of GCR primary particles absorbed in the soil layer; region 2 refers to the initial energy of GCR primary particles absorbed in the Astronaut; region 3 refers to the initial energy of GCR primary particles traversing the Astronaut;

	Region 1	Region 2	Region 3
GCR p	$E < \sim 1.GeV$	$\sim 1.GeV < E < \sim 1.2GeV$	$E > \sim 1.2GeV$
GCR alpha	$E < \sim 5.GeV$	$\sim 5.GeV < E < \sim 5.5GeV$	$E > \sim 5.5GeV$
GCR C12 ions	$E < \sim 35.GeV$	$\sim 35.GeV < E < \sim 40.GeV$	$E > \sim 40.GeV$

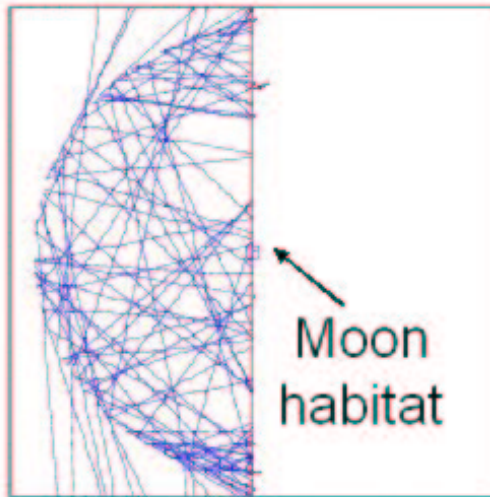


Figure 170: Generation of primary particles for moon habitat studies.

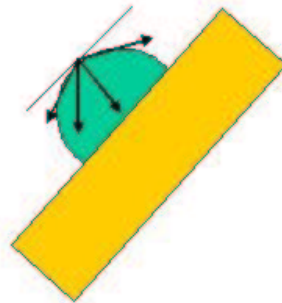


Figure 171: Initial direction of the primary particles generated in the experimental set-up shown in fig.170. It can vary within the region highlighted by the arrows.

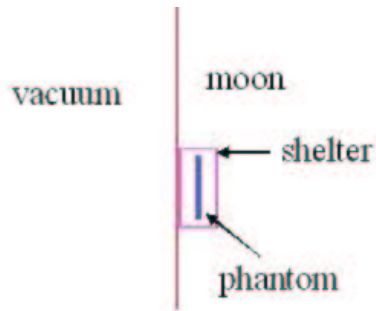


Figure 172: Experimental set-up adopted for the calculation of energy deposit in the Astronaut resulting from GCR and SPE particles generated according to fig. 170. The Astronaut is placed inside the shelter.

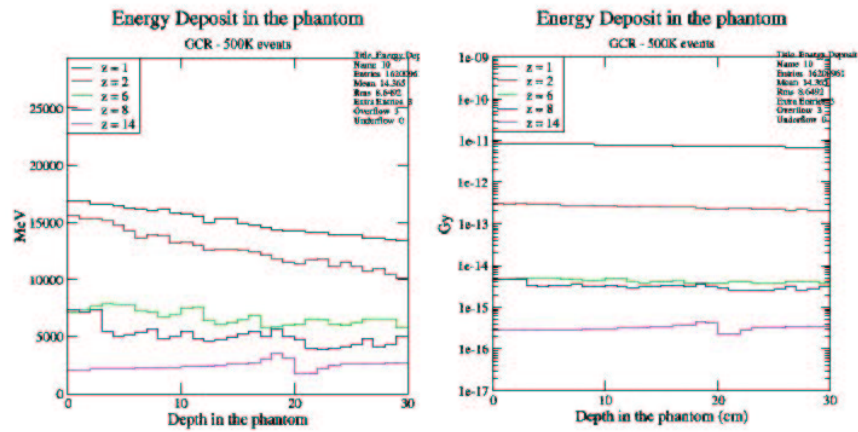


Figure 173: Energy deposit (first plot) and dose (second plot) in the Astronaut resulting from GCR particles ($X=0$).

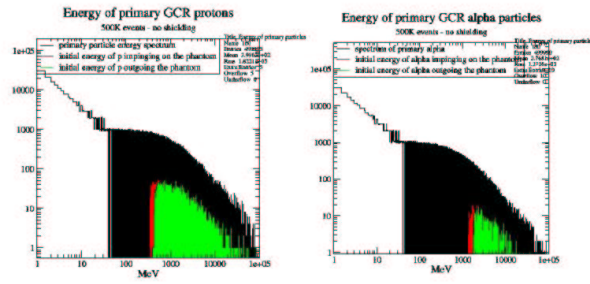


Figure 174: X =0.: initial energy of generated primaries is black, the initial energy for primaries reaching the Astronaut is red, the initial energy of primaries traversing the Astronaut is green.

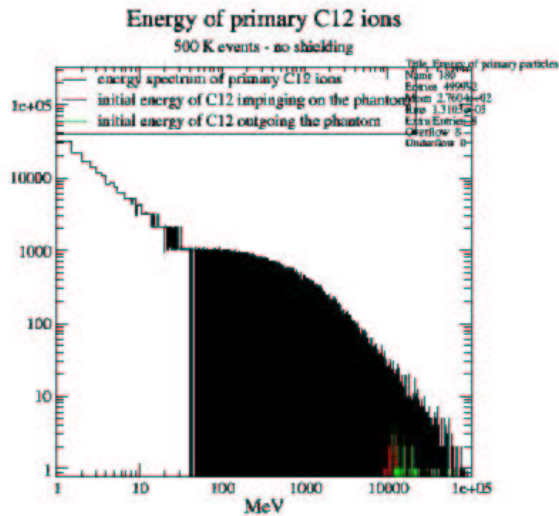


Figure 175: X =0.: initial energy of generated primaries is black, the initial energy for primaries reaching the Astronaut is red, the initial energy of primaries traversing the Astronaut is green.

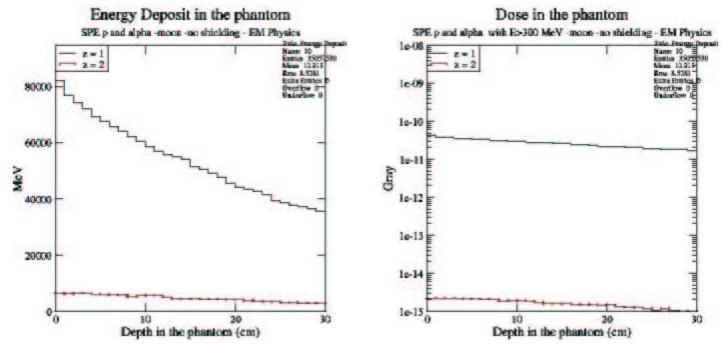


Figure 176: Energy deposit and dose given by SPE protons and alpha particles in the experimental set-up shown in fig 172; primary particles are generated with $E > 300.MeV$.

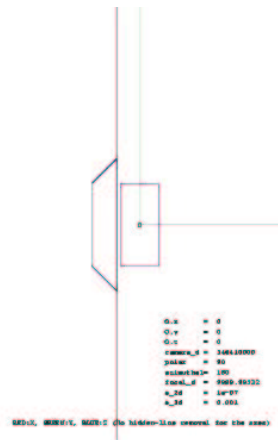


Figure 177: Experimental set-up: moon habitat with $X = 3.m$.

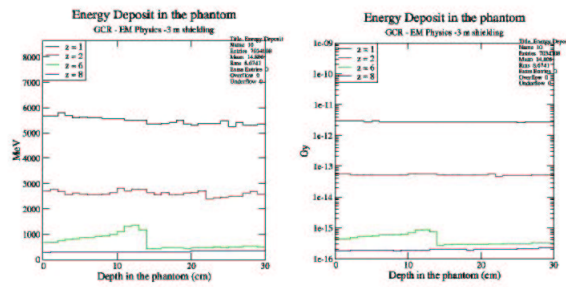


Figure 178: Energy deposit (first plot) and dose in the Astronaut given by GCR particles; the dose given by each GCR component is weighted in relation with the normalisation of the GCR energy spectra.

As shown in fig 179 and 180, the energy deposit in the Astronaut is less in the case of the moon habitat shown in fig. 177 ($X = 3.m$) than in the case of the habitat illustrated in fig. 172. The layer of soil moon (3. m thick layer) shields more particles.

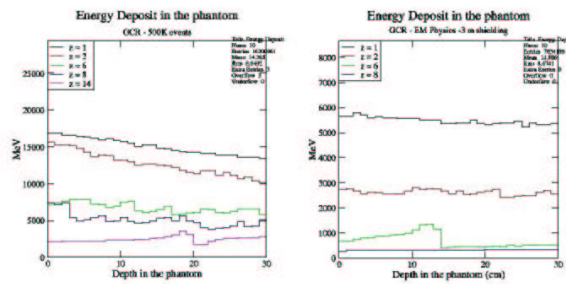


Figure 179: Comparison between the energy deposit in the Astronaut given by GCR particles in the case of $X = 0.m$ (first plot) and $X = 3.m$ (second plot).

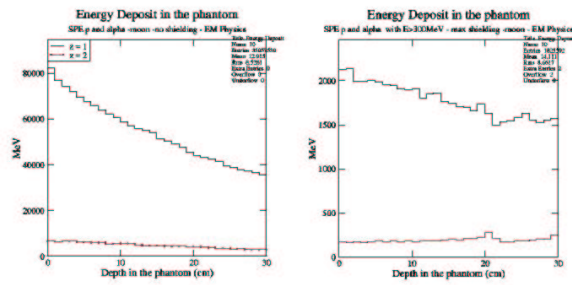


Figure 180: Comparison between the energy deposit in the Astronaut given by SPE particles in the case of $X = 0.m$ (first plot) and $X = 3.m$ (second plot).

11.5 Effect of the hadronic physics

The dosimetric effect of the hadronic processes has been evaluated on top of the results obtained with the activation of electromagnetic physics.

The experimental set-up adopted is shown in fig. 181. A particle beam impinges on the moon habitat with $X = 0.5 m$.

The primary particles can be GCR and SPE protons and alpha particles. The hadronic processes activated are listed in section 9. Fig. 182 and 183 show the effect of activation

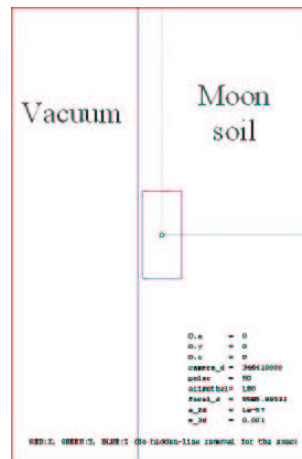


Figure 181: Experimental set-up adopted for the study of the effects of hadronic processes in moon habitat concepts ($X = 0.m$).

of the hadronic physics in comparison to the case with electromagnetic physics only, for

GCR and SPE protons and alpha particles.

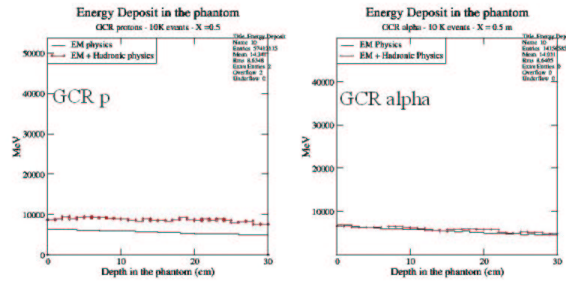


Figure 182: Energy deposit in the Astronaut resulting from GCR particles, activating Geant4 electromagnetic physics only and hadronic physics on top of it: GCR protons (left), GCR alpha (right).

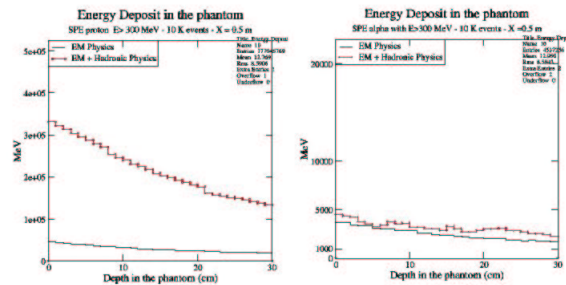


Figure 183: Energy deposit in the Astronaut resulting from SPE particles, activating Geant4 electromagnetic physics only and hadronic physics on top of it: SPE protons (left), SPE alpha (right).

11.6 Conclusions

From the plot enclosed in this section, we can observe a significant contribution to the dose in the Astronaut deriving from the activation of hadronic processes, presumably through the generation of secondary particles from hadronic interactions. However it is premature to reach quantitative conclusions about the dosimetric effects associated to hadronic processes: in fact, while the precision of Geant4 electromagnetic physics is well known and the effect deriving from electromagnetic interactions can be reliably estimated quantitatively, an intensive programme of validation of Geant4 hadronic physics and of

Table 10: CPU time needed for 10 K events simulation production .

	CPU time
C12 ions	$\sim 10.h$
Si28 ions	$\sim 7.5h$

further refinement of the hadronic models is still in progress.

Therefore this preliminary study is meant to provide an indication that hadronic processes may play a significant role in the optimisation of the moon habitat configurations, but it is recommended to perform the shielding optimisation studies of moon habitats at a stage when the degree of reliability of Geant4 hadronic models will be better known.

12 Exploitation of distributed computing resources

The dosimetric studies of moon habitats evidence the need of large event statistics for the production of meaningful results. Such high events statistics require a significant investment of CPU time. For this reason the Geant4 REMSIM application has been migrated to a distributed computing environment.

12.1 CPU resources for simulation production

Examples of CPU times required to simulate 10 K events with the experimental set-up illustrated in fig. 184 are shown in tab. 10.

If the random generation of primary particles over a hemisphere is introduced, as shown in fig. 170, a larger number of primary events to be generated is required to obtain statistically significant results for dosimetric studies because of geometrical acceptance reasons. As a rough estimate, the CPU time required for a statistically significant simulation production with the GCR and SPE particles is approximately 24 days on a 1.5 GHz Pentium 4 machine.

12.2 Strategy

The REMSIM simulation application has been parallelised to run in a distributed computing environment. In this way high statistics can be generated in a shorter time; however, this configuration require the availability of a computing farm.

The architectural solution chosen for access to distributed computing resources consists in the adoption of an intermediate layer between the application and the farm.

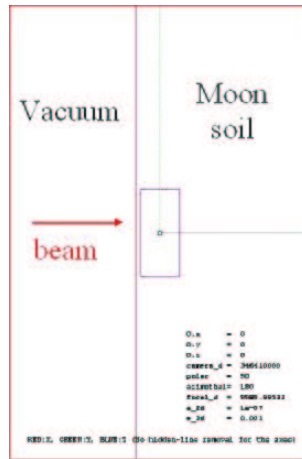


Figure 184: Experimental set-up: GCR particles hitting the moon habitat corresponding to the configuration with $X = 0.m$.

12.3 DIANE

DIANE [28] is a thin software layer which easily works on top of more fundamental middleware such as CPU local farms, or geographically distributed computing resources. Applications may be run in local clusters or on geographically distributed computing resources without any special modifications. The architecture of DIANE is shown in fig. 185.

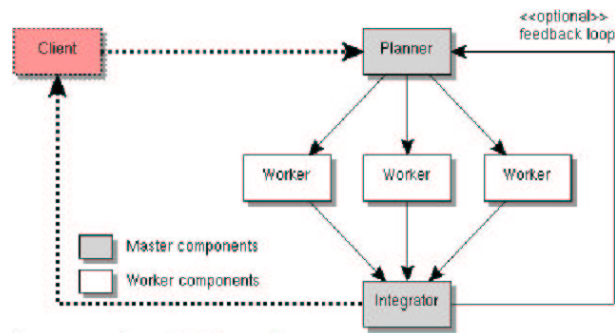


Figure 185: DIANE structure: the client sends the job to the planner; the planner splits the job into tasks, sent to workers; the workers execute the tasks, then the integrator sums the results of all the tasks. Finally the result of the job is sent back to the client.

12.4 Integration of the Geant4 REMSIM application with DIANE

The Geant4 REMSIM application has been integrated in the DIANE framework without affecting the code.

As an example of running the Geant4 REMSIM application in parallel mode, the plot in fig. 186 has been produced. The application ran on the CERN LSF farm.

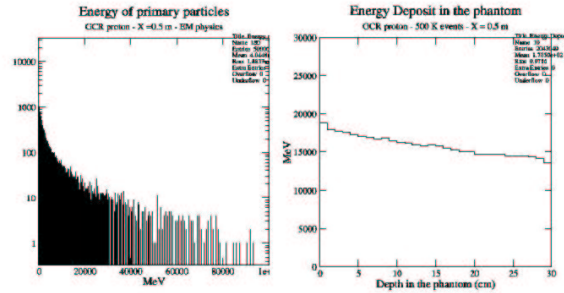


Figure 186: Results from REMSIM simulation executed in parallel mode.

12.5 Conclusions

The large event statistic requirements for REMSIM simulation production requires extensive computing resources. The usage of a computing farm for parallel production is recommended for future shielding studies. A solution for the parallelisation of Geant4 REMSIM application has been demonstrated and preliminary results confirming its feasibility are available.

13 Conclusions

Software system based on the Geant4 Toolkit has been designed and implemented for the study of radiation exposure in interplanetary manned missions.

Simple geometrical configurations, representing the essential features of vehicle concepts and moon habitats have been modeled. The dosimetric effects of Galactic Cosmic Rays and Solar Particle Events have been studied in these configurations, evaluating possible shielding options.

This study verified the availability of electromagnetic physics models in Geant4 adequate for precise evaluations of dosimetric effects, for all the types of particles involved (protons, alpha particles and ions). The results obtained have an accuracy of few percent as a contribution from Geant4 electromagnetic physics.

A preliminary evaluation of the dosimetric contribution due to hadronic processes has been performed for protons and alpha particles; such study has not been possible for ions, because Geant4 does not provide any models for them yet. Since Geant4 hadronic package is still under development and its validation studies are still in progress, the results presented in this report should be treated as preliminary indications rather than quantitative estimates; however these first studies suggest that the contributions from hadronic interactions should be taken into account and may be significant.

The study highlighted the requirement of significant CPU time for the production of statistically significant results, even in the very simple geometrical configurations considered. Therefore more in depth studies of the physics aspects or more sophisticated geometrical configurations are expected to require prohibitively large CPU resources for sequential production. The usage of a computing farm is recommended for future studies. For this purpose the simulation application developed for REMSIM has been parallelised, to operate transparently both on a single machine or in a distributed computing environment.

14 Acknowledgment

This work has been performed as part of contracts REM-SC-INFNGE-0418 and 572440524494 with ALENIA SPAZIO S.p.A., in the context of contract REMSIM with the European Space Agency.

References

- [1] S. Agostinelli et al., NIM A 506, 250-303 (2003).
- [2] I. Jacobson, J. Booch, J. Rumbaugh: The Unified Software Development Process (ed. Addison-Wesley, 1999).
- [3] P. Kruchten: The Rational Unified Process: an introduction (ed. Addison-Wesley, 2000).
- [4] G. Barrand et al., Abstract interfaces for data analysis: component architecture for data analysis tools, in: Proceedings of the CHEP 2001 Conference (Beijing, China, 2001)
- [5] ISO/IEC Joint Technical Committee 1 (JTC1): ISO/IEC DTR 15504 Software Process Assessment.
- [6] http://www.ge.infn.it/geant4/space/remsim/requirements/vision_remsim.html.

- [7] The Standish Group International: Extreme chaos (2001).
- [8] http://www.ge.infn.it/geant4/space/remsim/project_management/risk_list_remsim.html
- [9] http://www.ge.infn.it/geant4/space/remsim/design/SAD_remsim.html
- [10] http://www.ge.infn.it/geant4/space/remsim/project_management/iteration_plan_remsim.html
- [11] ALENIA SPAZIO: SG-PP-AI-1171, vol. 1 and 2.
- [12] E. Gamma, R. Helm, R. Johnson, J. Vlissides: Design patterns (Addison-Wesley, 1995).
- [13] O. Couet et al., ANAPHE OO Libraries and tools for data analysis, CERN-IT-2001-012 in: Proceedings of the CHEP 2001 Conference (Beijing, China, 2001).
- [14] S. Giani et al., Geant4 simulation of energy losses of ions, INFN/AE-99/21.
- [15] S. Giani et al., Geant4 simulation of energy losses of slow hadrons, INFN/AE-99/20.
- [16] J. Apostolakis et al., Geant4 low energy electromagnetic models for electrons and photons, INFN/AE-99/18.
- [17] F. Salvat et al., Penelope, a code system for Monte Carlo simulation of electron and photon transport, NEA/NSC/DOC(2001)19.
- [18] A. Allisy et al., ICRU Report 49, 1993.
- [19] J.F. Ziegler and J.M. Manoyan, NIM B 35 215 (1988).
- [20] S. Guatelli et al., Precision Validation of Geant4 Electromagnetic Physics in: Proceedings IEEE NSS (Portland, USA, 2003).
- [21] P. Nieminen, Report: Space Radiation Environment in the context of Interactions of Radiation with Biological Systems at the Cellular and DNA level.
- [22] P. Parodi, private communication, 23 February 2004.
- [23] <http://www.nist.gov>
- [24] R. Rampini, private communication, 30 February 2004.

- [25] P. Cirrone et al., A new MonteCarlo Simulation Tool for the development of a Proton Therapy Beam Line and Verification of the Related Dose Distributions, in: Proceedings IEEE NSS (Portland, USA, 2003).
- [26] D. Wright, private communication.
- [27] R. Rampini, private communication, 9 March 2004.
- [28] J.T. Moscicki, Distributed analysis environment for HEP and interdisciplinary applications, Nuclear Instruments and Methods 502 426-429 (2003).